Eidgenössische Technische Hochschule Zürich
Swiss Federal Institute of Technology Zurich

Master's Thesis

A critical appraisal of asymptotic 3D-to-2D data transformation and the potential of complex frequency 2.5-D modelling in seismic full waveform inversion

Ludwig Auer

IDEA League	Joint Master's in Applied Geophysics
Supervisors:	Prof. Dr. Stewart A. Greenhalgh Prof. Dr. Hansruedi Maurer Stefano Marelli
Co-examiner:	Prof. Dr. Kees Wapenaar
Start date:	1st of February 2011
End date:	8th of August 2011

Contents

Acknowledgements

Herewith I would like to express my acknowledgements to all the people who have contributed to making the period of my MSc thesis an enjoyable and instructive time.

I owe my sincere gratitude to my supervisor, Prof. Stewart Greenhalgh, for his always friendly and patient explanations on the issues I encountered, his tireless review of my text and the helpful comments on my work. Thank you also for your advice beyond the project itself! I am equally thankful to my other supervisor, Prof. Hansruedi Maurer, for his kind guidance in finding this project in the first place, defining the final project proposal and helping me to keep track of the main tasks. My special thank goes to my daily supervisor Stefano Marelli, for his willingness to explain me things again and again, his steady availability, the diligent correction of my manuscript and the many discussions. I couldn't have had a better tutor!

I also want to thank Edgar Manukyan for providing me with his 2.5-D examples, Giovanni Meles for helping me when Stefano was away, Anja Klotzsche for sending me her GPR pre-processing scripts and Kaspar Mertz for letting me join the amazing Furggwanghorn field campaign. I should not forget to mention the IDEA League Consortium and Shell who provided me with a scholarship, which greatly enhanced my financial situation.

Greets to all my Joint Master's classmates and especially the Zurich ones. It was nice to share an office with you. Finally, I want to thank my family for helping me out, whenever I run out of money and to Teresa, for the daily skype-meetings, encouraging me to study abroad and always being there.

Abstract

Seismic full waveform inversion is often based on forward modelling in the computationally attractive 2-D domain. Any solution of the 2-D cartesian wave equation inherently carries the assumption of being generated by a line source, extended in the out-of-plane direction, implying that source energy spreads over the surface of a cylinder, and that amplitudes scale with one over square-root of distance. However, realistic point sources like explosives or airguns, fired in a 3-D medium, generate amplitudes that decay with one over distance, since the wavefield expands spherically in all three dimensions.

Usually, practicioners correct for this amplitude difference and the associated phase shift of $\pi/4$ by transforming recorded field data to approximate 2-D, using simplistic asymptotic filter algorithms, operating on a time-sample basis and assuming straight ray paths and a constant velocity medium. The sometimes careless usage of these filters, is in contradiction to their well known limitations.

In this thesis, an extensive quantitative appraisal of 3D-to-2D data transformation procedures is presented. My analysis relies on a simple numerical modelling study, based on propagating 3-D and 2-D wavefields through 2-D media and comparing true 2-D and filtered 3-D synthetic data. It is demonstrated that filtering errors are moderate in purely acoustic situations but become substantial in complex media when arrivals overlap each other or ray paths deviate strongly from straight lines. Normalized root-mean-square deviations up to 5 % and maximum relative time domain errors up to 40 % were found in high contrast media, when full elastic treatment was considered.

In the second part of this thesis the potential of 2.5-D modelling as an alternative to 3D-to-2D transformation is investigated. Frequency-domain 2.5-D modeling is based on Fourier transforming the 3-D wave equation along the invariant axis to frequency-wavenumber domain and solving the resulting equation for many wavenumber components, thus breaking down the 3-D problem to a high number of 2-D problems.

An attempt is made to circumvent problems associated with singularities in the wavenumber spectrum by combining a finite-element 2.5-D forward solver and a complex-frequency extension. By shifting the poles off the real axis, they are avoided in the inverse Fourier transform to the frequency domain. It is shown that problems associated with the singularities are mitigated and the total number of required wavenumber samples is significantly reduced, as soon as frequencies are allowed to be complex. Reconstructed finite-element 2.5-D seismograms compare very well to reference finite-difference 3-D seismograms. 2.5-D modelling with complex frequencies outperforms asymptotic 3D-to-2D transformation showing very low misfits between 2.5-D and 3-D synthetics.

Abbreviations and Symbols

Acronym	Description
B1-3	Receivers B1, B2 and B3 in model BAT
BAT	Block model, acoustic, transmission-type
BC	Boundary condition
BET	Block model, elastic, transmission-type
CF	Complex frequency
(e)	Explosive source in FDM modelling
FD	Frequency domain
FDM	Finite difference method
FEM	Finite element method
GAR	Gradient model, acoustic, reflection-type
GF	Green's function
GP	Grid point
H1-3	Receiver H1, H2 and H3 in model HAT
HAT	Homogeneous model, acoustic, transmission-type
LAR	Layered model, acoustic, reflection-type
NRMSD	Normalized RMS deviation
PML	Perfectly matched layers
RMS	Root mean square
S1-3	Receivers S1, S2 and S3 in model SAT
SAT	Stochastic model, acoustic, transmission-type
SEM	Spectral element method
SET	Stochastic model, elastic, transmission-type
STD	Standard deviation
TD	Time domain
TEM	Time envelope misfit
(x)	x-directed source in FDM modelling

Symbol	Description	SI Unit
$A^{2D/3D}$	Amplitude at specified distance away from a source	Pa
$c,\ c_{min}$	Acoustic wavespeed, minimum wavespeed	ms^{-1}
C_m	Model covariance matrices	$-$
dt	Finite-difference time stepping interval	s
dh	FEM and FDM grid spacing	m
$\mathbf{d}^{pred}$	Predicted (synthetic) data	Pa or ms^{-1}
$\mathbf{d}^{obs}$	Observed (field) data	Pa or ms^{-1}
$E^{2D/3D}$	Energy at specified distance away from a source	J
$f,\ f_c$	Frequency, central (dominant) source frequency	s^{-1}
F, F^{-1}	Forward operator, Inverse operator	$-$
$G^{2D/3D/25D}$	Acoustic Green's functions in TD	m^{-1}
$\bar{G}^{2D/3D/2.5D}$	Acoustic Green's functions in FD	$-$
$\tilde{G}^{2D/3D/2.5D}$	Acoustic Green's functions in $\omega - k_y$ domain	$-$
$\hat{G}$	Exponentially damped Green's function solution	$-$
H, δ	Heaviside step function, Delta function	$-$
$H_0^{(1)}$	Hankel function of the 1st kind and zero order	$-$
$\mathbf{J}$	Sensitivity/Jacobian matrix	$-$
$J_0,\ Y_0$	Zero order Bessel function of the 1st and 2nd kind	$-$
K_0	Modified zero order Bessel function of the 2nd kind	$-$
$k_{x,z,y}$	Wavenumber in x,z and y direction	m^{-1}
k	Wavenumber = $2\pi\omega/\lambda$	m^{-1}
Δk_y	Wavenumber sampling density	m^{-1}
L	Wavelength	m
λ, μ	Lamé's first and second parameter	Pa
$\mathbf{m}^{est}$	Reconstructed model	ms^{-1}
n_{k_y}	Number of wavenumber samples	$-$
N_{dt}	Total number of time steps (FDM)	$-$
P	Acoustic pressure wavefield in time domain	Pa
$\bar{P}$	Pressure wavefield in frequency domain	Pa
$\tilde{P}$	Pressure wavefield in $\omega - k_y$ domain	Pa
$\hat{P}$	Exponentially damped pressure wavefield	Pa
Q	Quality factor	$-$
ρ	Medium density	kgm^{-3}
$\mathbf{r}, r$	Distance, $\mathbf{r} = (x, z, y), r = \lvert\mathbf{r} - \mathbf{r_0}\rvert$	m
$S, \bar{S}$	Source wavelet in the time and frequency domains	Pa
t	Time	s
$\mathbf{u}$	(Vectorial) Displacement vector	m
$V_P,\ V_S$	P-wave and S-wave velocity	ms^{-1}
$\omega, \omega_i, \omega_r$	Angular frequency, $Im[\omega]$, $Re[\omega]$	$rads^{-1}$

Chapter 1

Introduction

Full waveform inversion is a relatively young subdiscipline of seismic tomography which emerged in the 1980s, but was not fully exploited at that time, because of limited computational resources (Tarantola, 1986; Mora, 1987). Opposed to ray-based tomographic methods, not only first arrival times, but the entire waveform information is used in the inversion process. The optimization procedure is usually based on minimization of the misfit between observed and synthetic waveforms, propagated through realistic earth models, employing the full information content contained the data. Theoretically, waveform inversion is capable of reconstructing realistic earth models with sub-wavelength resolution (Fichtner, 2010).

Since the problem is highly non-linear, the model updating is usually performed in an iterative fashion using local-search optimization schemes. These algorithms have the tendency to get trapped in local minima, whenever the data quality, the source wavelet estimation, the closeness of the starting model to the true model, or the accuracy of the synthetic seismograms are poor. Thus, careful data preconditioning, such as a precise estimation of the source and reliable forward modelling are of utmost importance for the success of any waveform-inversion procedure (Virieux and Operto, 2009). Effectiveness of full waveform inversion is strongly problem dependent. There exists an ever growing variety of full wave inversion schemes, built around different types of forward solvers, which are operating either in the time or the frequency domain, and are exclusively designed for a particular field of application. Strategies, that pay off well in one field, might not work in other cases.

As a consequence, terminology is not consistent amongst different subdisciplines. What is called a "full" waveform in global seismology, where researchers often discard amplitude information, is very different from a "full" waveform in

exploration seismology, where all reflection events are included and surface waves are excluded in the inversion process (Fichtner, 2010). By contrast, in waveform inversion of data acquired for engineering and environmental investigations - cases which are not covered very often in the waveform inversion literature - surface waves and refracted waves are considered as a main carrier of useful information. For a comprehensive review of the history and state-of-the art of full waveform inversion, I refer to the article of Virieux and Operto (2009).

1.1 The 3D-to-2D problem

Any realistic seismic point source (explosive, sparker, airgun) fired in a 3-D medium creates a wavefront which spreads in all three directions. Full waveform inversion, however, is mostly performed in the computationally attractive 2-D domain (Brossier et al., 2009; Mulder et al., 2010). In terms of information content, this is acceptable, as long as the medium properties only change in two dimensions (e.g. the xz plane) and no out-of-plane arrivals are present in the data. Nevertheless 2-D is problematic, as any numerical or analytical solution of the 2-D wave equation inherently carries the assumption of being generated by a line source which is infinitely extended in the out-of-plane (strike) direction (Cervený, 2005).

In a homogeneous, constant-velocity medium, a point-source wavefront is spherical, whereas a line-source wavefront is cylindrical. This leads to amplitude and phase differences between the recorded 3-D and the modelled 2-D data. It is necessary to take care of this difference. Obviously, the natural solution would be to choose a forward modelling technique that is based on the full 3-D wave equation. However, solving the 3-D problem numerous times within full waveform inversion codes, is still a very computationally challenging exercise, even for acoustic media.

Only a very few examples of real 3-D full waveform inversions have been published (Ben-Hadj-Ali et al., 2008; Vigh and Starr, 2008). Generally, it is the forward problem which contributes the most to the total computational expenses. In time-domain modelling, the limiting factor is total run-time, as each source position requires a new forward computation. In frequency-domain modelling, multiple sources add little to the computational costs (see Sec. 2.1) but when full 3-D treatment is being considered, the system matrices can become extremely large and often exceed the available memory resources. Even though the 3-D problem might be tractable on institutional scale systems in around 5-10 years, the demand

for full-wave inversion procedures that are executable on single machines or even mobile hardware justifies the effort to quest for cheaper alternatives.

1.1.1 Solutions to the 3D-to-2D problem

There exist various approaches to generate synthetic seismograms which are quantitatively comparable to recorded field data, without having to deal with true 3-D modelling. Techniques to solve the 3D-to-2D problem can roughly be classified into three major categories (Roberts, 2005):

1. Reformulating the problem in (quasi-)cylindrical coordinates (Igel et al., 1993; Takenaka and Tanaka, 2003) and synthesizing line source data by integrating over many point-sources along the experimental axis in CMP sorted data (Wapenaar et al., 1992).
2. Asymptotic 2.5-D filtering procedures (Deregowski and Brown, 1983; Vidale et al., 1985; Bleistein, 1986; Esmersoy and Oristaglio, 1988; Williamson and Pratt, 1995; Miksat et al., 2008; Deregowski and Brown, 1983; Yedlin et al., 2011) to convert the 3-D (point source) data to 2-D (line source) data.
3. True 2.5-D modelling by Fourier transforming the governing partial differential equation along the y-axis to $\omega - k_y$ or $x - k_y$ domain and solving the resulting 2-D problem for many k_y-components (Song and Williamson, 1995; Zhou and Greenhalgh, 1998b; Novais and Santos, 2005; Sinclair, 2009), which can be done in either the time domain or the frequency domain, and yields approximate 3-D wavefields.

In this thesis, only the latter two approaches will be investigated. 2.5-D techniques directly exploit symmetries of the so called 2.5-D configuration. A typical 2.5-D problem consists of a 3-D point source which is situated inside a 3-D medium that is invariant in the y direction, i.e. a point source in a 2-D model (Cao and Greenhalgh, 1997).

It is a common practice in 2-D seismic experimental design to acknowledge the benefits of 2.5-D symmetry by placing sources and receivers in a plane perpendicular to the strike axis. This obviates any out-of-plane arrivals and leads to problems which are essentially two dimensional (Williamson and Pratt, 1995).

Strictly speaking, any 2.5-D method is only applicable in the absence of out-of-plane events, which will be true if the geology is unchanging in the transverse direction. Note, that one can still do 2.5-D modelling when receivers are located outside the central $(y = 0)$ plane.

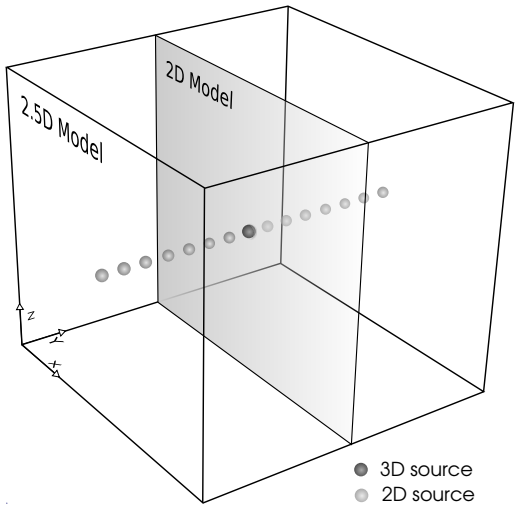

Figure 1.1: *A typical 2.5-D configuration with a purely two-dimensional geometry that is invariant in the y direction. A 2-D source modelled within a 2-D experimental domain inherently carries a line source assumption (Sec. 2.2).*

1.1.1.1 Asymptotic 3D-to-2D data transformation

Amongst the presented techniques, 3D-to-2D data transformation using an asymptotic filter, is by far the most widespread approach within the waveform-inversion community. It has the advantage of simple implementation and neglible computational costs.

In almost all field data applications of full-waveform inversion that have been reported in the literature, researchers rely on very simple straight-ray approximations of these transformations (Crase et al., 1990; Pica et al., 1990; Reiter and Rodi, 1996; Hicks and Pratt, 2001; Shipp, 2001; Belina et al., 2008; Bleibinhaus et al., 2009; Mulder et al., 2010). Some practitioners even completely neglect phase correction and apply only amplitude corrections by multiplying the recorded field data with a square-root-of-time dependent gain function.

The often careless usage of filtering methods is in stark contradiction to their well known drawbacks. Filtering errors, which are due to both fundamental limitations of asymptotic theory and over-simplifyed filter implementation, are significant for highly heterogeneous media (Williamson and Pratt, 1995; Miksat et al., 2008).

1.1.1.2 True 2.5-D Modelling

True 2.5-D modelling can require the solution of a high number of 2-D simulations but it is still much cheaper than full 3-D modelling. Probably it is the only generally valid approach to compute approximate 3-D responses in 2-D media (Williamson and Pratt, 1995).

However, 2.5-D modelling performed in the frequency domain suffers from the problem of singularities at certain critical k_y values in the wavenumber spectra (Zhou and Greenhalgh, 2006). When wavenumber sampling is too coarse and some wavenumber samples coincidentally fall close to or exactly on one of the poles, the reconstructed frequency-space solution gets completely distorted (Zhou and Greenhalgh, 2006; Latzel, 2010; Sinclair, 2009).

For the acoustic case, the aforementioned problems can be circumvented by avoiding the critical wavenumbers and increasing the sampling density at higher wavenumbers using a Gauss Legendre type sampling strategy (Zhou and Greenhalgh, 2006; Sinclair et al., 2011). For strongly heterogeneous media this approach is not suitable (Latzel, 2010) because the locations of the singularities are not known beforehand.

As an alternative, several authors (Cao and Greenhalgh, 1997; Greenhalgh et al., 2009; Latzel, 2010) propose to use complex frequencies, complex wavenumbers or complex medium parameters, to move the integration path away from the singularities, or the singularities away from the integration path, respectively.

1.1.2 Objectives and structure of this thesis

The main aim of this thesis is to critically investigate the limitations of 3D-to-2D conversion filters as a pre-processing step to 2-D inversion. This is done in both the time domain and the frequency domain. The other principal objective is to devise a suitable wavenumber sampling strategy combined with a complex frequency approach to 2.5-D modelling, which obviates the need to apply asymptotic correction filters.

In Chapter 2 I provide an introduction to some basic theoretical concepts, explain the differences between three- and two-dimensional wave propagation and tabulate the analytical solutions which are used for various purposes throughout this thesis.

In Chapter 3 I present a critical assessment of the validity of the asymptotic

3D-to-2D transformation. Filter performance is evaluated by means of a simple numerical modelling study, based on propagating 3-D and 2-D wavefields in 2-D models, and subsequently comparing line source and filtered point source data in the time and frequency domains. Subsequently, I perform a full waveform inversion on true 2-D and filtered 3-D data in order to examine to what extent the conversion errors degrade the reconstructed models.

In Chapter 4 I investigate if 2.5-D modelling is a viable alternative to asymptotic 3D-to-2D transformation. It is shown that problems associated with critical wavenumbers in frequency-domain 2.5-D modelling can be mitigated by combining an acoustic 2.5-D FEM solver with a complex-frequency extension.

Appropriate combinations of the imaginary part and the wavenumber sampling density were identified in simple experiments based on analytic 3-D and 2.5-D fullspace solutions. Finally, it is investigated how FEM 2.5-D modelling, performed over a typical range of complex valued frequencies, compares to FDM 3-D modelling, in both the time and the frequency domain.

Chapter 2

Theoretical framework

2.1 Solution of the forward problem

Solving an inverse problem most often relies on having a suitable algorithm to solve the forward problem, that is - in the context of waveform inversion - generating high-quality synthetic data $\mathbf{d}^{pred}$ (i.e. the theoretical or predicted seismic response) for a specified earth model $\mathbf{m}$

$$\mathbf{d}^{pred} = F(\mathbf{m}) \tag{2.1}$$

There exists a wide choice of forward solvers F to accomplish this task. Broadly speaking, the available methods can be classified in ray-based and wave-equation based approaches (Sinclair, 2009). Ray-methods are actually the high frequency solution and often fail to incorporate diffraction effects and guided waves. The latter are generally much more computationally intensive and provide more exact seismograms.

The three most popular wave-equation based methods are probably the finite-difference method (FDM), the finite-element method (FEM) and the spectral-element method (SEM). For an extensive review of forward solvers that can be employed in waveform inversion, the reader is referred to Virieux and Operto (2009).

Any of the aforementioned modelling techniques is based on a governing equation of a specified degree of complexity (e.g. acoustic, elastic, visco-elastic, anisotropic) and can be implemented in the time domain or in the frequency domain. Both the discretization in the frequency domain and in the time domain

have intrinsic advantages and disadvantages. See Sections 2.1.1 and 2.1.2 for a consideration of the individual strengths of acoustic, elastic, frequency-domain and time-domain seismic modelling.

In Chapter 3 3-D and 2-D seismic wavefield modelling is performed with a well established visco-elastic finite-difference code, developed by Bohlen (2002). Spatial discretization is based on a staggered-grid approach, meaning that field variables are distributed amongst grid-points (which - as opposed to regular grid approaches - allows a coarser grid and significantly reduces computational costs).

In Chapter 4 an acoustic 2.5-D rectangular grid finite-element code which was developed in-house (Latzel, 2010; Min et al., 2003) and employs perfectly matched layer (PML) boundary conditions and the PARDISO direct matrix solver to invert the system matrix (Schenk and Gärtner, 2004). Further details on the used FDM and FEM solvers are provided in Sections 3.2.1 and 4.4.

2.1.1 Equations of motions in the time domain

Elastic equation of motion

A form of the elastic equation of motion, which is often the basis of elastic wave-equation modelling, is for example given by (Slawinski, 2003)

$$\rho(\mathbf{r})\frac{\partial^2\mathbf{u}(\mathbf{r},t)}{\partial t^2} = (\lambda(\mathbf{r})+2\mu(\mathbf{r}))\nabla(\nabla\cdot\mathbf{u}(\mathbf{r},t)) - \mu(\mathbf{r})\times\nabla\times(\nabla\times\mathbf{u}(\mathbf{r},t)) \quad (2.2)$$

where $\mu(\mathbf{r})$ and $\lambda(\mathbf{r})$ are the Lame constants, $\mathbf{u}(\mathbf{r},t)$ is the displacement field and $\rho(\mathbf{r})$ is the mass density. Body and gravitational forces have been neglected.

Eq. 2.2 describes non-dissipative seismic wave propagation through general inhomogeneous isotropic media and can be derived from the equation of momentum, a constitutive stress-strain relation and the definition of strain.

Acoustic equation of motion

When the medium under investigation behaves like a fluid, the shear modulus μ effectively reduces to zero. In this case wave propagation can be modeled with the lossless constant-density acoustic wave equation (Cao and Greenhalgh, 1997)

$$\nabla_3^2 P(\mathbf{r},t) = \frac{1}{c^2(\mathbf{r})}\frac{\partial^2 P(\mathbf{r},t)}{\partial t^2} - S(t)\delta(\mathbf{r}-\mathbf{r_0}) \tag{2.3}$$

where ∇_3^2 is the 3-D Laplacian operator, $P(\mathbf{r},t)$ is the dynamic pressure, $c(\mathbf{r})$ is the spatial distribution of acoustic wavespeed and $S(t)$ is the source-time function. In the acoustic constant-density approximation, the problem reduces to just one effective medium parameter (i.e. acoustic wavespeed).

Elastic or acoustic full waveform inversion

Most experiments performed within this thesis are based on acoustic wave modelling as it offers the advantage of smaller computational requirements and simpler mathematical description. The assumptions of acoustic wave propagation can be met when the influence of the shear component is kept small by using pressure receivers (hydrophones) and omnidirectional pressure sources (explosives).

Nevertheless, the acoustic approximation may be problematic when the medium comprises large, high-contrast interfaces. These can cause mode conversions, leading to a highly complicated wavefield, when interference occurs between the different wave modes. For an extensive review of the validity of the acoustic approximation in full-waveform inversion see Marelli et al. (2011).

2.1.2 Acoustic frequency-domain Helmholtz equations

As mentioned above, full waveform inversion is often carried out with frequency-domain algorithms, which offer some computational and practical advantages over time-domain schemes. To obtain frequency-domain representation of the hyperbolic Eq. (2.3), a temporal Fourier transform is performed to converts it to the elliptic 3-D frequency domain Helmholtz equation, which can be written as (Cao and Greenhalgh, 1997)

$$\nabla_2^2 \bar{P}(\mathbf{r},\omega) + \left[\frac{\omega^2}{c^2(\mathbf{r})}\right]\bar{P}(\mathbf{r},\omega) = -\bar{S}(\omega)\delta(\mathbf{r}-\mathbf{r_0}) \tag{2.4}$$

where ω is the angular frequency, $\nabla_2^2 = \partial_{xx} + \partial_{zz}$ is the 2-D Laplacian, and $\bar{S}(\omega)$ is the frequency-domain representation of the source time function. Performing an additional spatial Fourier transform along the y axis, one obtains the 2.5-D acoustic Helmholtz equation (Zhou and Greenhalgh, 1998a)

$$\nabla_2^2 \tilde{P}(\mathbf{r}, k_y, \omega) + \left[\frac{\omega^2}{c^2(\mathbf{r})} - k_y^2 \right] \tilde{P}(\mathbf{r}, k_y, \omega) = -\bar{S}(\omega)\delta(\mathbf{r} - \mathbf{r_0}) \tag{2.5}$$

where k_y is the wavenumber in the y direction and $k_{xx}^2 = \frac{\omega^2}{c^2(\mathbf{r})} - k_y^2 = k_x^2 + k_z^2$.

Frequency-domain or time-domain full waveform inversion

Frequency domain is attractive, as it allows to start with delineating the macrostructure, using low frequencies, and to progressively reconstruct more subtle features, using higher frequencies, which strongly mitigates the non-linearity problem (Virieux and Operto, 2009). Only a few deliberately well chosen frequencies are required to recover high-quality subsurface models (Maurer et al., 2009).

Another major advantage of frequency-domain full waveform inversion is that Eqns. (2.4) and (2.5) can be readily transformed in linear systems which are easy to solve with direct matrix solvers. Once the matrix is inverted it can be re-used to solve the forward problem for extra sources in very short time, by multiplying the inverted system matrix with each new source vector (Pratt and Shipp, 1998). However, working in the frequency domain exacerbates interpretation, as one cannot identify discrete arrivals or waveforms.

2.1.3 Green's function solutions

Whilst for general, inhomogeneous acoustic and elastic media Eqns. (2.4) and (2.5) have to be solved numerically, analytical solutions exist for some simple cases. In the following I tabulate some well known 3-D, 2-D and 2.5-D Green's function solutions for acoustic media. I will use them throughout this thesis for rapid wavefield modelling and validation of numerical algorithms.

3-D Green's function solutions

The solution for an omnidirectional 3-D point source in a unbounded, acoustic, homogeneous medium (i.e. fullspace) can be derived for example by using contour integration in the complex plane (Cervený, 2005, p. 77). In the frequency domain it is given by

$$\bar{G}^{3D}(\mathbf{r},\omega) = \frac{1}{4\pi r} exp\,(i\omega r/c) \tag{2.6}$$

The corresponding time domain expression is given by

$$G^{3D}(\mathbf{r},t) = \frac{1}{4\pi r}\delta(t - t_0 - r/c) \tag{2.7}$$

where r = $|\mathbf{r} - \mathbf{r_0}|$. See (Cervený, 2005, p. 79) for a derivation.

2-D Green's function solutions

The frequency-domain 2-D Green's function solution for an unbounded, acoustic, constant density fullspace is given by Abramowitz and Stegun (1965) or Cervený (2005, p. 97)

$$\bar{G}^{2D}(\mathbf{r},\omega) = \frac{i}{4} H_0^{(1)}(wr/c) \tag{2.8}$$

where $H_0^{(1)}$ is the Hankel function of the first kind and zero order. A Hankel function represents combinations of Bessel functions of the first and second kind. As will be shown in Section 2.2, the 2-D solution corresponds to a line source parallel to the y axis. Using the well known large-argument approximation of the Hankel function, one can obtain the asymptotic 2-D acoustic Green's function in the frequency domain (Morse and Feshbach, 1953; Cervený, 2005, p. 79)

$$\bar{G}^{2D}(\mathbf{r},\omega) \approx \frac{1}{2}\sqrt{\frac{c}{2\pi\omega r}} exp\left(\frac{i\omega r}{c}\right) exp\left(\frac{i\pi}{4}\right) \tag{2.9}$$

The argument in 2.8 ($w/r = kr = r/L$) is large in the far-field where distance r is high or wavelength L is low (i.e. at high frequency). Thus, approximation (2.9) breaks down in the near field or for low frequencies. Fourier transforming Eq. (2.8) one can obtain the time-domain acoustic 2-D Green's function (Morse and Feshbach (1953, p. 842); Bleistein (1984, p. 156))

$$G^{2D}(\mathbf{r},t) = \frac{1}{2\pi} H(t - t_0 - r/c)((t - t_0)^2 - r^2/c^2)^{-1/2} \tag{2.10}$$

where H is the Heaviside step function. The physical meaning of Eqns. (2.6 - 2.10) is given in Section 2.2 along with a description of how the involved terms describe the differences between point source and line source wave propagation.

2.5-D Green's function solutions

Performing a Fourier cosine transform on Eq. (2.6) along the y direction, and using a Table of Integrals, one obtains the doubly Fourier transformed Green's function (i.e. the 2.5-D acoustic frequency-wavenumber domain Green's function) for a homogeneous acoustic constant density fullspace in the following form

$$\tilde{G}^{2.5D}(k_y, \mathbf{r}, \omega) = \begin{cases} -\frac{1}{4}\left[J_0\left(r\sqrt{\frac{\omega^2}{c^2} - k_y^2}\right) - iY_0\left(r\sqrt{\frac{\omega^2}{c^2} - k_y^2}\right)\right] & , \quad k_y < \frac{\omega}{c} \\ \frac{1}{2\pi}K_0\left(r\sqrt{k_y^2 - \frac{\omega^2}{c^2}}\right) & , \quad k_y > \frac{\omega}{c} \end{cases} \tag{2.11}$$

Here $r = \sqrt{(x - x_0)^2 + (z - z_0)^2}$ is the source-receiver separation within the 2-D plane, $J_0(x)$ and $Y_0(x)$ are zero order Bessel functions of the first and second kind (Zhou and Greenhalgh, 2006; Aki and Richards, 2002) and K_0 is the modified zero order Bessel function of the second kind. Eq. (2.11) is the wavenumber-domain Green's function solution of Eq. (2.5). Note that the solution becomes singular when the terms under the square-root in Eq. (2.11) go to zero at $k_y = \frac{w}{c}$. For details on the nature of this singularity see Chapter 4.

2.2 Differences between 3-D and 2-D wave propagation

As shown in Section 2.1.3, the 3-D Green's function has a fundamentally different form than the 2-D Green's function. This difference is not only present in analytical solutions but can also be observed when Eqns. (2.8) and (2.6) are approximated on finite-difference or finite-element grids.

Following Miksat et al. (2008), I will demonstrate that the 2-D solution of the wave equation inherently carries the assumption of a line source, which is formed as the sum of 3-D point sources, continuously spread along the y axis. I consider a 2-D source (black dot in Fig. 2.1) situated at the origin of a 2-D plane. Green's functions are evaluated at receiver REC. The Green's function of the 2-D source

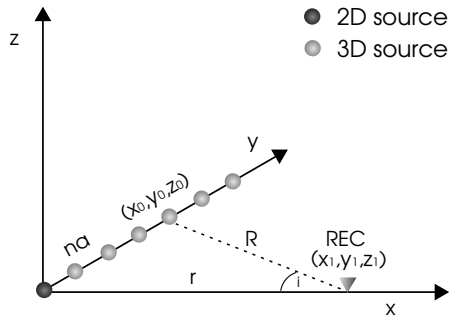

Figure 2.1: *Principle of the 2-D line source and the 3-D point source. It can be demonstrated that a 2-D source is equivalent to a continuum of 3-D point sources along the y axis. The 2-D line source is centered at the origin. The triangle represents a receiver REC in distance r from the origin. Modified after Miksat et al. (2008).*

can be assembled by summing over an infinite number of 3-D sources distributed along the y axis

$$G^{2D}(\omega, \mathbf{r}) \doteq \frac{2}{4\pi} \sum_{n=1}^{+\infty} \frac{exp(ikR)}{R} \tag{2.12}$$

with $R = \sqrt{(x_0 - x_1)^2 + (y_0 - y_1)^2 + (z_0 - z_1)^2} := \sqrt{x'^2 + y'^2 + z'^2}$ where $y' = na$. Expressing R as a power series and truncating it after the second term yields (Lauterborn et al., 1999, p. 151)

$$R = x' \sqrt{1 + \frac{y'^2}{x'^2} + \frac{z'^2}{x'^2}} \approx x' + \frac{y'^2}{2x'} + \frac{z'^2}{2x'} \tag{2.13}$$

When we assume that the ray along R makes a small angle i with the "optical" axis x we can apply the Fresnel approximation and rewrite the exponential term in (2.12) as (Lauterborn et al., 1999, p. 151)

$$\frac{exp(ikR)}{R} \approx \frac{exp(ikx')}{x'} exp\left(\frac{ik}{2x'}[y'^2 + z'^2]\right) \tag{2.14}$$

Since $z' = 0$ we can remove the z'-term in (2.14). Transforming the sum in Eq. (2.12) to an integral and evaluating it yields

$$G^{2D}(\omega, \mathbf{r}) = \frac{exp(ikx')}{4\pi x'} \int_{-\infty}^{+\infty} exp\left(\frac{iky'^2}{2x'}\right) dy' \tag{2.15}$$

$$= \frac{exp(ikx')}{4\pi x'} exp\left(\frac{i\pi}{4}\right) \sqrt{\frac{2\pi c x'}{\omega}} \tag{2.16}$$

where k has been replaced by ω/c. Substituting x' with r and taking $2\pi r$ outside of the square-root one obtains the high frequency approximation of the 2-D acoustic Green's function already shown in Eq. (2.9). The line source properties that are implicit in the 2-D cartesian solution of the wave equation have significant effects on geometrical spreading behaviour (Section 2.2.1) and wavelet characteristics (Sec. 2.2.2), which differ from those of the point source solution.

2.2.1 Amplitude decay behaviour

The most obvious difference between 3-D and 2-D wave propagation is their different amplitude decay behaviour with distance or time. As mentioned above, in case of a 3-D point source, energy spreads over the surface of a sphere, when the medium is homogeneous. Ignoring dissipation and assuming constant flux, the product of energy density (intensity) and surface area of the wavefront must be conserved. Thus the energy at a distance r from the source is given by

$$E^{3D} = \frac{E_T^{3D}}{4\pi r^2} \tag{2.17}$$

where E_T^{3D} is the total energy delivered by the source and $4\pi r^2$ is the surface area of a sphere. In the acoustic approximation, amplitude A is equal to $\sqrt{E}$. Considering the ratio between the amplitude A at a distance r and a reference amplitude A_0 at a distance r_0, one can see that point-source amplitudes are proportional to $1/r$

$$\frac{A^{3D}}{A_0^{3D}} = \sqrt{\frac{E^{3D}}{E_0^{3D}}} = \sqrt{\frac{r_0^2}{r^2}} = \frac{r_0}{r} \rightarrow A^{point} \propto \frac{1}{r} \tag{2.18}$$

In the 2-D (line-source) case energy spreads over the surface of an expanding cylinder, when the medium is homogeneous. Thus

$$E^{2D} = \frac{E_T^{2D}}{2\pi r B} \tag{2.19}$$

where B is the length of the cylinder. Again, one can establish the the ratio of amplitudes at two distances away from the cylinder axis, to obtain

$$\frac{A^{2D}}{A_0^{2D}} = \sqrt{\frac{E^{2D}}{E_0^{2D}}} = \sqrt{\frac{r_0}{r}} \rightarrow A^{2D} \propto \frac{1}{\sqrt{r}} \tag{2.20}$$

Figure 2.2 illustrates the different amplitude decay behaviour of $1/r$ and $1/\sqrt{r}$, by plotting amplitude decay on a decibel scale over distance. Line source and point source amplitudes have been set to the same reference value, 5 m away from the source. At a distance of 50 m away from the source, amplitudes of the 3-D solution have already decayed by around 10 dB, while 2-D amplitudes have only decayed by around 5 dB.

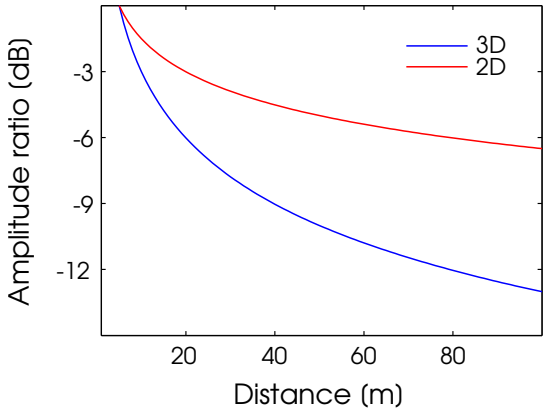

Figure 2.2: *Difference in amplitude decay ratio (dB) with increasing distance from the source. Amplitudes of the 3-D and the 2-D solution have been set to the same reference value 5 m away from the source. Modified after Liner (2004).*

Figure 2.3 shows a color-coded plot of 2-D and 3-D acoustic frequency-domain Green's functions (2.8 and 2.8) on a 100×100 m homogeneous domain with a constant velocity of 1500 m/s and a source located on the left edge. Again, 2-D and 3-D amplitudes have been set to the same value 5 m away from the source, for better visibility. The more rapid geometrical decay of the 3-D wavefield is clearly visible.

Geometrical spreading of the wavefront is responsible for only part of the total amplitude decay. In realistic, strongly absorbing media, energy loss due to frequency-dependent visco-elastic dissipation (internal friction) can dominate.

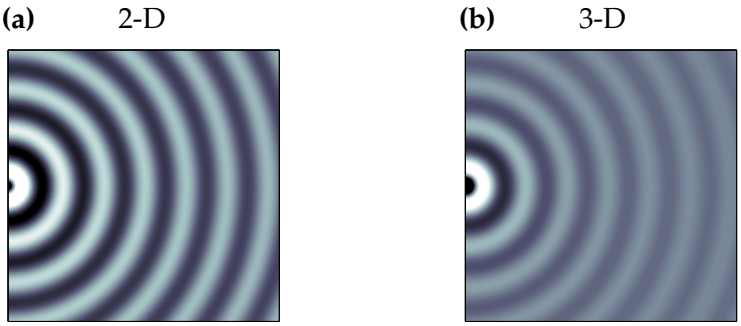

Figure 2.3: *Amplitude color-coded plots of 2-D and 3-D frequency-space domain Green's function solutions for a fixed frequency of 100 Hz. In the 2-D case, energy is spread over a circle and decays with* $1/\sqrt{t}$ *whereas in 3-D the energy spreads over a sphere and scales as* $1/t$.

2.2.2 Wavelet shape and spectral properties

The line-source nature of 2-D wave propagation has a signficant influence on wavelet shape and spectral properties of the wavefield. Compared to the time-domain 3-D Green's function (2.6), which includes a delta function that immediately goes to zero after it has passed a receiver, the 2-D Green's function sees later energy arriving from increasingly distant point sources along the y axis. This results in the so called "long-tail" or "$\sqrt{t}$-tail" which can mathematically be understood from the square-root term in (2.10) and causes an asymmetric shape of the 2-D wavelet (Fig. 2.4).

The 3-D frequency-domain Green's function shows regularly oscillating behaviour (Fig. 2.5). By contrast, the 2-D frequency domain Green's function (2.9) is scaled as $(\omega)^{-1/2}$ which explains the smaller amplitudes at larger angular frequencies. The $\pi/4$ phase shift between 2-D and 3-D solution can be understood from the multiplication with $exp(i\pi/4)$ in the asymptotic 2-D Green's function (2.9). The dominance of lower frequencies in the 2-D Green's function can physically be explained with an increasingly destructive interference pattern of point sources along the y axis for higher frequencies.

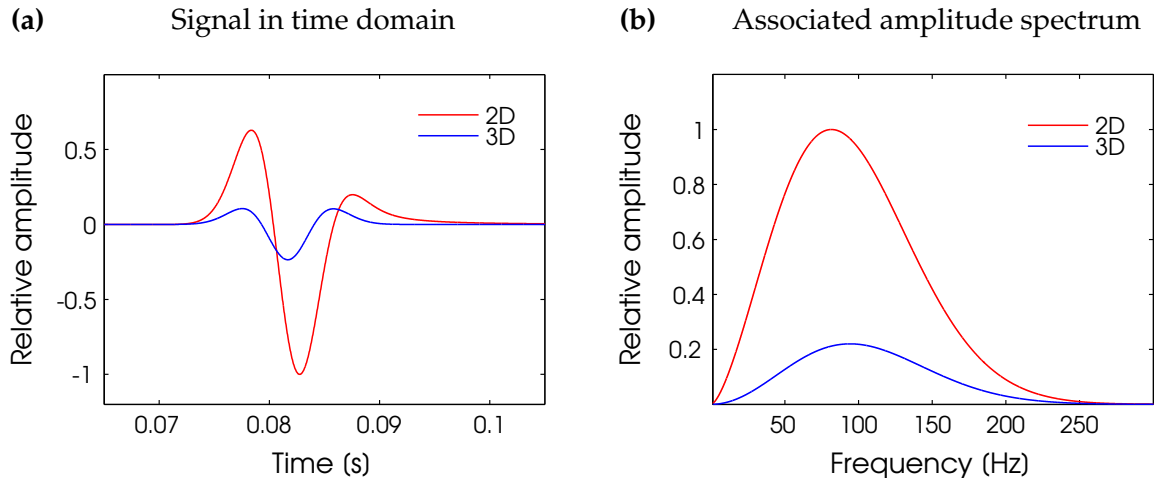

Figure 2.4: ***(a)*** *2-D and 3-D time-domain responses, generated by computing 2-D and 3-D frequency domain Green's functions for many frequencies and multiplying them with the spectrum of a Ricker wavelet having a central frequency of* 50 *Hz. A seismogram is then obtained by inverse Fourier transformation. Results are given for a single receiver* 100 *m away from the source.* ***(b)*** *Associated 2-D and 3-D amplitude spectra. The 3-D envelope is slightly shifted towards higher frequencies, while in the 3-D spectrum lower frequencies dominate.*

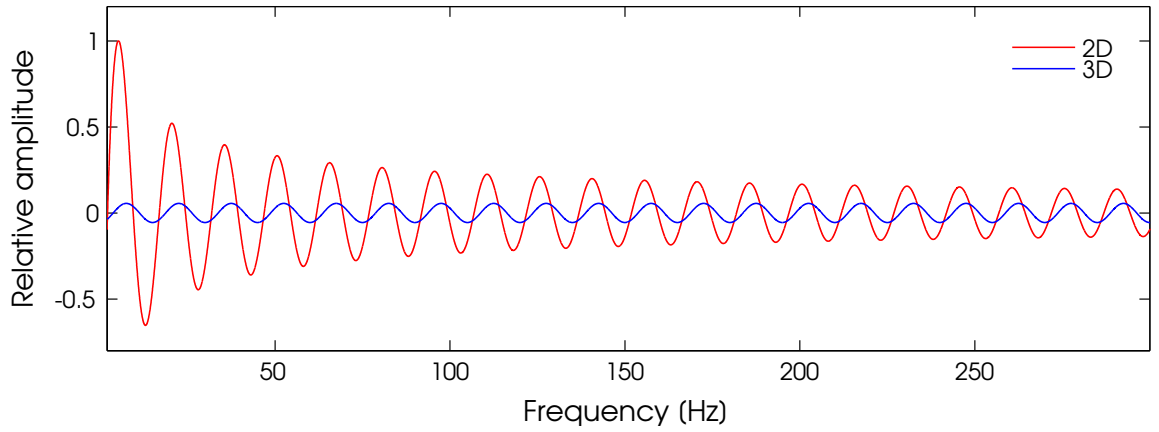

Figure 2.5: *Frequency-domain acoustic Green's function at one receiver for a fixed source receiver separation of* 100 *m, plotted as a function of frequency. While the 3-D Green's function shows constant amplitudes over the frequency band, the 2-D solution does not. Mathematically, this can be understood from the Hankel function which is involved in the 2-D Green's function. A physical interpretation is an increasingly destructive interference pattern of 3-D sources distributed along the y axis. Note that the 2-D solution is phase-shifted by* $\pi/4$ *at high frequency.*

2.3 Solution of the inverse problem

The inverse problem in full waveform inversion corresponds to a reconstruction of the medium parameters $\mathbf{m}^{est}$ from the observed data $\mathbf{d}^{obs}$ employing an inverse operator F^{-1}, and is given by

$$\mathbf{m}^{est} = F^{-1}(\mathbf{d}^{obs} - \mathbf{d}^{pred}) \tag{2.21}$$

The optimization algorithm used for the full waveform inversion presented in Section 3.3 is based on a regularized Gauss-Newton type approximation of the inverse operator F^{-1}, employing an L2-norm misfit function (Maurer et al., 2009). It can be written as

$$\mathbf{m}^{est}_{i+1} = (\mathbf{J}^T\mathbf{J} + \lambda\mathbf{C}^{-1}_M)^{-1}J^T[(\mathbf{d}^{obs} - \mathbf{d}^{pred}) + \mathbf{J}\mathbf{m}^{est}_i] \tag{2.22}$$

where $\mathbf{J}$ is the Jacobian or Sensitivity matrix, $\mathbf{m}^{est}_0$ is the initial model, i is the iteration number and $\mathbf{C}^{-1}_M$ is the model covariance matrix incorporating damping and smoothing factors. Unlike many other algorithms, the used optimization scheme employs explicit expressions (Zhou and Greenhalgh, 1999) to compute the sensitivities in $\mathbf{J}$.

Chapter 3

3D-to-2D transformation using asymptotic filters

In this Chapter I present an overview of popular asymptotic 3D-to-2D filtering techniques along with a critical appraisal of their accuracy. I performed various reflection and transmission type experiments based on computing time-domain 3-D and 2-D solutions and comparing the true 2-D result to the filtered 3-D data.

All numerical experiments in this Chapter were initially performed with a dominant source frequency of 100 Hz. For a direct comparison with the finite-element 2.5-D results presented Chapter 4, where I reduced the dominant frequency in order to save computation time, several of the finite-difference experiments were repeated using 50 Hz source central frequency.

I mainly focus on how good or poor the approximate staight-ray time domain filter (Section 3.1.2) operates, since this is the technique which is most popular and has the widest range of applicability. Windowed frequency-domain filtering in combination with raytracing (Section 3.1.2) is only of limited relevance in waveform inversion and thus only applied on a very simple 1-D reflection-type model, as a proof of concept.

3.1 Introduction to 3D-to-2D filtering

3.1.1 Filter derivation

Asymptotic point-source to line-source conversion filters have been presented by various authors in different contexts (Deregowski and Brown, 1983; Vidale et al., 1985; Bleistein, 1986; Esmersoy and Oristaglio, 1988; Williamson and Pratt, 1995; Miksat et al., 2008; Deregowski and Brown, 1983; Yedlin et al., 2011). The most cited approach is probably that of Bleistein, who used Asymptotic Ray Theory (ART) for his derivation. A simpler derivation of the filter function is based on forming the ratio of the 3-D frequency-domain acoustic Green's function (2.6) to the asymptotic 2-D frequency-domain acoustic Green's function (2.9) $\bar{G}^{3D}/\bar{G}^{2D}$. This yields the asymptotic filter transfer function for a homogeneous medium

$$\bar{G}^{2D}(\omega) = \bar{G}^{3D}(\omega) \cdot exp\left(\frac{i\pi}{4}\right)\sqrt{\frac{2\pi\sigma}{|\omega|}} \tag{3.1}$$

where σ is equal to cr (or c^2t). In the high frequency ray limit σ can be approximated as the integral of the velocity with respect to the arclength s of the ray (Miksat et al., 2008)

$$\sigma = cr = \int_s c(s)ds \tag{3.2}$$

For (3.2) to be valid in the asymptotic limit, quantity σ has to be calculated explicitly for each arrival using a raytracer (Williamson and Pratt, 1995). For piecewise homogeneous media, the integral in (3.2) takes the form (Miksat et al., 2008).

$$\int_s c(s)ds = \left(\frac{s_{tot}}{\sqrt{t}}\right)^2 = \left(\frac{s_1 + s_2 + ... + s_n}{\sqrt{t}}\right)^2 \tag{3.3}$$

It is important to note, that the general form of σ for inhomogeneous media involves both the traveltime t and the length of the associated raypath s. Eqns. (3.2) and (3.3) clearly show that amplitude is scaled neither by distance nor traveltime of events alone, but by both of them in combination. Applying an inverse Fourier transform (Aki and Richards, 2002, p. 445) yields the filter function in the time domain

$$G^{2D}(t) = \sqrt{2\pi\sigma} \cdot \left[\frac{H(t)}{\sqrt{t}} * G^{3D}(t) \right] \tag{3.4}$$

3.1.2 Practical implementation

In full waveform inversion, the velocity model is the target of the reconstruction procedure and so raytracing is not possible. Consequently, σ has to be approximated in one or other way. In the literature, only little guidance is given on practical filter implementation. Three different concepts were tested within this thesis.

FD filtering in combination with raytracing

In order to test the validity of (3.1), a windowed filter that employs a 1-D raytracer for event identification and treats each event separately was developed and applied on a simple reflection-type velocity model. To identify events, to compute their raylength and to estimate the associated scaling parameter σ, I used a public domain 1-D kinematic raytracing routine provided by the CREWES project (Margrave, 2001). Events are isolated in time windows, equal to three times that of the source pulse duration, and then individually Fourier transformed. Phase adjustment and amplitude scaling is performed in the frequency domain, separately on each event. Clearly, the windowed filter is only applicable when the velocity model is known and events are well separated in time.

FD filtering in combination with first break picking

Ernst (2007) describes a frequency domain filtering approach based on Eq. (3.1) which relies on picking first break arrival times and computing scaling factors for the picked events by approximating σ as $c^2 t$ where t is the picked traveltime and c is the average velocity of the inital traveltime tomogram. This technique can adequately correct amplitudes of the picked arrival, but fails for amplitudes of any later phase. Since the focus of Ernst (2007) is on time-domain "first arrival" full waveform inversion of georadar data, this approach might be the best solution for such a special case. Real data examples of applying Ernst's method can be found in Klotzsche et al. (2010) and Ernst (2007).

TD straight-ray approximate filtering

The frequency-domain approach of Ernst (2007) can only satisfactorily correct picked first breaks and filtering in combination with raytracing can't be applied when the velocity model is unknown. Therefore the most popular approach within the waveform inversion community is a very crude approximation of the asymptotic time-domain filter (3.4). It consists of a multiplication of each time domain trace with $\sqrt{t}$ on a sample-by-sample basis to correct amplitudes, followed by a time-domain convolution with $1/\sqrt{t}$ to adjust phases. This severe simplification can lead to additional filter errors (Section 3.1.3). Real data examples of such an approach are given by Crase et al. (1990), Pica et al. (1990), Reiter and Rodi (1996), Hicks and Pratt (2001), Shipp (2001), Belina et al. (2008), Bleibinhaus et al. (2009) and Mulder et al. (2010).

3.1.3 Limitations of asymptotic filtering

Both the frequency-domain and the time-domain expressions (3.1) and (3.4) require the high frequency ray approximation to hold. The validity of the asymptotic approximation is violated when the argument $w/r = kr = r/L$ in Eq. 2.9 gets small, that is, when the wavelength L is large or the distance r is small (i.e. in the near field).

In seismic exploration, the ray (high frequency) approximation is regularly violated. See Kravtsov and Orlov (1990) for a good review of the validity of ray theory. Examples in which wave theory is required include overlapping events (multiply reflected arrivals, caustics, bow ties), or free surface and interbed multiples interfering with primary reflections. Further problems arise when elastic phase conversions and interference between P and S waves occur. Whenever earlier or later arrivals or P and S modes start to overlap and interfere which each other, the phase difference between 3-D and 2-D propagation can no longer be taken as $\pi/4$.

The quantity σ can be calculated explicitly when the velocity model is known. This is only the case in situations where 2-D forward modelling is carried out to aid amplitude interpretation of single isolated arrivals in the far field (e.g. for seismological purposes). As mentioned in the previous Section, calculating σ is not possible in the context of full waveform inversion. Thus, usually the approximate straight-ray time-domain filter is used in waveform inversion pre-processing. This filter basically represents a straight-ray approximation of the original filter (Miksat et al., 2008) because arclength is not taken into account and events are solely scaled

by their traveltime. Consequently, errors occur, when raypaths deviate strongly from straight ray paths as is the case for multiply reflected arrivals.

Another problematic aspect of filtering in the time-domain is that phases and amplitudes are adjusted in a time-sample manner. Events of finite duration will see an erroneous amplitude scaling at any time after their onset. This effect is most significant for early arrivals (e.g. direct waves) and long wavelength events.

3.2 Filter performance appraisal

To the best of my knowledge, no studies exist in the literature, giving an extensive quantitative appraisal of accuracy of 3D-to-2D data transformation - at least in the context of full waveform inversion.

Literature on accuracy of 3D-to-2D transformation

Ernst (2007, p. 90) alludes to a thorough testing of his frequency-domain approach and suggests a good performance in far-field regimes. Pica et al. (1990) mention that they tested filter performance and claim sufficient accuracy, but neither do they show data examples nor quantitative errors. In Igel et al. (1993), a numerical example for a 1-D acoustic 5-layer model is shown to illustrate the poor performance of the filter, but the authors provide no quantitative error values. Wapenaar et al. (1992) demonstrate how filtered point source amplitudes of first and second events in a two-layer model deteriorate from line-source amplitudes but they didn't examine phase errors. Miksat et al. (2008) present a comparison of the straight-ray approximation (Section 3.1.2) and filtering combined with ray-tracing (Section 3.1.2) using a testing procedure analogous to mine. They found relative maximum amplitude errors up to 20 %. Miksat et al. (2008) tested homogeneous, layered and lens-structure models, but only considered single, isolated transmission events. Finally, Williamson and Pratt (1995) show that application of the straight-ray filter yields an amplitude error equal to the relative reciprocals of $\sqrt{\sigma}$ and its straight-ray approximation $c\sqrt{t}$. They warn of errors up to approximately 35 % for a linear gradient region in which velocity changes by a factor of two. However, they did not analyse the error numerically.

3.2.1 Testing environment

A 2-D time-domain staggered-grid visco-elastic finite-difference code and its 3-D equivalent (Bohlen, 2002) were used to compute 2-D reference synthetic seismograms and their 3-D counterparts, representing the observed field data. Two-dimensional 3-D models (see Fig. 1.1) were set up by repeating 2-D models in the y direction. I established a suit of various 2.5-D and 2-D reflection and transmission type models of increasing degrees of complexity and computed their 2-D and 3-D synthetic responses.

Finite difference algorithm and source-time function

The employed FDM algorithm is based on a fourth order discretisation in space and a second order discretization in time. Absorbing boundary conditions are implemented as a dissipative frame around the actual modelling domain in which velocities and stresses are decreased smoothly by an exponential factor (Bohlen, 2002). The source-time function which I use for finite-difference modelling is a Ricker-type wavelet, defined according to Latzel (2010)

$$s(\tau) = (1 - 4\tau^2)exp(-2\tau^2) \quad \text{with} \quad \tau = \frac{2f_c\pi}{3}\left(t - \frac{3}{2f_c}\right) \tag{3.5}$$

where t is time and f_c is the central (or dominant) frequency. The same definition is used for analytical and finite element modelling (Section 3.2.2 and Chapter 4). Expression (3.5) is known to reasonably well approximate the nature of realistic seismic sources such as explosions or sparker pulses. The maximum frequency for which the amplitude is significant is - as a rule of thumb - given by $2f_c$ (Latzel, 2010).

Acoustic and elastic seismograms were generated with the same viscoelastic code, but for acoustic modelling the density was set to a constant value of 2600 kg/m^3 and shear wave velocity was set to a very small value of 10 m/s. Viscoelastic dissipation was neglected by setting the quality factor Q to a very large value of 2×10^5.

In my analysis I didn't consider higher degrees of complexity like a free surface, source or receiver ghosts, tensor sources or more realistic source-time functions.

Modelled quantities

The physical quantity recorded in seismic experiments is usually either scalar acoustic pressure (recorded with hydrophones) or vectorial particle velocity (recorded with geophones). Acoustic pressure is proportional to the divergence of the particle velocity. The employed finite-difference forward solver allows one to directly output pressures, which are computed by summing over the diagonal components of the stress tensor (by contrast the in-house finite-element code used in Chapter 4 has an acoustic option and directly models scalar pressure fields).

Thus, most amplitudes shown in this thesis correspond to scalar pressures. In Section 3.2.7, however, some elastic experiments are shown and amplitudes correspond to particle velocities in x (horizontal) and z (depth) direction.

Grid spacing, time stepping and boundary conditions

The key task in setting up an adequate testing environment was to find a compromise between reasonable computation time for 3-D simulations and minimal contamination of obtained seismograms with boundary reflections or other numerical artifacts. The author of the FDM code provides several recommendations for temporal and spatial parameterisation and boundary thicknesses. For the constant grid size dh, he suggests

$$dh \leq \frac{V_S^{min}}{2 f_c 8} \tag{3.6}$$

where V_S^{min} is the minimum S-wave velocity, which corresponds to 8 grid points per minimum wavelength. According to the Courant criterion (Bohlen, 2002) the time-stepping interval dt for a fourth order standard staggered grid algorithm has to be chosen below

$$dt \leq \frac{6dh}{7\sqrt{D}V_P^{max}} \tag{3.7}$$

where V_P^{max} is the maximum P-wave velocity and D is the dimension of the model (2 or 3). Even though Bohlen's recommendation (3.6) for spatial discretization was generally sufficient, I mostly used at least 10 or more grid points per minimum wavelength. It was found that some reflection-type models (e.g. gradient model GAR) required an even finer discretization. In both reflection and transmission

type experiments I used a boundary size of 100 grid points with an exponential damping parameter of 1.6.

In transmission-type experiments I kept a minimum offset to the boundaries of 50 grid points for the sources and 30 grid points for the receivers. For reflection type models, minimum separation from the boundaries was 100 grid points, both for sources and receivers. Throughout this thesis I only show the active modelling domain (without boundaries). The active modelling domain dimensions were 150×150 m and 300×200 m for transmission and reflection-type experiments, respectively. In Table 1, I provide an overview of all finite difference models and their individual parameterization. A description of source-receiver geometry is generally contained in the individual model Sections.

Limited accuracy of FDM and FEM modelling

It is impossible to eliminate numerical artifacts completely. Generally, transmission-type experiments are affected to a minor degree due to the higher relative amplitudes of arrivals. However, the signal-to-noise ratio between boundary reflections and later primaries in reflection-type experiments can be relatively low. This is particularly the case in 3-D simulations, due to the more rapid amplitude decay.

Boundary conditions were thoroughly optimized only for 100 Hz experiments and just re-used for 50 Hz experiments, as they seemed to remain stable. However, it has to be noted that absorbing boundaries have the tendency to perform worse at higher distance per wavelength ratios. Therefore I advise the reader to view the RMS and maximum relative errors provided for reflection type and 50 Hz experiments under the aforementioned restrictions.

Error estimation and normalization

Amplitude values in 3-D finite-difference synthetic seismograms were smaller by orders of magnitude compared to the amplitudes in the 2-D synthetics. In order to obtain meaningful error estimates, I had to normalize 2-D and filtered 3-D gathers by a single scaling factor. I investigated several optimal scaling methods based on the ratio of root-mean-square values (RMS), standard deviations (STD), interquartile ranges (IQR) and median absolute deviations (MAD).

Approaches based on RMS or STD values appeared to place a higher weight on a good fit at the direct arrival, while IQR and MAD scaling seemed to place more emphasis on later events. As I considered matching direct arrivals as most

important, I decided to use RMS optimal scaling for all examples shown in this thesis. The error was then estimated in the time domain as the normalized root-mean-square deviation (NRMSD) of each trace. The NRMSD is given by

$$NRMSD[\%] = \frac{\sqrt{\sum_{i=1}^{n}(x_{1,i} - x_{2,i})^2/n}}{x_{max} - x_{min}} \tag{3.8}$$

where $x_{1,i}$ and $x_{2,i}$ represent the observed amplitude values and x_{max} and x_{min} are the maximum and minimum amplitudes in the data of both traces. Miksat et al. (2008) computed relative maximum time domain errors by comparing maximum phase amplitudes of 2-D and filtered 3-D data, according to the expression

$$\text{Max. TD relative error [\%]} = \frac{\left|A_{max}^{3Dfilt} - A_{max}^{2D}\right|}{|A_{max}^{2D}|} \tag{3.9}$$

I decided to use a more sophisticated error estimate, based on transformation of data to its time-frequency representation (TFR), which enables one to investigate the temporal evolution of the spectral content (Kristeková et al., 2006). Besides the possibility of examining misfits in the time-frequency plane, the method allows one to project the TF misfits back to the time domain, which yields the so called time envelope misfit (TEM) - a representation of the percental error as a function of time. Mostly, maximum TEM and the misfit given by (3.9) exhibited very comparable values.

Model parameterization, naming convention and symbolism

Throughout this thesis, I will abbreviate models with three lettered acronyms. The first letter stands for the incorporated structure (e.g. "S" for stochastic fluctuations or "L" for layers), the second letter indicates if an acoustic ("A") or an elastic ("E") medium is being considered, and the last letter refers to transmission ("T") or reflection ("R") type model. An (e) denotes an explosive source, while (x) indicates an x-directed source. In the model geometry plots, crosses symbolize sources and dots denote receiver positions. For better visibility I generally show only every fourth receiver.

Model parameterization (FDM)							
Name	dh $[m]$	dt $[s]$	N_{dt}	GP/λ_{min}	f_c $[Hz]$	x/z/y $[m]$	BC ($[m]$,exp)
HAT	0.5	5×10^{-5}	4000	15	100/50	$250 \times 250 \times 250$	50/1.6
LAR	0.5	5×10^{-5}	8000	10	100	$400 \times 300 \times 300$	50/1.6
GAR	0.25	4×10^{-5}	7000	20	100	$400 \times 300 \times 200$	50/1.6
SAT	0.5	5×10^{-5}	4000	~10	100/50/25	$250 \times 250 \times 250$	50/1.6
BAT	0.5	5×10^{-5}	4000	10	100/50/25	$250 \times 250 \times 250$	50/1.6
SAT(b)	0.5	5×10^{-5}	4000	~17	100	$250 \times 250 \times 250$	50/1.6
BAT(b)	0.5	5×10^{-5}	4000	17	100	$250 \times 250 \times 250$	50/1.6
BET(e)	0.5	5×10^{-5}	4000	10	100/50	$250 \times 250 \times 250$	50/1.6
SET(e)	0.5	5×10^{-5}	4000	~10	100/50	$250 \times 250 \times 250$	50/1.6
BET(x)	0.5	5×10^{-5}	4000	10	100/50	$250 \times 250 \times 250$	50/1.6
SET(x)	0.5	5×10^{-5}	4000	~10	100/50	$250 \times 250 \times 250$	50/1.6

Brief model description						
Name	Type	V_P $[km/s]$	V_S $[km/s]$	ρ $[t/m^3]$	Source	Description
HAT	transmission	1.5	0.01	2.6	explosive	homogeneous
LAR	reflection	1.0 - 2.0	0.01	2.6	explosive	1-D, layered
GAR	reflection	1.0 - 3.0	0.01	2.6	explosive	1-D, gradient
SAT	transmission	~1.05 - 1.38	0.01	2.6	explosive	stochastic
BAT	transmission	1.0 - 2.0	0.1	2.6	explosive	block model
SET	transmission	~1.78 - 2.35	~1.05 - 1.38	~2.10 - 2.75	(e) explosive (x) directive	elastic SAT
BET	transmission	1.7 - 3.4	1.0 - 2.0	2.0 - 4.0	(e) explosive (x) directive	elastic BAT

***Table 1**: Overview of models and their individual parameterization*

3.2.2 Model HAT: Acoustic fullspace (analytical modelling)

I started with an acoustic homogeneous fullspace model (HAT). The model is very simple and generates only straight ray paths. This allows the investigation of the fundamental asymptotic limitations, which are inherent in any 3D-to-2D data transformation procedure. Wavefield modelling in this Section is based on simple, analytical 3-D and 2-D Green's function solutions for the acoustic fullspace (Eqns. 2.8 and 2.6).

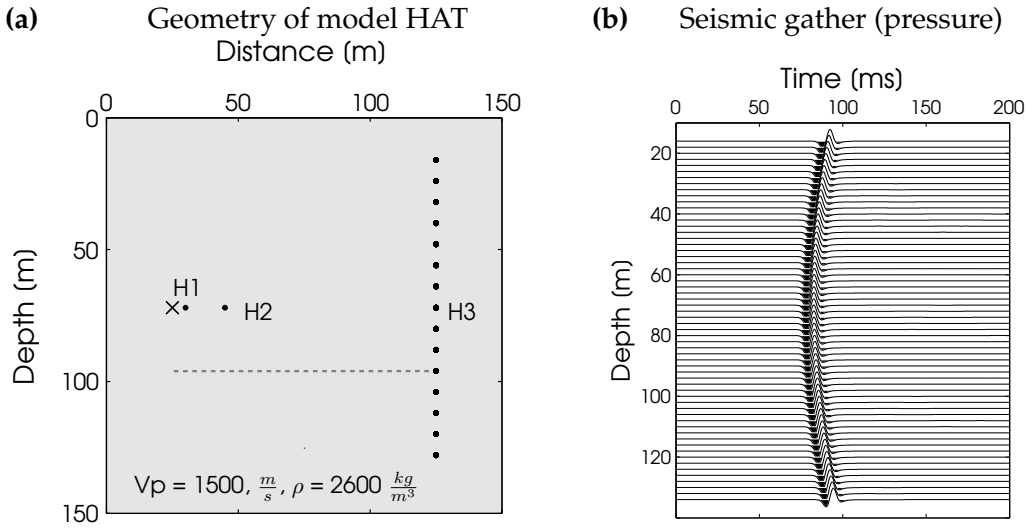

Figure 3.1: ***(a)*** *Model geometry for a homogeneous constant density acoustic fullspace (HAT).* ***(b)*** *2D finite difference synthetic seismograms obtained from finite difference numerical experiments using a Ricker wavelet with a central frequency of 100 Hz.*

First, the response at receiver H3 (Fig. 3.1) at a depth of 72 m, 100 m away from the source, is considered. 2-D and 3-D Fourier spectra are obtained by evaluating (2.6) and (2.8) for a range of frequencies up to 300 Hz. Subsequently, the 3-D Fourier spectrum is multiplied point-wise with the asymptotic frequency-domain filter (3.1) to obtain the approximate 2-D Fourier spectrum.

The scaling factor σ is determined using a source receiver separation r of 100 m and a wavespeed c of 1500 m/s. In Fig. 3.2 the 2-D (red), 3-D (blue) and filtered 3-D (green) Fourier spectra are shown up to a frequency of 300 Hz. The fit between true 2-D and filtered 3-D is good at higher frequencies, but the residual increases towards the low frequency end of the spectrum, which is most likely

because the high-frequency approximation in Eq. (3.1) breaks down.

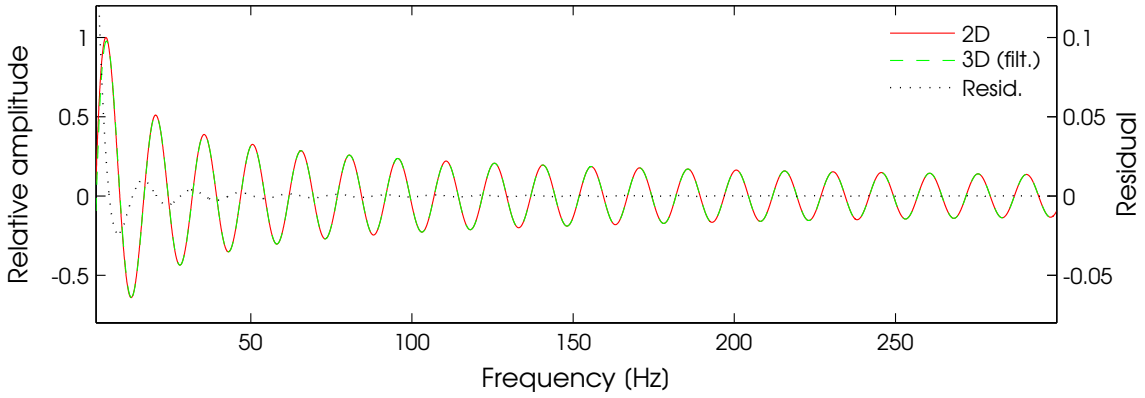

Figure 3.2: *2-D (red) and filtered 3-D (green) Fourier spectra evaluated for many values of ω and plotted as a function of frequency $f = \omega/\pi$. Due to the asymptotic nature of filter (3.1), residuals increase towards the low frequency end of the spectrum.*

To obtain a time-domain response, all Fourier spectra are multiplied with the spectrum of a 100 *Hz* central-frequency Ricker wavelet (3.5) and then inverse Fourier transformed (Fig. 3.3). There is a good match between the 2-D and the filtered 3-D solution. The relatively high residual seen near the low frequency end in Fig. 3.2 does not seem to markedly affect accuracy in the simple homogeneous case.

Next, I evaluated (2.8) and (2.6) at a fixed frequency of 100 *Hz* for many distances r along a horizontal slice, 25 m below the source (indicated by the line in Fig. 3.1 **(a)**). For better visibility, amplitudes of the 3-D and the 2-D solution are set to the same reference value 5 m away from the source. Again, an excellent fit between the 2-D and the filtered 3-D solution can be observed (Fig. 3.4).

To verify comparability of finite-difference and analytical modelling, complementary 2-D and 3-D finite-difference simulations with a central frequency of 100 *Hz* were performed. Table 1 provides details on the employed parameterization. The source is situated at a depth of 72 m and designated with a cross, whereas the 60 receivers, which are spread over the depth interval $16 - 136$ m, are denoted by black dots (see Fig. 3.1). A Ricker type source-time function with a central frequency of 100 *Hz* is employed. 2-D and 3-D finite-difference synthetic seismograms compare very well to the analytically obtained traces (see Fig. 1 in Appendix A).

Even though the frequency-domain 3D-to-2D transformation works well in model HAT, I decided to apply the straight-ray approximate time-domain filter

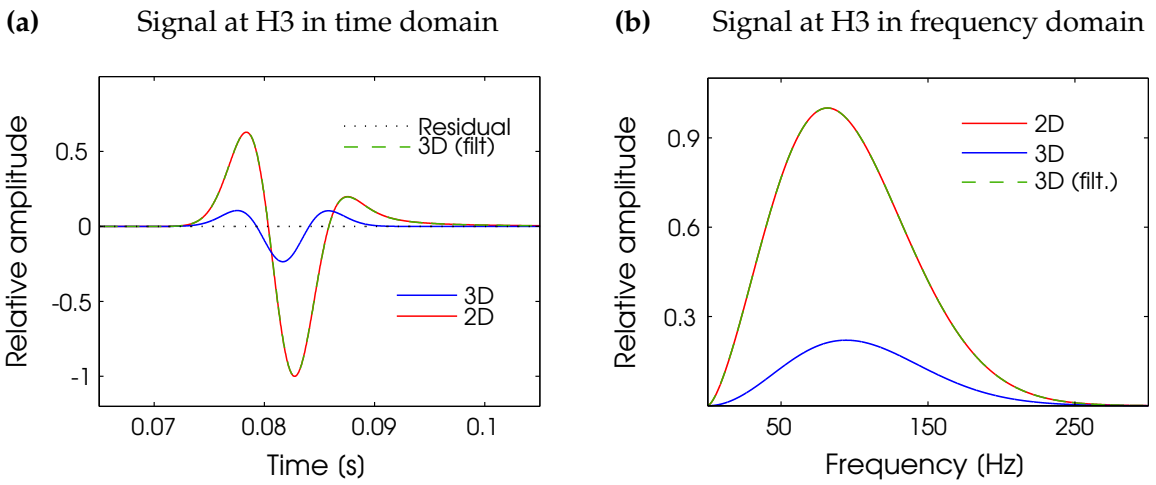

Figure 3.3: *2-D, 3-D and filtered 3-D synthetic seismograms in a homogeneous fullspace. Filtering was done using the frequency domain expression (3.1). Parameter σ is determined using the known source-receiver separation of* 100 *m and the wavespeed of* 1500 *m/s. There is an excellent fit between the 2-D (red) and the filtered 3-D (green) response. 3-D and 2-D maximum amplitudes have been set to the same value at a distance* 5 *m away from the source for better comparison.*

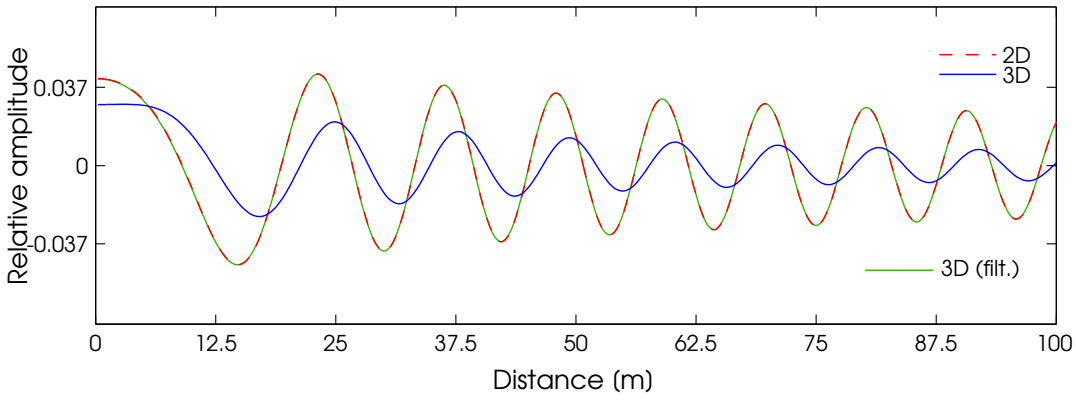

Figure 3.4: *2-D and filtered 3-D freuency domain solutions, for a fixed frequency of* 100 *Hz and many distances r along the depth slice denoted by a dashed line in Fig. 3.1. Amplitudes of the 3-D and the 2-D solution are set to the same value at a distance* 5 *m away from the source for better comparison.*

on the full synthetic 3-D gather, to examine the error due to sample-by-sample amplitude adjustment (and to obtain reference errors for all further experiments).

In Fig. 3.5 **(a)** the match of the filtered 3-D and reference 2-D maximum trace amplitudes are shown. The fit is quite poor and earlier events seem to suffer more severely from over-correction than later events. The mean normalized RMS deviation shown in Fig. 3.5 **(b)**, averaged over NRMSD values for all traces is about 0.3 % and the mean maximum TEM is about 0.9 %.

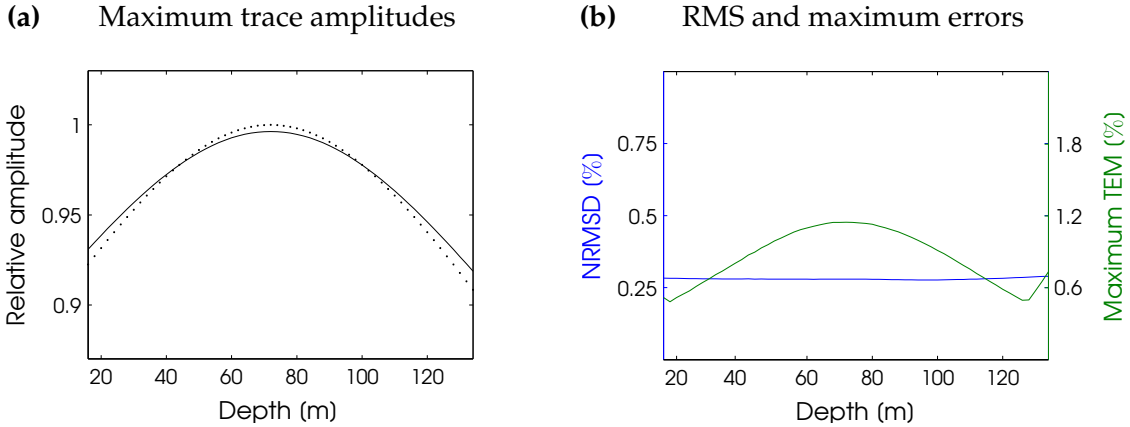

Figure 3.5: *Model HAT.* ***(a)*** *Maximum trace amplitudes of 2-D (dashed) and filtered 3D (solid) data.* ***(b)*** *Trace by trace NRMSD and maximum TEM in %.*

3.2.3 Model LAR: Acoustic fullspace with layers

As a first step towards more realistic models I defined a typical end-on reflection type acquisition geometry - representative of, for example, a shallow marine seismic survey - incorporating one-dimensional stratification. The model is purely acoustic and density is set to a constant value of 2600 kg/m^{-3} in all layers (Fig. 3.6). Layers are arranged in such a way that reflections are distinctly separated (see Fig. 3.6). Details on the finite-difference parameterization are provided in Table 1.

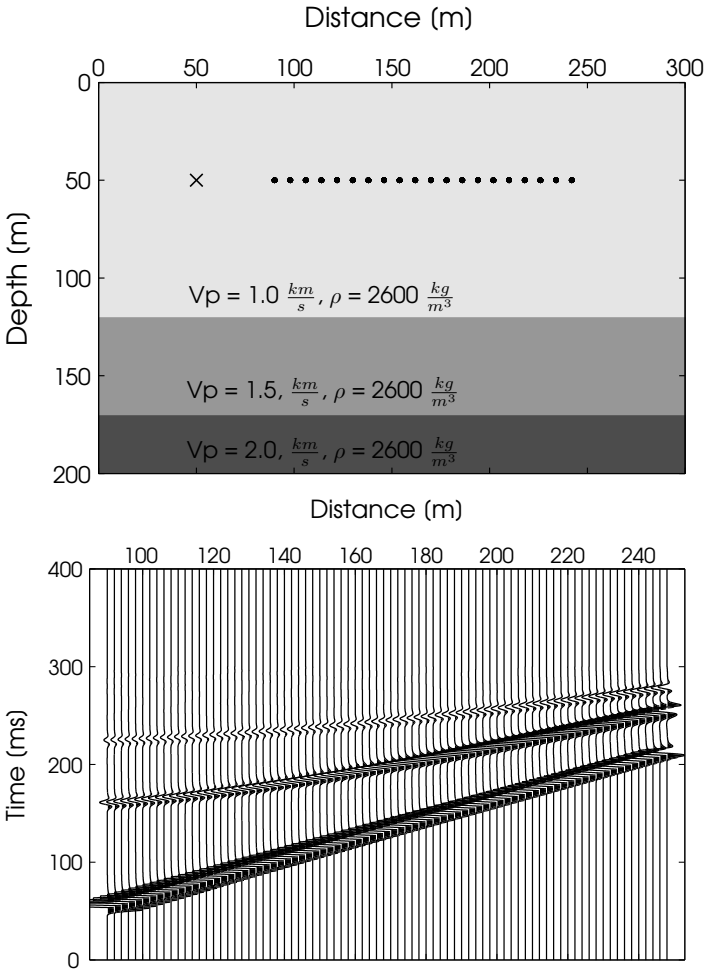

Figure 3.6: *Model geometry and seismic gather, model LAR*

(a) Geometry of model LAR. 80 sources with a spacing of 2 m are laterally spread over a total length of 160 m. Minimum offset from the source is 40 m. Velocity ranges from 1000 to 2000 m/s. A constant density of 2600 kg/m^3 is used.

(b) FDM synthetic seismic gather. Only 2-D data are shown. A central frequency of 100 Hz is used. Three clear and well separated reflection events can be identified in the data.

The one-dimensional geometry of model LAR allows to perform raytracing. Hence, I was able to directly compare all three filtering concepts, introduced in Section 3.1.2. Results are shown on a sample trace (receiver 10) at a distance of 110 m (Fig. 3.7).

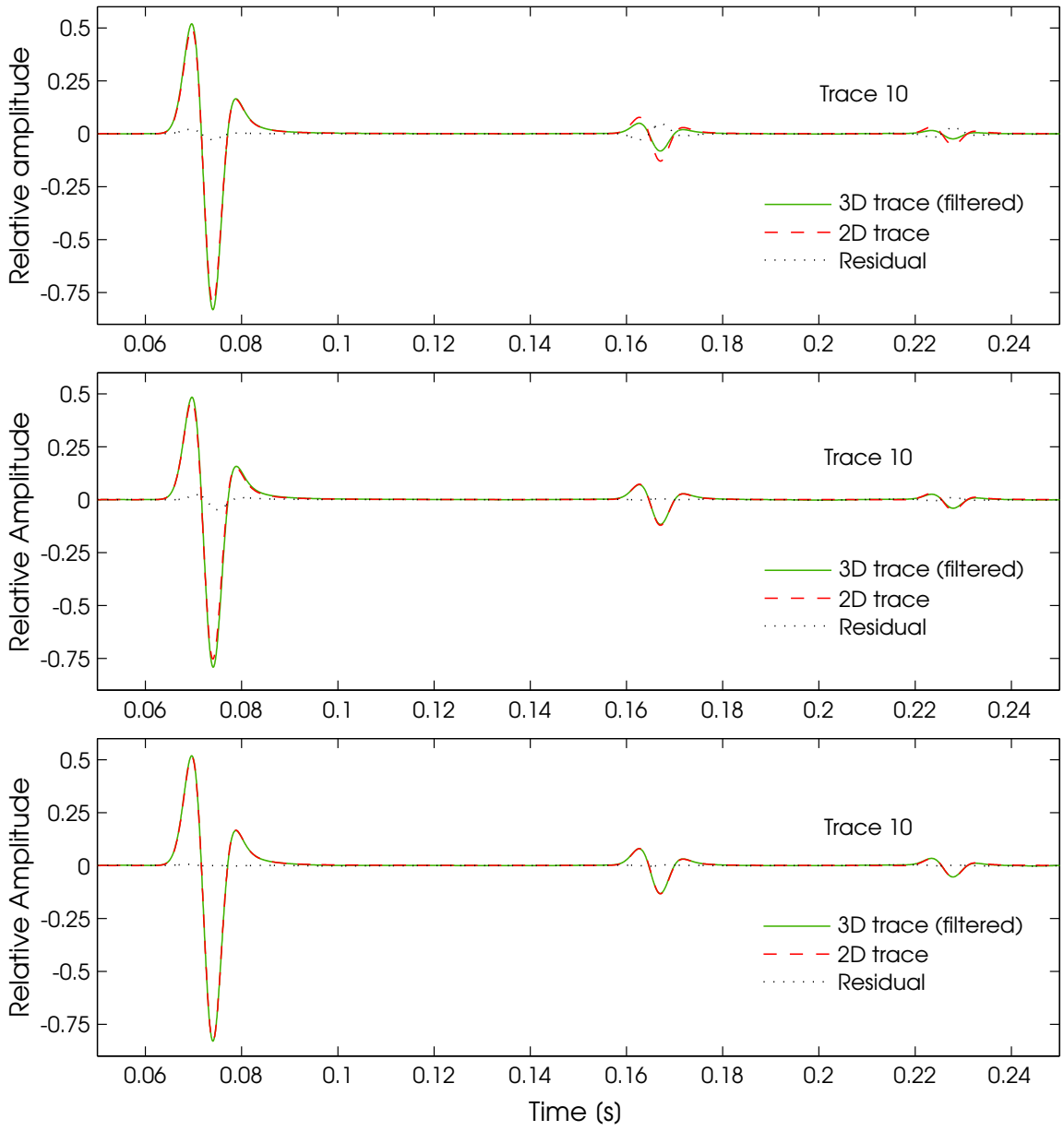

Figure 3.7: *Comparison of different filter implementations on a sample trace at a distance of* 110 *m. 2-D FDM results are drawn in red and filtered 3-D traces are drawn in green. Frequency-domain filtering with first break picking (top panel) shows over-correction for the first arrival and under-correction for the second and third arrivals. The straight-ray time-domain filter (middle panel) performs very well but shows slight over-correction for the first arrival. Only windowed filtering combined with raytracing (bottom panel) is able to correct amplitudes for all three arrivals. Phases fit very well in all cases.*

For FD filtering with event picking (top panel), traveltimes of the direct wave were picked. For any later event the filter fails to correct amplitudes, but satisfactorily adjusts phases. Straight-ray time-domain filtering (middle panel) performs quite well, but slightly over-corrects amplitudes of the direct arrival. Only windowed filtering combined with raytracing (bottom panel) is able to correct the amplitudes of all events on the trace.

In Fig. 3.8 the 2-D and the filtered 3-D amplitude and phase spectra of the sample trace, associated with data transformation using the straight-ray approximate time domain filter, are shown. Both phases and amplitudes match each other well, but errors are slightly higher towards the lower frequencies.

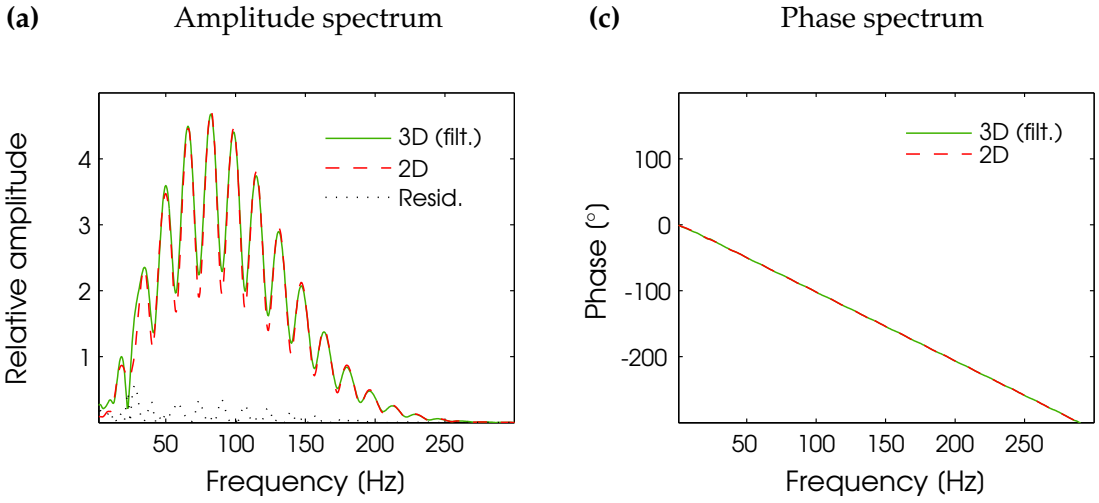

Figure 3.8: *Frequency spectrum of a sample in a distance of 110 m treated the approximate straight-ray time-domain filter.*

NRMSD errors are solely estimated between 2-D and filtered 3-D data, obtained by transformation with the straight-ray approximate time-domain filter, as this is the only filter having pratical relevance. In recognition of the fact that in reflection-type full waveform inversion, the direct wave is usually regarded as noise (Yilmaz, 1987), I muted the first event before estimating the error. NRMSD and Maximum TEM are moderate and don't exceed 0.7 % and 7 %, respectively. The mean RMS error for the full gather is ~0.6 % and the mean maximum TEM error is ~4.5 %. A trace-by-trace error comparison of RMS and maximum TEM errors is given in Fig. 3 in Appendix B.

3.2.4 Model GAR: Acoustic fullspace with velocity gradient

To further increase complexity, the middle layer in model LAR was replaced with a linear velocity gradient from 2.0 to 3.0 km/s and the velocity of the lowermost layer was changed to 1.0 km/s in order to attain a strong impedance contrast (see Fig. 3.9 **(a)**). Source-receiver geometry is analogous to model LAR (Fig. 3.6). A central frequency of 100 Hz is used. Details on the model parameterization are given in Table 1.

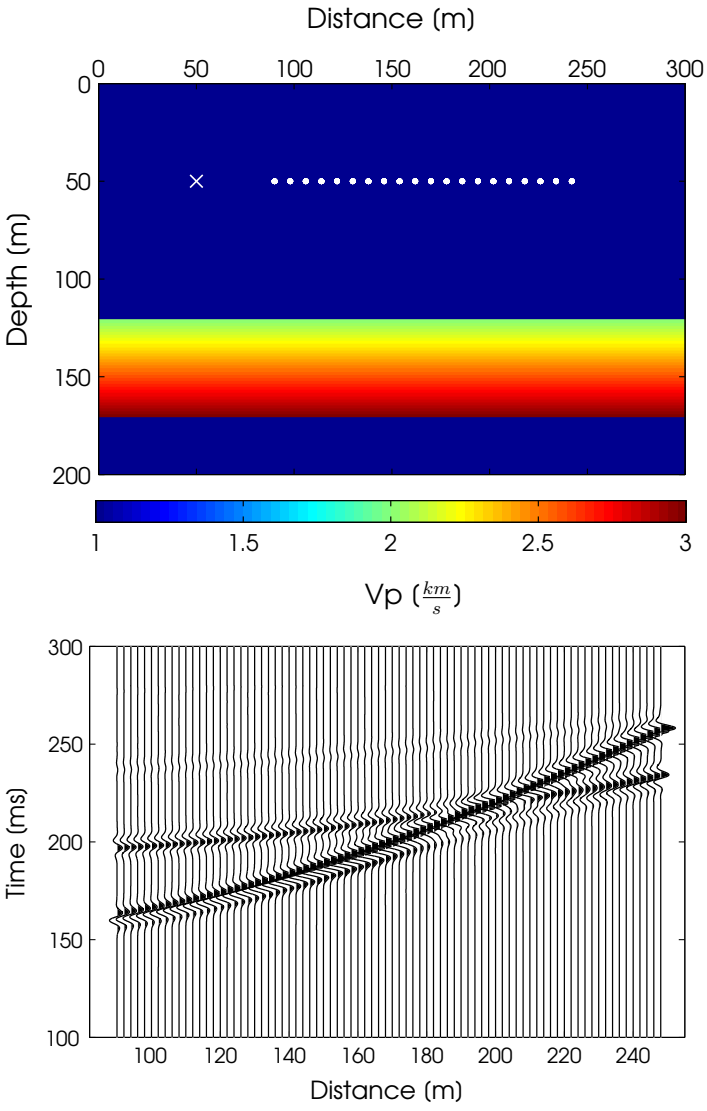

Figure 3.9: *Model geometry and seismic gather, model GAR*

(a) Model geometry of a fullspace with a velocity gradient from 2000 to 3000 m/s embedded between two layers of lower velocity. Density for all layers is constant at 2600 kg/m^3.

(b) 2-D FDM synthetic seismogram. A 100 Hz Ricker-type source wavelet was used. The second event overlaps the first event at an distance of around 190 m. A weak interbed multiple is visible around 250 ms.

The gradient geometry results in two reflections of which the second overlaps the first (see Fig. 3.9 **(b)**). This yields a more or less complicated interference

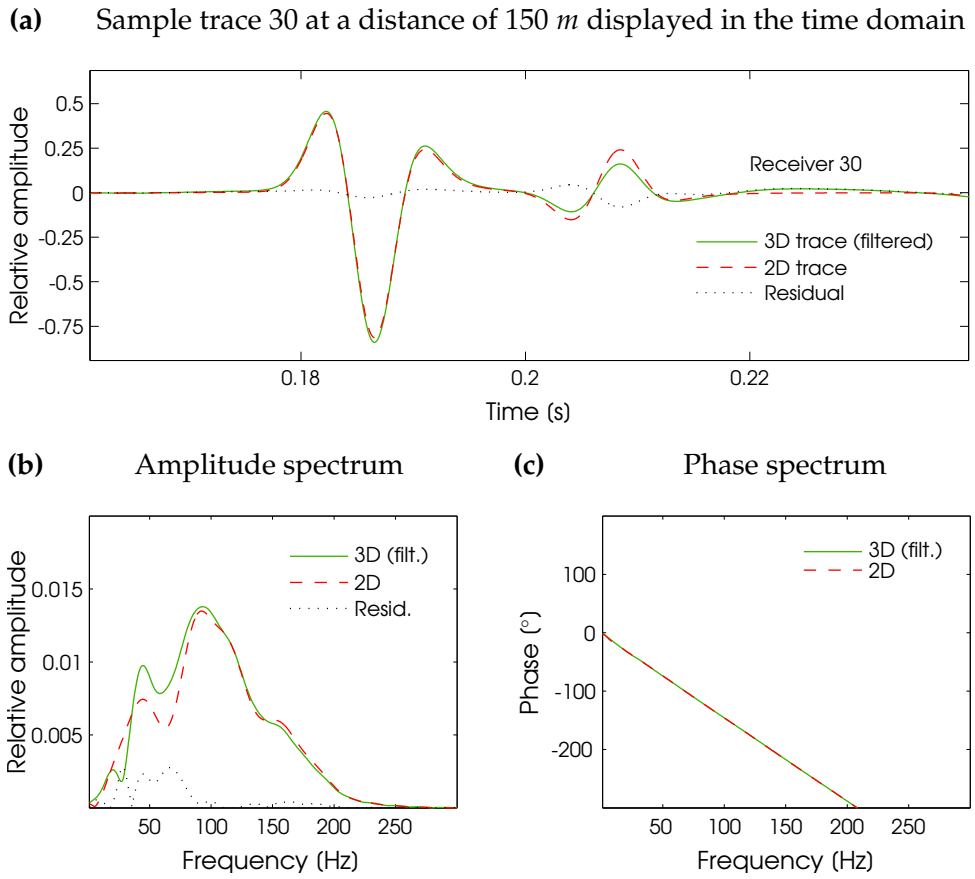

Figure 3.10: ***(a)*** *Sample trace 30 in the time domain (at a distance of 150 m). The second event, that has travelled through a velocity gradient, is under-corrected as its ray path is bent and the straight-ray assumption is violated.* ***(b)*** *Sample trace 60 in at a distance of 210 m in the frequency domain. At locations where the first and second reflection event overlap, a particularly poor performance at low frequency can be observed.*

pattern at receiver distances between 180 and 220 *m*. Arrivals associated with reflection at the lowermost boundary have travelled through the velocity gradient. Thus, their ray-paths strongly deviate from straight lines.

Again, the direct arrival is muted, before 3D-to-2D transformation is performed. The straight-ray approximate time-domain filter fails completely on the second arrival (Fig. 3.10), which is under-corrected by about 30 % (i.e. the relative time-domain misfit of the second arrival) throughout the gather. This is due to violation of the straight-ray assumption, which arises for events that have travelled through the velocity gradient (Fig. 3.11).

Both RMS and TEM values increase erratically at receivers which recorded the overlap of the second and the first reflection (Fig. 3.11 **(b)**). Interestingly, NRMSD and maximum TEM exhibit larger values at near offsets. One could speculate that this might be due to the smaller distance-per-wavelength ratio at shorter offsets. However, considering the absence of a similar pattern in the RMS errors of model LAR, this seems unlikely. The mean NRMSD value of the whole gather is ~1.2 % whereas the mean maximum TEM is ~7.5 %.

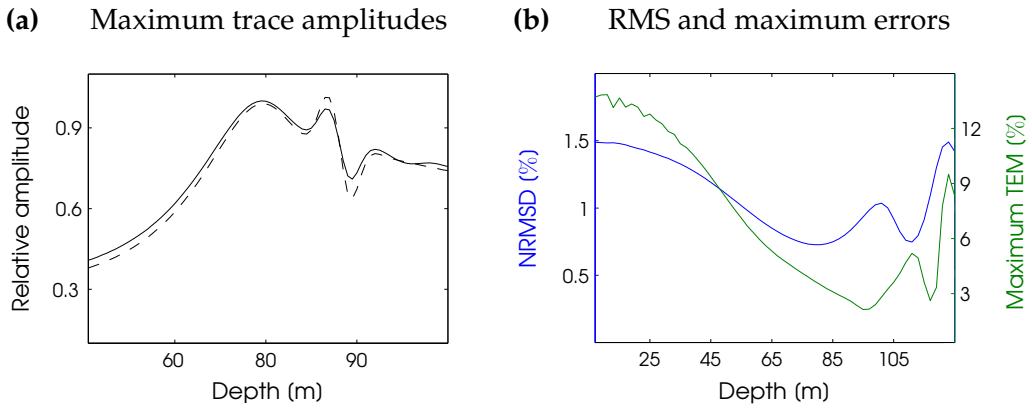

Figure 3.11: *Model GAR.* ***(a)*** *Maximum trace amplitudes of 2-D (dashed) and filtered 3-D (solid) data.* ***(b)*** *NRMSD and maximum TEM in %.*

3.2.5 Model SAT: Acoustic fullspace with stochastic fluctuations

Next I considered an acoustic fullspace model including stochastic fluctuations of 15 % around a median P-wave velocity of 1250 m/s with a Hurst (or roughness) number of 0.75, a horizontal correlation length of 23 m and a vertical correlation length of 5 m. Yet, density is constant and V_S is kepat at a low value of 10 m/s. Modelling parameters are listed in Table 1. There is a high velocity zone at shallow receivers and a low velocity zone at deep receivers. The source is located within an intermediate velocity zone. Various later phases of relatively low amplitude arrive after the first break. Simulations were performed with 100, 50 and 25 Hz central frequency, but only results for the 100 Hz simulations are shown.

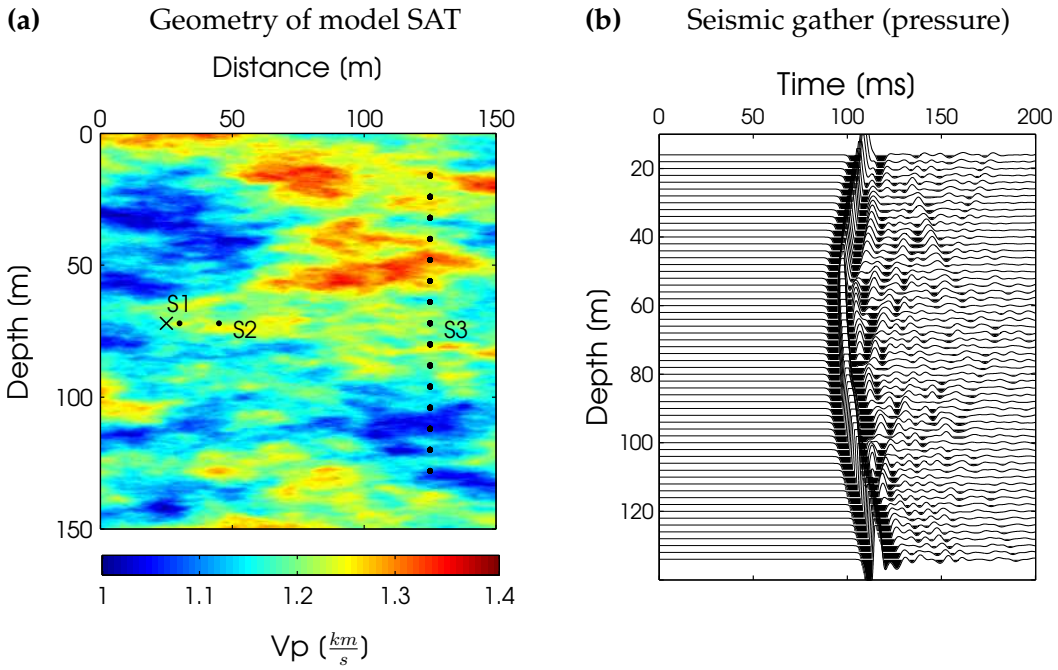

Figure 3.12: ***(a)*** *Domain of model SAT, having stochastic fluctuations.* ***(b)*** *Synthetic seismic gather obtained from 2-D finite-difference modelling with a 100 Hz central frequency Ricker-type source. Various later phases of relatively low amplitude arrive after the first break.*

Interestingly, model SAT seems to be surprisingly forgiving in regard to filtering errors. Maximum trace amplitudes of 2-D and filtered 3-D data fit each other very well and NRMSD and maximum TEM generally stay below 0.5 and 2.0 %, respectively (Fig. 4). The mean NRMSD of the whole gather is ~0.3 % and the

mean maximum TEM is ~1.8 %. This is comparable to the errors observed in the homogeneous fullspace HAT and well within the expected range of precision of the numerical algorithm. The sample trace 30 at a depth of 74 *m* illustrates the very good fit between 2-D and filtered 3-D data in the time and in the frequency domain (Fig. 3.13). A reason for these relatively low errors might be that stochastic fluctuations tend to rectify effective travel paths and lead to rays that are essentially straight.

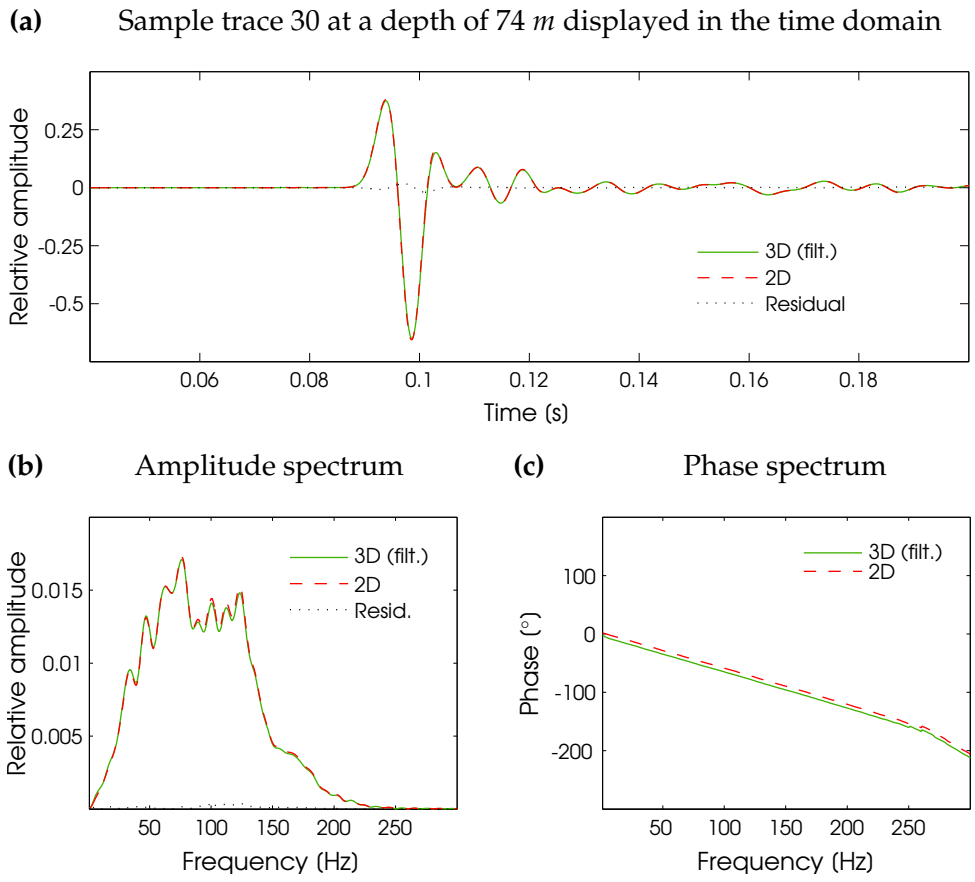

Figure 3.13: *Sample trace 30 at a depth of 74 m.* ***(a)*** *2-D (red) and filtered 3-D (green) data in the time domain. There is relatively good fit between 2-D and filtered 3-D traces.* ***(b)*** *The same trace in the frequency domain. Amplitude and phase spectra of 2-D and filtered 3-D compare very well. It might be that the strong degree of heterogeneity tends to straighten the effective ray paths.*

3.2.6 Model BAT: Acoustic fullspace with high contrast blocks

As the fifth test case I embedded low and high velocity rectangular blocks in a constant velocity background medium. This model might, for example, mimic seismic experiments performed close to engineered structures (e.g. artificial cavities, tunnels or foundations). Source and receiver geometries are defined as in the models HAT and SAT. Density is constant and V_S is kept at a low value of 10 m/s. Table 1 provides an overview of the finite difference parameterisation. Simulations are performed with 100, 50 and 25 Hz central frequency, but only results for the 100 Hz simulations are shown. The model geometry and a 2-D synthetic seismic gather are displayed in Fig. 3.14.

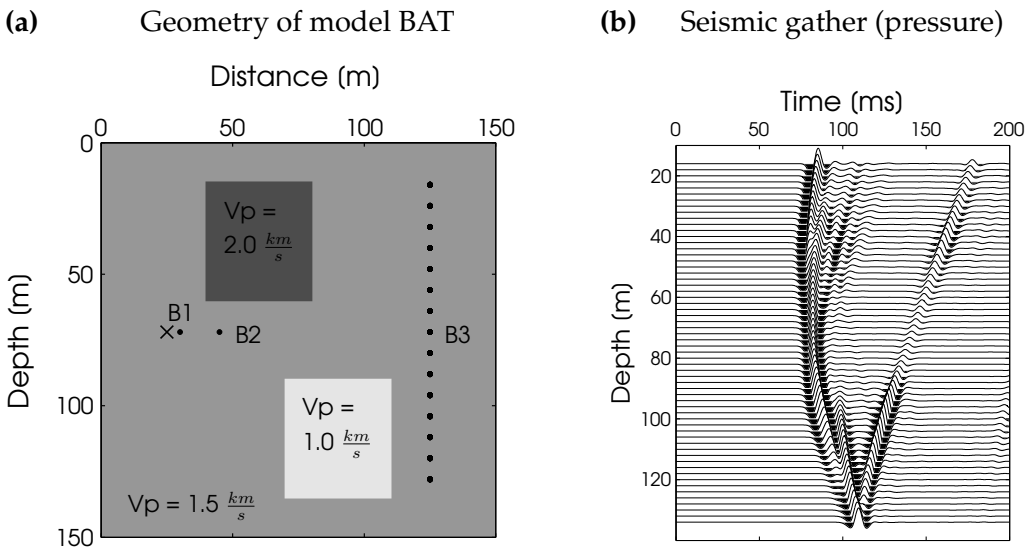

Figure 3.14: ***(a)*** *Geometry of model BAT. One low and one high velocity block are embedded in a constant velocity background. Density is set to a constant value of 2600 kg/m^3.* ***(b)*** *Associated seismic gather obtained from 2-D finite-difference modelling with a 100 Hz dominant-frequency Ricker wavelet. In the lower half of the gather, strong interference occurs between earlier and later phases.*

Filter performance is worse than in model SAT. For central receivers the ray path is more or less straight. Thus, only little interference occurs and NRMSD values stay below 1 % (Fig. 3.15). However, especially at shallow and deep receivers, where first arrivals have travelled through low or high velocity regions and interfere occurs with later phases, results are slightly degraded. Mean NRMSD error

is ~0.8 % and the mean maximum TEM error is ~7.6 %, which is comparable to model LAR (see Fig. 5 in Appendix B).

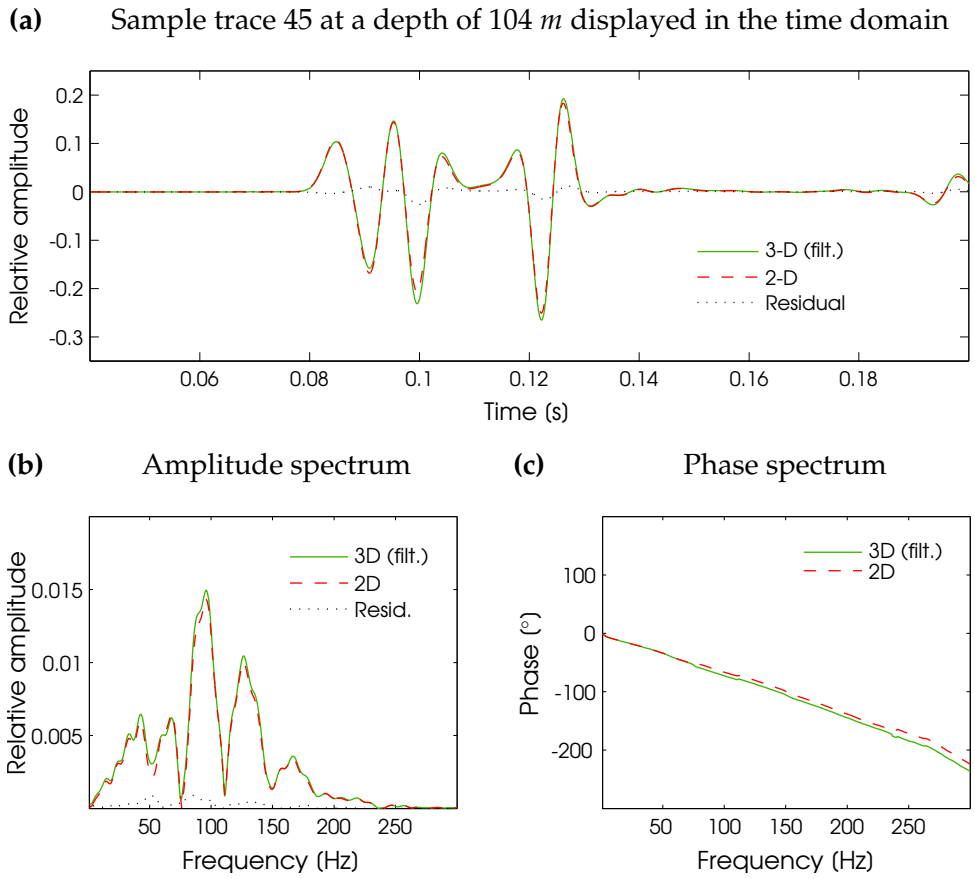

Figure 3.15: *Sample trace 45 at a depth of 104 m.* ***(a)*** *2-D (red) and filtered 3-D (green) data in time domain. Events have travelled through a low velocity region. Fit between 2-D and filtered 3-D is not as good as for model SAT.* ***(b)*** *and* ***(c)*** *Amplitude and phase spectra of the same trace shows some differences.*

.

3.2.7 Elastic experiments (Model BET and SET)

As a final example, I considered full elastic wavefields, propagated through modified versions of models BAT and SAT. I introduced elasticity in model SAT (Section 3.2.5) and BAT (Section 3.2.6) by setting their S-wave velocities (which had been fixed at an unphysical value of 10 m/s for all acoustic experiments) to the original P-wave velocities and setting the new P-wave velocities to the original values multiplied by a factor of 1.7, which is a typical V_P/V_S ratio for crustal rocks (corresponding to a Poisson's ratio of ~0.25).

Simulations were performed both with an omnidirectional source and an x-directed source. The x-directed source generates a considerable amount of shear components. Associated phase conversions and energy leakage into elastic modes can make the wavefield highly complex because severe interference can occur between P and S waves.

In both model BET(x) and SET(x), a clear S-wave, arriving shortly after the direct P-wave arrival and strongly interfering with later portions of the seismic gather, can be observed (indicated by arrows in Figs. 3.16 and 3.19). Due to the high degree of phase modification, interfering and overlapping events, a large influence on the accuracy of 3D-to-2D transformation is expected.

It is important to note that increasing the P-wave velocity by itself will aggravate the conversion error, as the dominant wavelength is increased. Thus I performed additional acoustic experiments (SAT(b) and BAT(b)) where solely the P-wave velocity was increased by a factor of 1.7 (while V_S was kept at 10 m/s). All the elastic results have to be seen relative to error values obtained for models SAT(b) and BAT(b).

Snapshot analysis (not shown) didn't show a worsening of boundary effects or other numerical artifacts. Hence, I remained with the finite-difference parameterization which I used for acoustic experiments (see Table 1). Unlike to all the acoustic examples, not scalar pressure but vectorial particle velocity in the x, z and y direction is acquired (computed). Obviously, 2-D simulations only yield particle velocities in x and z direction. As the straight-ray approximate time-domain filter works on a pure sample-by-sample basis, no modifications had to be done to apply it to particle velocities.

Mean NRMSD errors are ~0.6 % and ~1.5 % for SET(e) and BET(e) when an omnidirectional (explosive) source is used. This is about twice the error values observed in models SAT(b) and BAT(b). However, using an x-directed source, causes the mean RMS errors to soar to values of ~1.9 and ~2.8 % for SET(x) and BET(x), re-

spectively. Maximum relative time-domain errors peak at ~35 % in model SET(x) and ~36 % in model BET(x). The associated maximum TEM mean is ~16.4 % and ~28.2 % for model SET(x) and model BET(x), respectively. All error values in this paragraph are related to particle velocities in x direction and 100 Hz simulations.

Sample traces 30 (Fig. 3.21; Model SET(x)) and 45 (Fig. 3.18; Model BET(x)) reveal major deviations between the 2-D and the filtered 3-D solution - both in the time domain and in the frequency domain. For model BET(x), a considerable phase discrepancy is observed. Comparison of multiple traces along the receiver spread indicate a better performance for the z component of the wavefield (see Figs. 3.17 and 3.20). This is the case, both for model BET(x) and for model SET(x).

For model BET(x), the results at receivers located behind the low velocity zone show a particular strong degradation. This is most likely due to the fact that the low-velocity zone produces shorter wavelengths and tends to "compress" the wavefield, resulting in more overlap of arrivals, whilst in the high-velocity zone the events rather get "stretched" out. In Figs. 7 and 6 in Appendix B, I provide a complete compilation of trace-by-trace NRMSD and maximum TEM errors for models SET(x), SET(e), BET(x) and BET (e).

(a) Seismic gather, x comp. **(b)** Seismic gather, z comp.

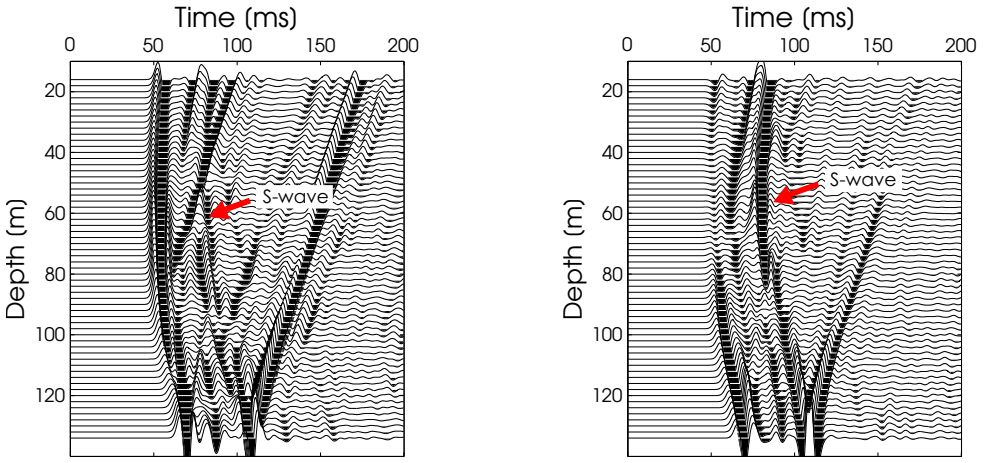

Figure 3.16: *Model BET(x). 2-D synthetic seismic gathers (particle velocities in x and z direction) obtained from finite-difference modelling with an x-directed source. The wavefield is considerably more complicated than in model BAT and exhibits strong interference and phase modification. A clear S-wave arrival covering later portions of the wavefield is visible in both the x and the z component.*

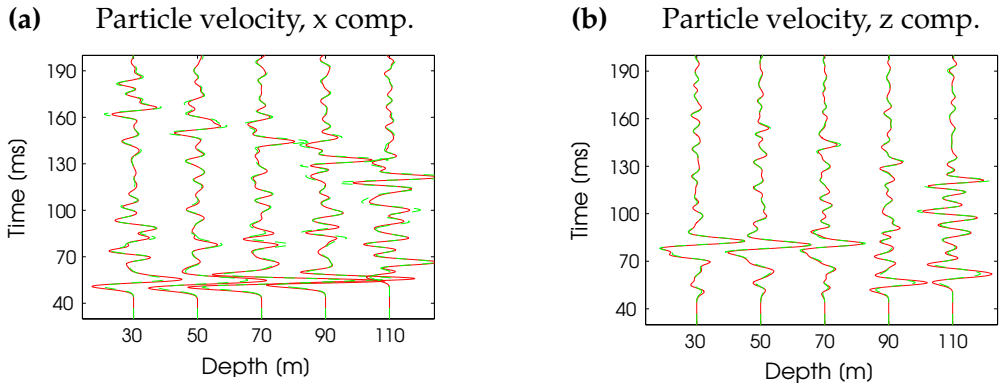

Figure 3.17: *Model BET(x): Trace-by-trace comparison of 2-D (red) and filtered 3-D data (green). An x-directed source has been used.* ***(a)*** *Particle velocity in x direction.* ***(b)*** *Particle velocity in z direction. The largest misfits occur at receivers located behind the low-velocity zone.*

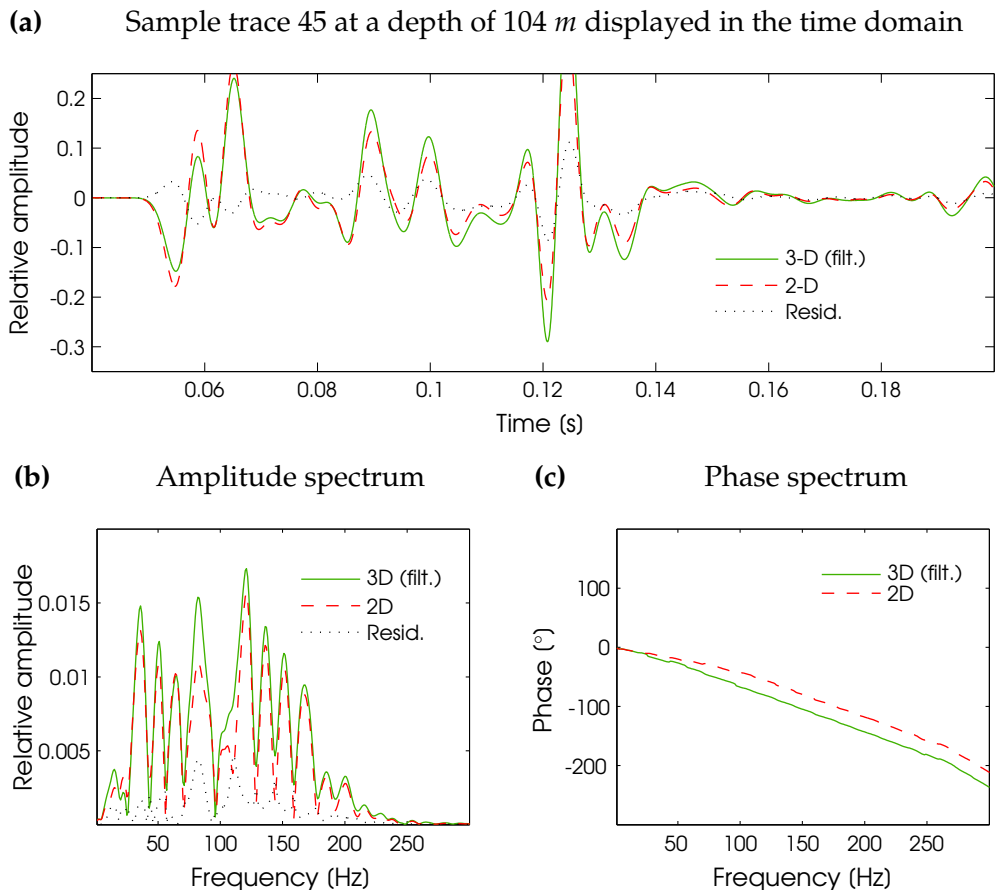

Figure 3.18: *Sample trace 45 in a depth of 104 m for model BET(x). Misfits in the time and the frequency domain are significant. As opposed to most other models, where phases tended to match each other relatively well, here a clear phase distortion can be observed.*

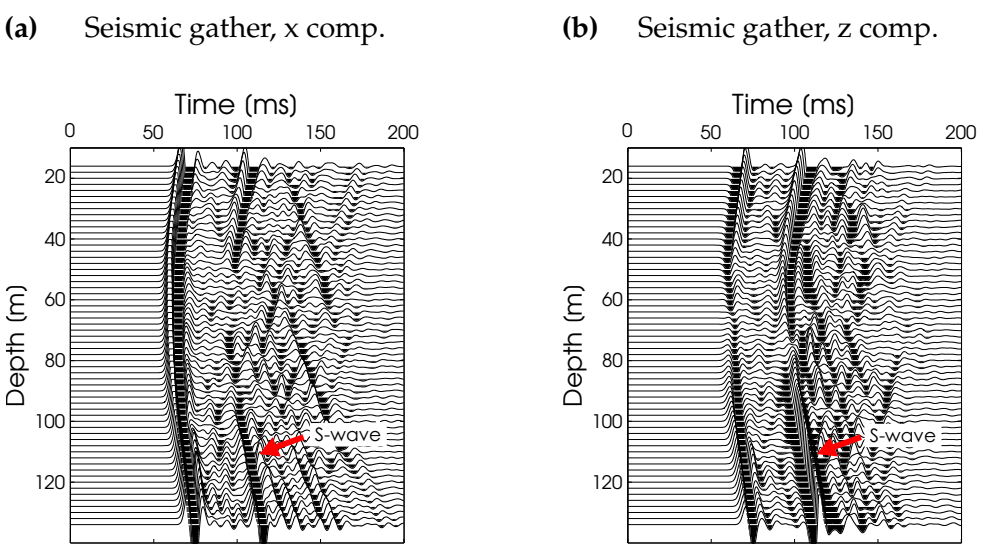

Figure 3.19: *Model SET(x). 2-D synthetic seismic gathers (particle velocities in x and z direction) obtained from finite-difference modelling with an x-directed source. The wavefield is considerably more complicated than in model SAT and exhibits strong interference and phase modification. A clear S-wave arrival, covering later portions of the wavefield, is visible in both the x and the z component.*

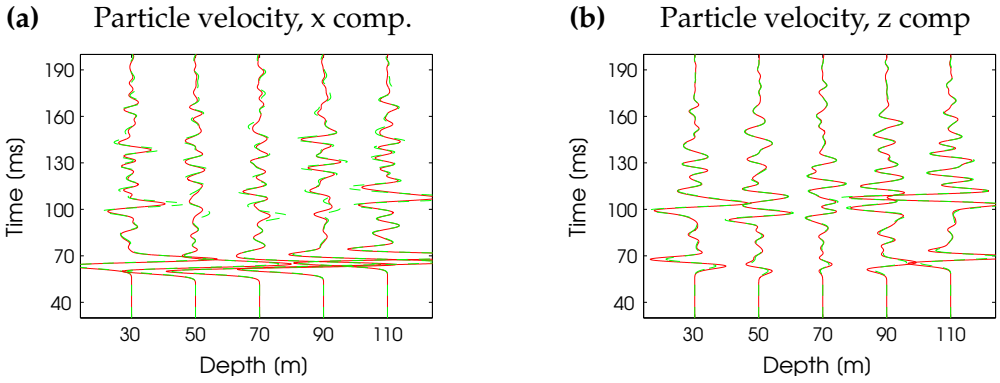

Figure 3.20: *Model SET(x): Trace-by-trace comparison of 2-D (red) and filtered 3-D data (green). An x-directed source has been used.* ***(a)*** *Particle velocity in x direction.* ***(b)*** *Particle velocity in z direction. Discrepancies are smaller than in model BET(x) but still significant.*

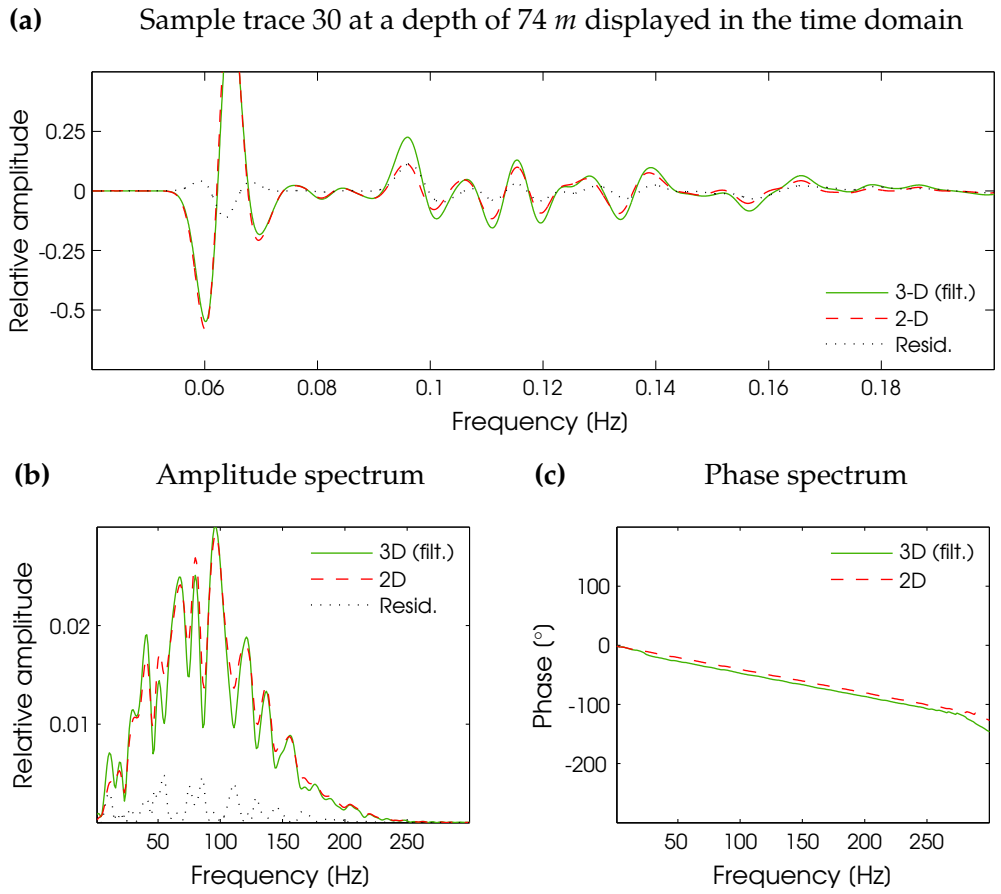

Figure 3.21: *Sample trace 30 in a depth of 74 m for model SET (x-directed source). Misfits in the time and the frequency domain are significant, but phases match each other slightly better than in the case of model BET(x).*

3.3 2-D acoustic trial-inversion of filtered data

In order to examine the influence of incorrect 3D-to-2D data transformation on the model reconstruction with a full waveform inversion routine, I performed a test-inversion for the high contrast block model BAT. Since a comprehensive inversion study was not planned to be an integral part of this thesis, inversion experiments were not extended to a wider range of models.

3-D and 2-D finite-difference seismograms were propagated for 15 source positions with a separation of 8 *m*, starting at a depth of 16 *m* (denoted by black crosses in Fig. 3.22) and 60 receivers, using the same time-domain FDM code, that was used for all previous simulations. Again, a Ricker-type source wavelet was used. 3-D gathers were converted to approximate 2-D sections, using the straight-ray approximate time-domain filter. Both filtered 3-D and true 2-D data were then inverted with a 2-D acoustic frequency-domain FEM inversion code.

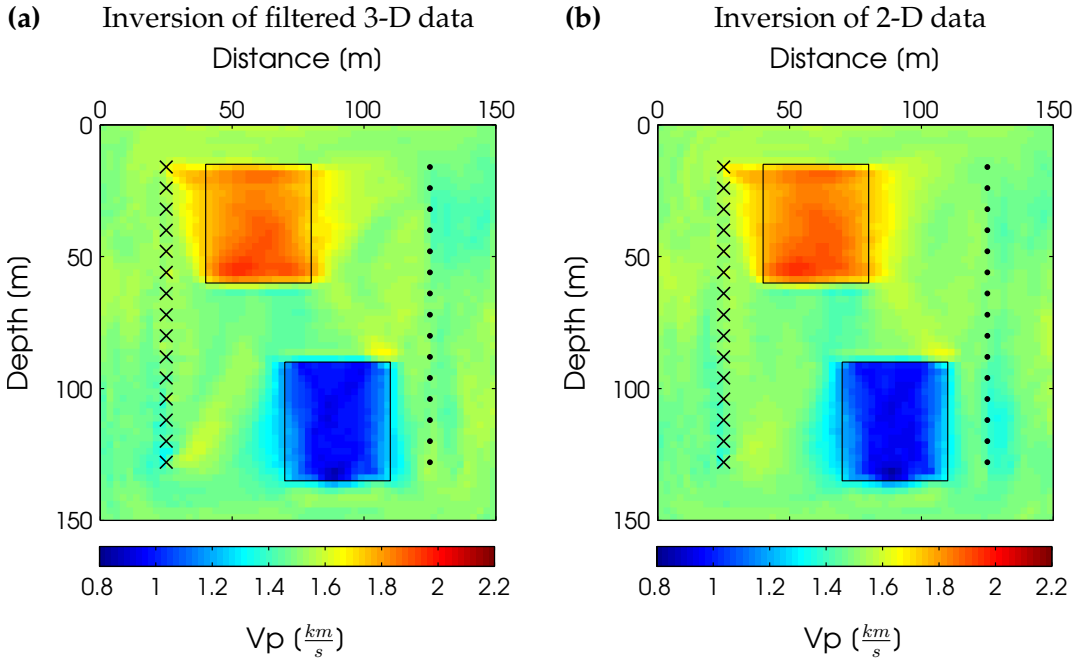

Figure 3.22: *Acoustic 2-D full waveform inversion performed on synthetic 2-D* ***(b)*** *and filtered 3-D* ***(b)*** *data from model BAT. Model reconstructions after 80 iterations are shown. Nine frequencies between 20 and 260 Hz on were used. Some discrepancies are visible, but generally, the quality of estimated models is comparable.*

In my inversion strategy, I closely follow that described by Marelli et al. (2011), in which the author investigates the deleterious effects of acoustically inverting

elastic data. The finite-element forward solver that is employed in the waveform inversion code was found to be significantly more sensitive to grid dispersion than the previously used FDM code. Thus, it was not possible to re-use the finite-difference grid of model BAT ($dh = 0.5\ m$). I refined the FEM forward grid to a gridspacing dh of 0.125 m, corresponding to more than 50 grid points per minimum wavelength. The ratio between the (both rectangular) inversion and forward grids was set to a value of 10.

To simplify the procedure, I didn't include source wavelet estimation in the inversion and assumed a known Ricker-type source with a central frequency of 100 Hz. As a starting model, a strongly smoothed version of the true model was used (not shown). My frequency schedule involved 9 equally spaced frequencies between 20 and 260 Hz with an increment of 30 Hz. Frequencies are fed into the inversion procedure in a step-wise manner, starting with low and advancing to high frequencies. Each time a new frequency component is added, smoothing and damping parameters are increased, and lowered accordingly, as the inversion progresses (Marelli et al., 2011).

As can be seen in Fig 3.22, the model reconstructions obtained by inverting the filtered 3-D and the 2-D data were comparable to a large extent. Only a very close look reveals some minor discrepancies. This indicates, that 3D-to-2D transformation using asymptotic filters, might be an acceptable alternative as long as the acoustic approximation is met. Unfortunately, I wasn't able to extend the inversion part of this thesis to the elastic case, as I was limited in time and computational resources. I expect adverse effects in inversion to be much stronger, when full elastic treatment is considered.

3.4 Summary of filter appraisal

An assessment of the validity of 3D-to-2D transformation with asymptotic filtering procedures has been performed. In Fig. 3.23 the main results of Chapter 3 are summarized in terms of mean NRMSD values for full seismic gathers. Acoustic experiments are drawn in green shades and elastic experiments are colored in blue. Lighter and darker colors indicate higher and lower frequencies, respectively. Mean NRMSD values range between 0.3 % for model HAT with 100 Hz up to 5 % for model BET(x) with 50 *Hz* central frequency. Maximum TEM errors up to 40 % are observed in model BET(x). In recognition of the fact that any numerical algorithm is only of finite exactness, I regard RMS error values below 0.5 % to be within the range of accuracy of the employed 3-D and 2-D FDM algorithms.

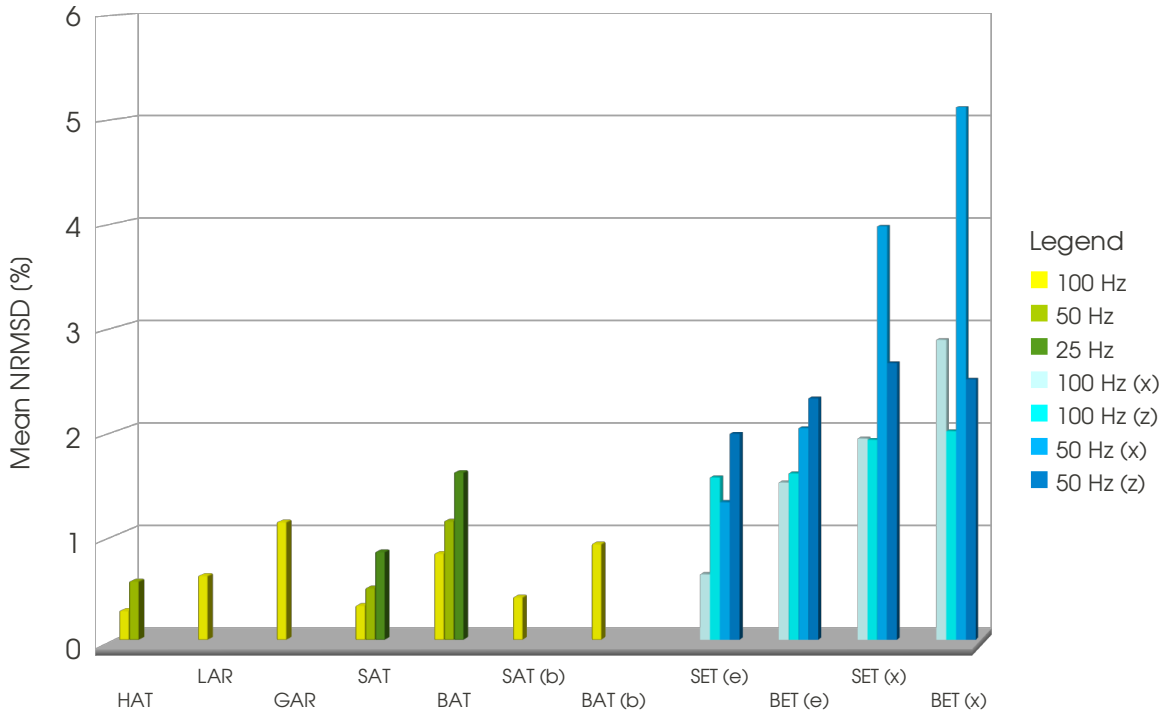

Figure 3.23: *Summary of assessment of 3D-to-2D filter validity. Mean NRMSD errors for full seismic gathers are shown. A discussion is provided in the text.*

The strongly heterogeneous acoustic model SAT exhibits mean NRMSD values of ~0.3 %, which is inside the assumed range of precision of the numerical algorithm and very similar to the error that was observed for the homogeneous fullspace model HAT. Apparently, stochastic media are relatively forgiving in this matter. It is likely that the high degree of heterogeneity to a greater or lesser extent

"straightens" out effective raypaths which is favorable for the straight-ray approximation, implicit in the data transformation.

The high contrast block model BAT exhibits a slightly increased mean NRMSD of ~0.8% which is approximately three times the error found for model SAT, and slightly higher than what is assumed to be the intrinsic error of the used FDM code. Trace-by-trace errors reveal that most of this increase originates from relatively high discrepancies at traces, situated behind a low velocity zone, at which two arrivals overlap. Generally, the low velocity zone tends to "compress" the wavefield, resulting in a higher amount of interference, while the high velocity zone rather "stretches" out the wavefield and separates events.

The simple one-dimensional reflection type model LAR exhibits an acceptable mean NRMSD error of ~0.6 %. The slightly more complex model GAR, which includes a linear velocity gradient that generates a secondary reflection overlapping the first one, shows mean NRMSD errors of ~1.2 %. The second arrival, which has travelled through the velocity gradient, strongly violates the straight-ray assumption. Thus, it is generally under-corrected and shows a relative time-domain misfit of about 30 % throughout the gather. Furthermore, the errors are accentuated where the overlap occurs (see Figs. 3.10 and 3.11).

When full elastic treatment is considered, elastic mode conversions and energy leakage into different elastic modes make the wavefield much more complex, with severe interference occuring between P and S waves (see Fig. 3.16 or 3.19). Due to the high degree of phase modification, interfering and overlapping events, the mean NRMSD errors for models SET(x) and BET(x) increase up to 1.9 % and 2.8 % for omnidirectional 100 *Hz* experiments. The associated mean maximum TEM errors are ~16.4 % and ~28.2 % for models SET(x) and BET(x), respectively.

Chapter 4

2.5-D Modelling with complex frequencies

2.5-D modelling is based on Fourier transforming the wave equation along the y axis to the time-wavenumber domain or the frequency-wavenumber domain and solving the resulting 2-D problem for many k_y-components (Song and Williamson, 1995; Zhou and Greenhalgh, 1998b; Novais and Santos, 2005; Sinclair, 2009). Theoretically, 2.5-D modelling yields wave fields with point-source spreading behaviour at much lower computational costs than full 3-D modelling. The major advantage of 2.5-D modelling are the significantly reduced memory requirements, as the problem is broken down to solving a high number of 2-D problems. On the other hand, total run time increases with the amount of wavenumbers that are used, which makes the k_y sampling strategy crucial for computational efficiency.

4.1 Critical wavenumbers in 2.5-D Modelling

For frequency-domain 2.5-D modeling, only some of the papers cited above allude to the complex oscillatory nature and pole like behaviour at certain critical k_y values in the wavenumber spectra. Generally, the wavenumber spectra oscillate gently at lower wavenumbers and more strongly at higher wavenumbers. As shown in Section 2.1.3, the 2.5-D acoustic frequency-domain fullspace solution (2.11) is split into an evanescent part for $k_y > w/c$, in which the solution is non-oscillatory, and an oscillatory part for $k_y < w/c$. Evanescent waves in particular dominate in the near-field but at source-receiver distances of many wavelengths they are negligible.

A singularity is present when k_y approaches w/c_{min}, which appears as a steep, erratic disruption in the wavenumber spectrum. While for a homogeneous acoustic fullspace only one singularitiy is present, similar poles occur in more complicated situations. For example, the homogeneous isotropic elastic case exhibits two singularities at $k_y = w/c_s$ and $k_y = w/c_p$ where c_s is the shear wave velocity and c_p is the P-wave velocity (Latzel, 2010). For strongly heterogeneous or anisotropic media, the situation becomes even more complex with multiple and directionally-dependent critical points, contaminating the wavenumber spectra (Sinclair et al., 2011). Generally, the maximum critical wavenumber corresponds to the slowest wavespeed in the medium. Throughout Chapter 4, any wavenumber k_y which is associated with a singularity will be referred to as a "critical wavenumber".

The degree of oscillation in the wavenumber spectrum not only increases at higher wavenumbers but also with increasing frequency f and increasing source-receiver separation r. Thus, the required number of samples to accurately capture the behaviour in strongly fluctuating parts of the k_y spectrum near critical wavenumbers, is not only dependent on the nature of the medium but also on the experimental geometry and the bandwidth of used frequencies.

4.1.1 Equidistant wavenumber sampling

All numerical and analytical modelling examples that are presented in this Chapter were performed in the acoustic approximation. I employed an equidistant wavenumber sampling strategy, very similar to the one described by Latzel (2010, p. 130), albeit not taking into account source receiver spacing. The largest k_y sample considered, is chosen according to the formula

$$k_y^{max} := 1.2\frac{2\pi}{L_{min}} \tag{4.1}$$

with $L_{min} = \frac{c_{min}}{f}$ where L_{min} is the minimum wavelength, c_{min} is the minimum acoustic wavespeed and f is the specified frequency. The wavenumber sampling density Δk_y is determined from

$$\Delta k_y := \frac{k_y^{max}}{n_{k_y}} \tag{4.2}$$

where n_{k_y} is the desired number of k_y samples. For the model having stochastic fluctuations (SAT) the sampling strategy (4.1) resulted in a relatively large k_y^{max} and

more than 25 % of (useless) sampling points, falling beyond the maximal critical wavenumber that was actually present in the data (see for example Fig. 4.12). This is most probably due to the fact that the highest observed critical wavenumber is usually rather determined by the wavespeed near the source region, and not by the minimum wavespeed of the whole medium (Latzel, 2010; Greenhalgh et al., 2009). This might be considered when establishing a more efficient sampling strategy.

As already mentioned, a larger number of k_y samples is required for large offsets and small wavelengths. In my analysis, this was not taken into account and I decided to define a fixed number of wavenumber samples for all frequency components. Clearly, the quantities f and r_{min} should be involved in defining a more efficient sampling strategy.

4.1.2 Problems associated with critical wavenumbers

The effect of singular values at critical wavenumbers on the frequency-domain solution is illustrated in Fig. 4.1 where the 3-D frequency-domain Green's function solution for an acoustic fullspace (2.6) is compared to an approximated 3-D solution obtained from evaluating the analytic 2.5-D Green's function solution, summed over 64 wavenumber components (2.11), at a specified frequency of 150 Hz.

The source-receiver geometry is analogous to the high contrast block model HAT (Fig. 3.1) and the acoustic wavespeed is 1500 m/s. Figure 4.1 gives the wavefield along a horizontal slice (indicated by the dashed line) situated in a 2-D grid with a grid spacing of 0.25 m. The true 3-D solution is marked by the blue line, while the 2.5-D solution is drawn in magenta. The two curves do not match closely. When the frequency f is doubled to 300 Hz, whilst retaining 64 k_y samples, the effect on the reconstructed frequency-domain solution and hence the discrepancy with the true solution is even more pronounced (see Fig. 4.2).

Figure 4.3 shows wavenumber spectra, extracted from the 2.5-D fullspace solution, 5 m (H1, top), 20 m (H2, middle) and 100 m (H3,bottom) away from the source. The increasing degree of oscillation at higher k_y values and the steep behaviour near the critical wavenumber $k_y = 2\pi \cdot (150\ Hz)/(1500\ m/s) = 0.6283\ 1/m$ is clearly visible. Thin black lines correspond to a reference sampling density, comprising 2048 k_y-samples. Black dots indicate sampling with 64 and 256 k_y values in the left and the right columns, respectively. Even with 256 k_y-samples it is impossible to adequately capture the oscillatory behaviour. Some samples fall close to the pole and contribute with a much higher relative amplitude to the

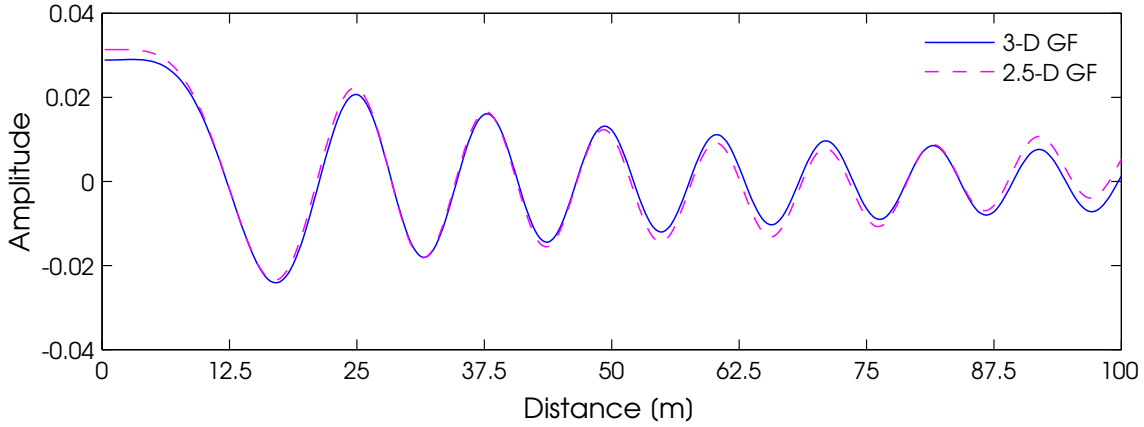

Figure 4.1: *3-D and 2.5-D frequency-domain acoustic fullspace solutions for $f = 150$ Hz along the slice indicated in Fig. 3.1 The true 3-D solution is given by the blue line and the 2.5-D solution obtained from 64 k_y values is drawn in magenta. The 2.5-D solution clearly deviates from the true 3-D solution.*

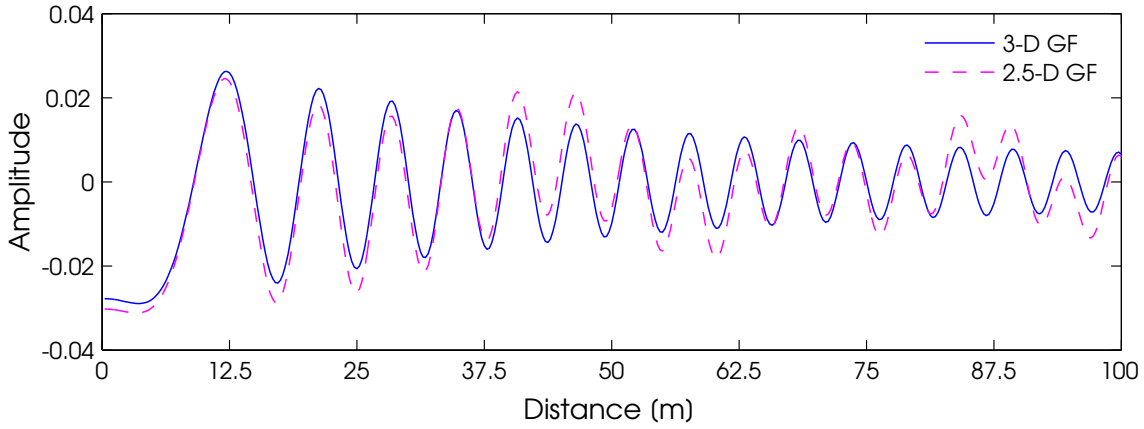

Figure 4.2: *3-D and 2.5-D frequency-domain acoustic fullspace solution along the slice indicated in Fig. 3.1. The true 3-D solution is given by the blue line and the 2.5-D solution obtained from 64 ky values is drawn in magenta. The 2.5-D solution clearly deviates from the true 3-D solution.*

reconstructed frequency-domain solution.

4.1.3 Enhanced wavenumber sampling strategies

Several authors have presented enhanced wavenuber sampling strategies, which aim to mitigate problems associated with critical wavenumbers and to reduce the

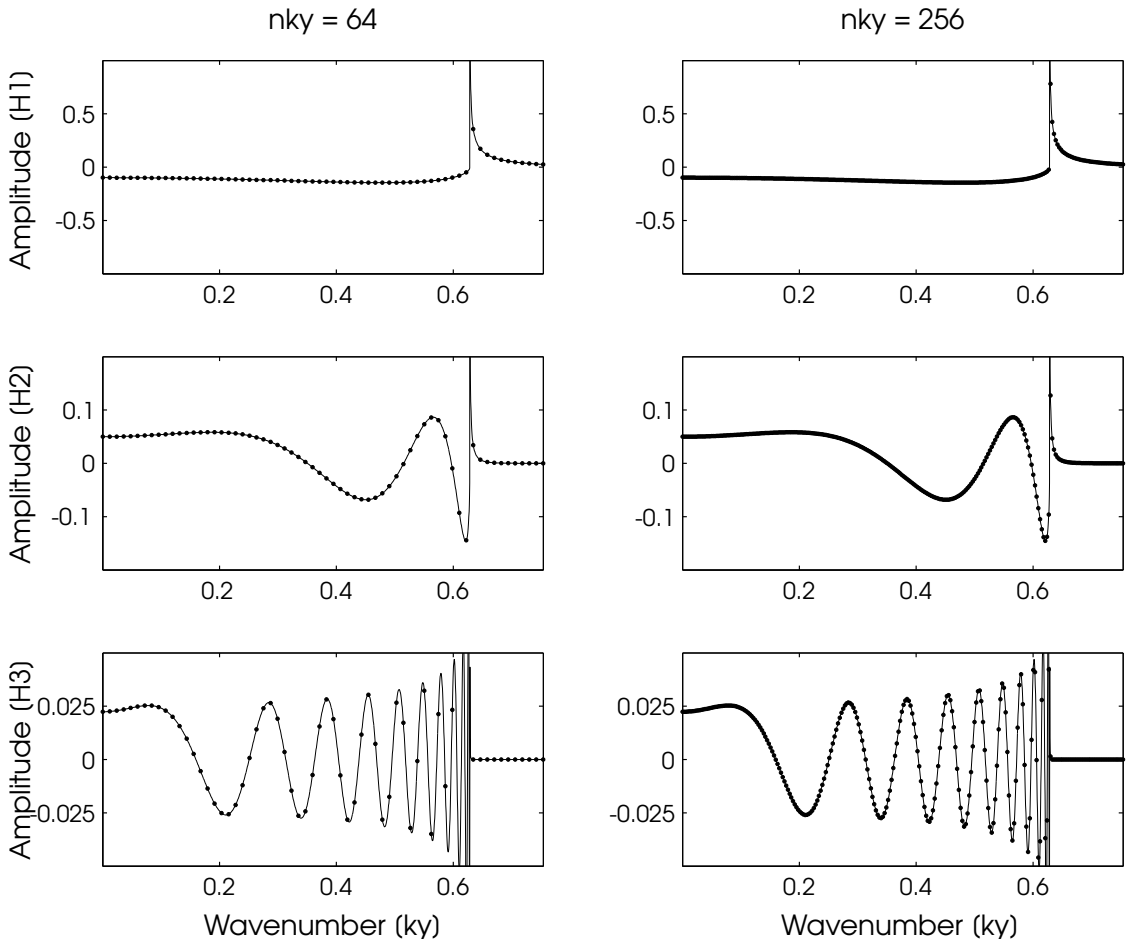

Figure 4.3: *Wavenumber spectra extracted from the 2.5-D fullspace solution in model HAT at receivers H1 (top), H2 (middle) and H3 (bottom) (Fig. 3.1). Only the real parts are shown. Note the increasing degree of oscillation for higher k_y values and the steep behaviour near the critical wavenumber $k_y = 0.6283\ m^{-1}$. Frequency is fixed at 150 Hz. Thin black lines correspond to a dense sampling with 2048 k_y-samples. Black dots correspond to samping with 64 and 256 k_y values. Even with 256 k_y-samples it is impossible to adequately capture the behaviour near the critical wavenumber.*

total number of k_y samples. Zhou and Greenhalgh (2006) presented a Gauss Legendre type sampling scheme, which only considers k_y values up to the critical wavenumber but omits both the singularity and the evanescent field component (which is small in the far-field). Capturing the increasing rate of oscillation with successively denser Legendre spacings, allows the reconstruction of frequency-domain solutions with a relatively low number of samples. While the method

works well when only acoustic wave propagation and relatively simple models are considered, it is not suited for strongly heterogeneous or especially anisotropic media (Sinclair et al., 2011).

Sinclair (2009) describes a strategy based on skipping wavenumbers close to singularities, by identifying proximity to poles using a tolerance measure, but results appeared to be unstable. Latzel (2010) presents a method for simple elastic models which is based on splitting the wavenumber spectrum in several Gauss Legendre intervals, thus avoiding for multiple poles associated with P and S modes. Her sampling strategy yields acceptable errors in homogeneous and nearly homogeneous fullspace and halfspace models, when locations of the critical points are known. However, the method fails in strongly heterogeneous models with a very high number of unknown singular values (Latzel, 2010, p. 137).

Sinclair et al. (2011) suggests that simply taking a very large number of equidistantly spaced wavenumber samples might be the best solution for general heterogeneous elastic or anisotropic media. Similar strategies were also investigated by Latzel (2010), but she recognized that even with a very high sampling density of more than 2000 wavenumbers, problems occured due to failure of PML boundary conditions, which she uses in her FEM code.

Latzel (2010) noticed that sources close to the boundary tended to cause PML's to break down when a significant amount of evanescent energy was present in the vicinity of critical wavenumbers and - at the same time - single wavenumber samples fell very close to one of these singular points. The failure manifested in high-amplitude standing waves in the associated frequency-wavenumber solution which completely dominated the obtained frequency-domain solution.

4.2 The complex frequency method

Several authors have suggested ways to avoid the problems associated with critical wavenumbers by separating the integration path and the singularities. Most ideas are associated with introducing different forms of attenuation in the medium. Latzel (2010) mentions the following alternatives:

1. Using true viscoelastic forward modeling, which most likely removes the singularities, but trades off with increased complexity and computational costs (Latzel, 2010).
2. Making wavenumbers complex by introducing a small imaginary part to the velocities or the elastic moduli of the model, which moves the integration

path away from the singularities on the real k_y axis (Greenhalgh et al., 2009).

3. Moving the singularities away from the real k_y axis by introducing an imaginary part to the frequency, while keeping the wavenumber samples real valued (Cao and Greenhalgh, 1997).

The latter approach is often used to solve similar problems in discrete wavenumber modelling (Phinney, 1965; Mallick and Frazer, 1987; Bouchon, 2003). Frequency-domain modelling with complex frequencies results in exponentially damped time-domain seismic signals. This makes it particularly suitable for real data applications in frequency-domain full waveform inversion, where complex frequency preconditioning is sometimes used as a method to select apertures and constrain the optimization process by iteratively feeding larger time windows into the inversion (Brenders and Pratt, 2006). Another side effect of complex frequencies is an effective suppression of wraparound effects associated with the Fourier transform to time (Mallick and Frazer, 1987).

By introducing an imaginary part ω_i to the angular frequency, $\omega = \omega_r - i\omega_i$, the acoustic 2.5-D wave equation becomes (Cao and Greenhalgh, 1997)

$$\left(\nabla_2^2 + \frac{(\omega_r - i\omega_i)^2}{c^2} - k_{y^2}\right) \hat{\tilde{P}}(x, k_y, z, \omega) = -\bar{S}(\omega)\delta(\mathbf{r} - \mathbf{r_0}) \tag{4.3}$$

where ω_i is the imaginary part $Im[\omega]$ and $\hat{\tilde{P}}$ is the exponentially damped 2.5-D wavefield. For the case of a homogeneous fullspace, Eq. (4.3) can be solved with the complex valued frequency-wavenumber 2.5-D Green's $\hat{\tilde{G}}^{2.5D} = \hat{\tilde{P}}/S(\omega)$ Function which is given by

$$\hat{\tilde{G}}^{2.5D}(k_y, \mathbf{r}, \omega) =$$

$$\begin{cases} -\frac{1}{4}\left[J_0\left(r\sqrt{\left(\frac{\omega_r - i\omega_i}{c}\right)^2 - k_y^2}\right) - iY_0\left(r\sqrt{\left(\frac{\omega_r - i\omega_i}{c}\right)^2 - k_y^2}\right)\right] & , \quad k_y < \frac{\omega_r}{c} \\ \frac{1}{2\pi}K_0\left(r\sqrt{k_y^2 - \left(\frac{\omega_r - i\omega_i}{c}\right)^2}\right) & , \quad k_y > \frac{\omega_r}{c} \end{cases} \tag{4.4}$$

The spectral response for a particular frequency can be obtained by an inverse Fourier transform over k_y, which reduces to a summation of all frequency-wavenumber solutions when the problem is confined to the xz-plane (i.e. $y = 0$ and $exp(ik_y y) = 1$) (Cao and Greenhalgh, 1997)

$$\hat{\tilde{P}}(\mathbf{r},\omega) = \frac{1}{2\pi}\int_{-\infty}^{\infty} \hat{\tilde{P}}(x,k_y,z,\omega)exp(ik_y y)dk_y \tag{4.5}$$

$$\approx \frac{\Delta k_y}{2\pi}\sum_{j=1}^{N_{ky}} \hat{\tilde{P}}(\omega,k_y^j,\mathbf{r}) \tag{4.6}$$

To obtain a time-domain response an additional Fourier transform over frequency has to be performed (Cao and Greenhalgh, 1997)

$$\hat{P}(\mathbf{r},t) = \frac{1}{2\pi}\int_{-\infty}^{+\infty} \hat{\tilde{P}}(\mathbf{r},\omega)exp(i\omega t)d\omega \tag{4.7}$$

Again, the hat denotes that $\hat{P}$ corresponds to a time series which is exponentially damped by the term $exp(-\omega_i t)$. The original (non-damped) time-domain signal can be recovered by multiplying $\hat{P}$ with the inverse exponential function $exp(\omega_i t)$

$$P(\mathbf{r},t) = \hat{P}(\mathbf{r},t)exp(\omega_i t) \tag{4.8}$$

Using this relation, field data can be made comparable to solutions obtained from complex frequency modelling. However, for (4.8) to hold, only one fixed ω_i value is allowed for all frequency components (Latzel, 2010).

Positive effects on the frequency domain solution

Figure 4.4 shows how the imaginary frequency component $\omega_i = 10$ mitigates problems associated with critical points in the wavenumber spectrum. The 3-D solution (light blue) fits the 2.5-D solution (magenta) much better than in Fig. 4.1 in which frequency is pure real ($\omega_i = 0$). Again, a frequency of 150 Hz and 64 k_y samples were used.

Associated wavenumber spectra at receivers H1, H2 and H3 (see Fig. 3.1), indicate that singularities are indeed circumvented to a large extent, which significantly facilitates capturing the overall oscillatory pattern (see Fig. 4.5). Note, that the solution is considerably damped, especially at receiver H3. This can also be seen in the 3-D and the 2.5-D frequency-domain solutions (Fig. 4.4) which exhibit smaller amplitudes than the 3-D solution without complex frequency.

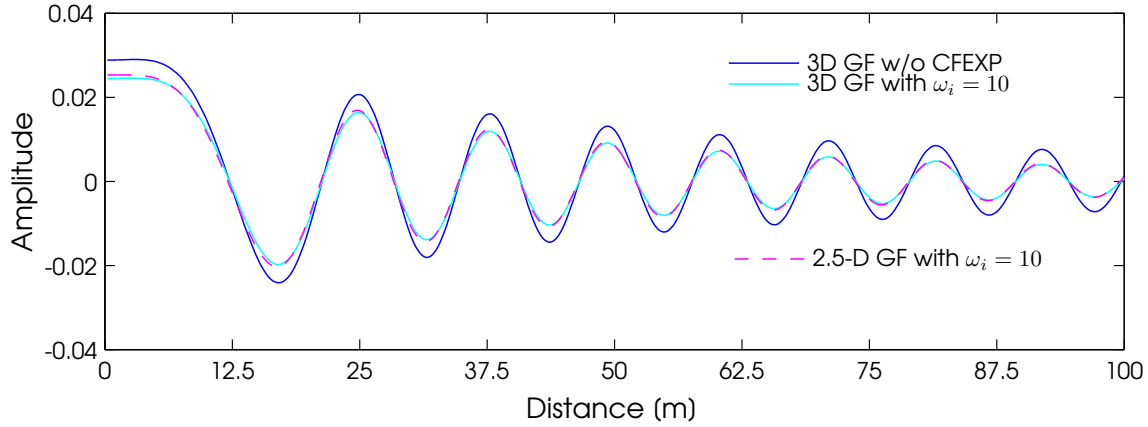

Figure 4.4: *3-D and 2.5-D frequency-domain acoustic fullspace solution along the slice indicated in Fig. 3.1. The true 3-D solution is given by the blue line, and the 2.5-D solution obtained from 64 k_y values with complex frequencies is drawn in magenta. When an imaginary part $\omega_i = 10$ is introduced, the 2.5-D solution and the 3-D solution match each other very well (see Fig. 4.1 for the same slice without complex frequencies)*

4.3 Choice of the imaginary part

Prior to carrying out finite-element modelling on more complex models, it was necessary to determine a reasonable range of values for the imaginary term ω_i. I set up a simple experiment, based on acoustic frequency-domain 3-D and 2.5-D Green's functions (2.6) and (2.11). As in Section 4.1.2 the experimental geometry corresponds to that of model HAT (see Fig. 3.1).

3-D and 2.5-D solutions were computed for various combinations of angular frequency ω, total number of k_y samples n_{k_y} and the imaginary part ω_i of the angular frequency ω. The error between the true 3-D and the 2.5-D solution is determined as the normalized RMS deviation for a vertical slice along the receiver line, depicted in Fig. 3.1. Figure 4.6 illustrates the high degree of instability caused by coincidentally sampling close to a critical wavenumber, or aliasing in the wavenumber spectrum when n_{k_y} is chosen too small.

For $n_{k_y} = 64$ and $n_{k_y} = 128$, the RMS errors exceed 20 %. There is a trend towards higher errors at higher frequencies but the curve behaviour is rather nonlinear and exhibits abrupt jumps. Sometimes there is a sudden decrease of errors for increasing frequency. Note that NRMSD errors in this Chapter cannot be directly compared to the time-domain errors shown in Chapter 3, as they are estimated in a different context.

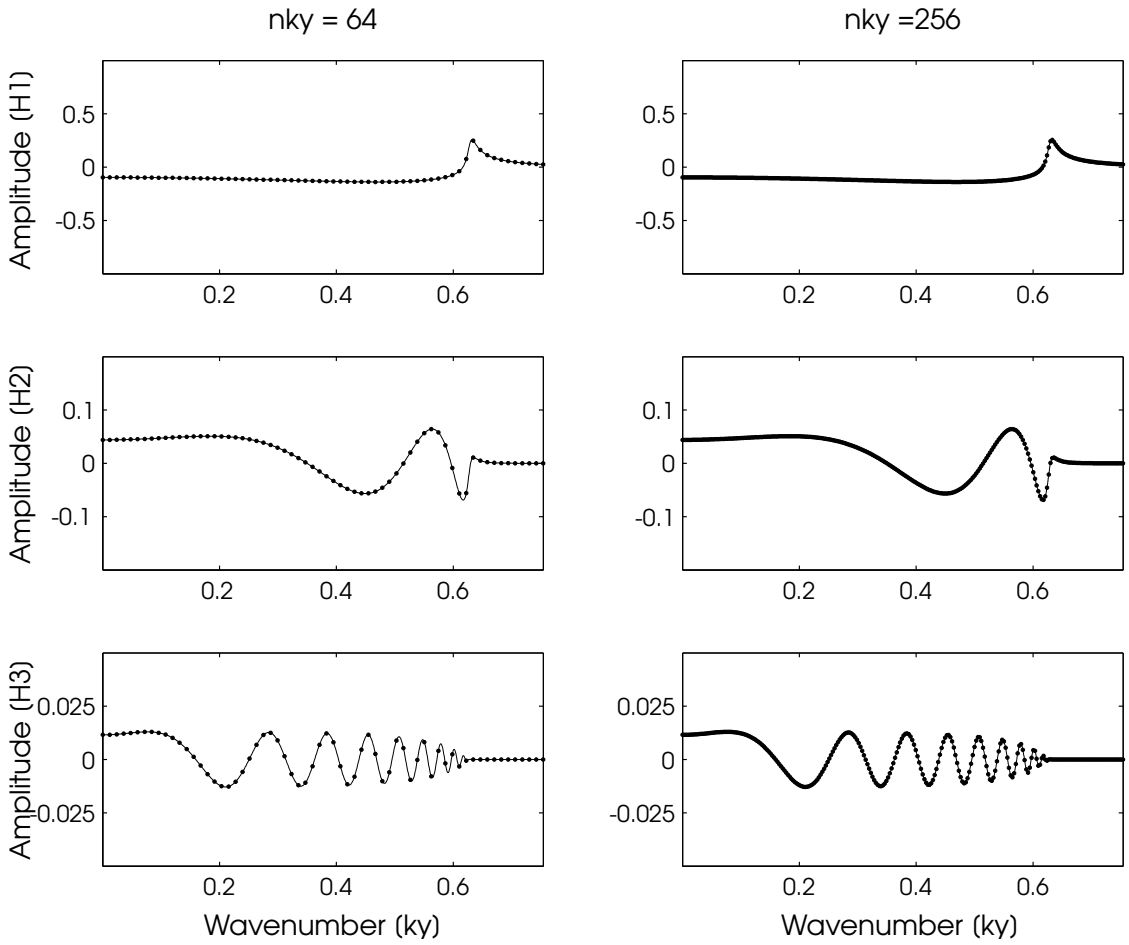

Figure 4.5: *Wavenumber spectra extracted from the 2.5-D fullspace solution with complex a complex frequency ($\omega_i = 10$) in model HAT at receivers H1 (top), H2 (middle) and H3 (bottom) (Fig. 3.1). Frequency is fixed at* 150 *Hz. Singularities are avoided and the overall oscillatory pattern is captured much better than in Fig. 4.3 (for $\omega_i = 0$). The solution is considerably damped at the most distant receiver H3. Only real parts are shown.*

Repeating the experiment with a small imaginary part of $\omega_i = 10$, the errors are significantly reduced (see Fig. 4.7). The choice of $\omega_i = 10$ corresponds to a ratio $R = Im[f]/Re[f]$ of the imaginary part and the real part of the frequency f of ~1/100. Besides exhibiting lower RMS errors, the curves show a much steadier increase with frequency. The sudden fluctuations or jumps which were visible in Fig. 4.6 are completely eliminated. For all further experiments I fixed n_{k_y} at a value of 256, which I considered as a fair compromise between acceptable RMS errors and yet low computational effort.

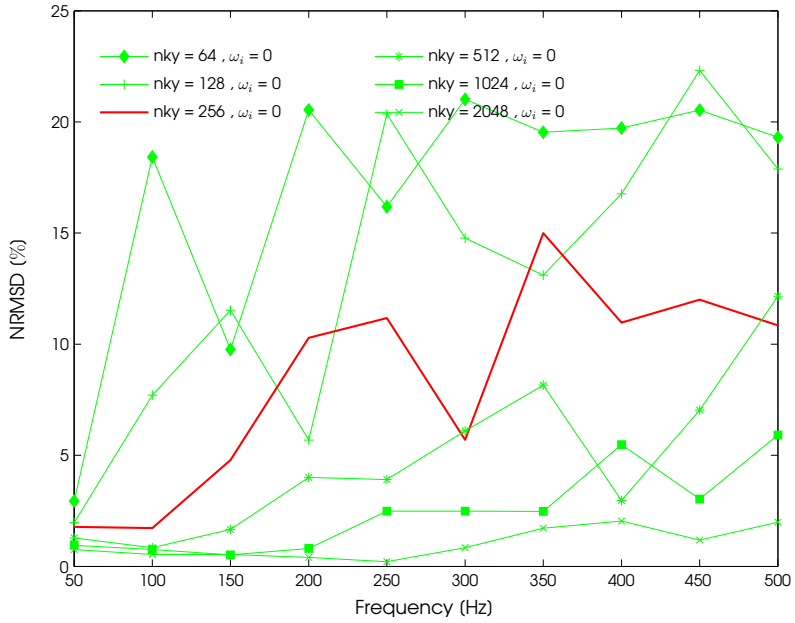

Figure 4.6: *RMS errors for a vertical slice along the receiver line in model HAT (Fig. 3.1). Error curves indicate a high degree of instability due to coincidentally sampling close to a critical wavenumber and/or aliasing in the wavenumber spectrum when n_{k_y} is chosen too small. Although there is a trend towards higher errors for higher frequencies, the error curves behave rather non-linearly and exhibit sudden jumps.*

Finally, I investigated how the magnitude of the imaginary part ω_i affects NRMSD errors by successively increasing ω_i from 0.1 to 200, whilst keeping n_{k_y} fixed at a value of 256. All curves exhibit two local maxima at 250 and 350 Hz, which indicates that samples close to a singularity were picked (Fig. 4.8). Increasing ω_i leads to a smoothing of the curve shape and an overall reduction of NRMSD errors. For choices of ω_i that were larger than 50, the errors tended to increase again (not shown). This is most likely caused by an increasing numerical inaccuracy when damping is too strong and solutions are very close to zero. I fixed ω_i at a value of 10 for all further experiments.

The degree of damping or "removal" of singularities is illustrated in Fig. 4.9, in which the analytical complex-frequency 2.5-D solution (4.4) is shown for a fixed distance of 100 m, a frequency of 150 Hz and many choices of the imaginary component ω_i. An imaginary part of $\omega_i = 10$ is indicated by the dashed line.

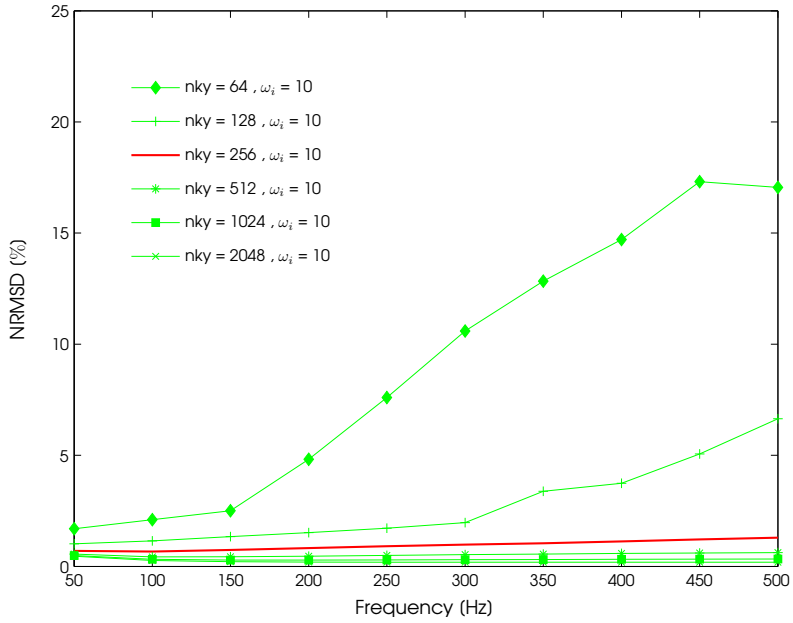

Figure 4.7: *RMS errors obtained from repeating the experiment described in Section 4.1.2 with complex frequency ($\omega_i = 10$) and various values of n_{k_y}. Errors are significantly reduced for all choices of n_{k_y}. The error curves show a much steadier increase with frequency. The sudden fluctuations or jumps that were visible in Fig. 4.6 are completely eliminated.*

4.4 Finite-element 2.5-D modelling with complex frequencies

In this Section I present several forward modelling results, obtained with a complex-frequency version of an acoustic frequency-domain 2.5-D finite element solver. It is investigated, if the complex frequency method mitigates instabilities caused by singular points in the wavenumber spectrum, and yields approximate 3-D results of sufficient accuracy. I decided to perform complex-frequency 2.5-D modeling for a range of frequencies. This allowed me to reconstruct time-domain traces by Fourier inversion and to directly compare 2.5-D modelling to asymptotic 3D-to-2D filtering.

I tried to stay close to experiments performed by Latzel (2010, Section 4.4), directed towards the undesirable consequences of singularities in the k_y-spectrum, in which she uses equidistant wavenumber sampling. In her experiments, Latzel (2010) used a fixed signal frequency of 150 Hz. Hence, I decided to define 150 Hz as my upper limit and performed forward modelling on 30 frequencies between 5

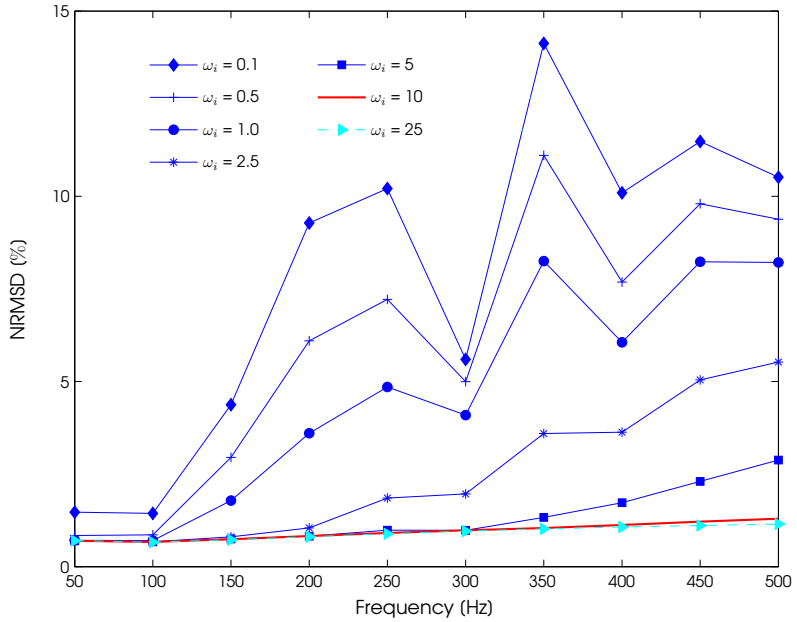

Figure 4.8: *RMS errors obtained from repeating the experiment shown in Figs. 4.6 and 4.7 with a fixed n_{k_y} of 256 and various values of the imaginary component ω_i. For low values of ω_i between 0.1 and 1, error curves show several local maxima which are most likely associated with sampling close to a singularity. For larger values of ω_i the peaks are removed and the overall curve shape seems to be much more controlled.*

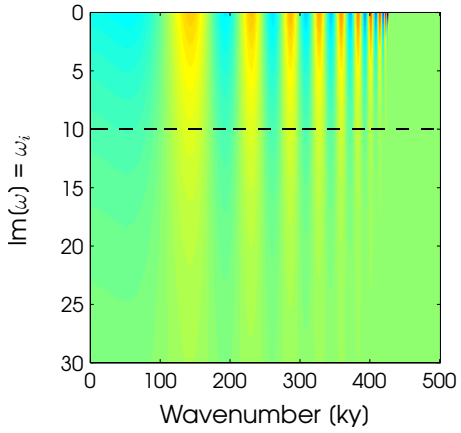

Figure 4.9: *Color-coded image, illustrating how complex frequencies move singularities away from the integration path. The analytical complex-frequency 2.5-D solution (4.4) has been evaluated for a fixed distance of 100 m, a frequency of 150 Hz and many choices of the imaginary component ω_i. The wavenumber spectrum associated with an imaginary part of $\omega_i = 10$ is indicated by the dashed line.*

and 150 Hz ($df = 5\ Hz$). Modelling for higher frequencies was not possible due to limited time and computational resources. The 5 Hz component exhibited numerical artifacts which were manifesting as unrealistically large amplitudes at single receivers. Hence, I didn't include the 5 Hz component in reconstructing the time domain signal. Most likely, the artifacts are caused by a failure of PML boundary conditions, as wavelengths corresponding to 5 Hz exceeded the minimal source-receiver separation.

I considered three transmission-type models (HAT, SAT and BAT; see Sections 3.2.2, 3.2.5 and 3.2.6) approximately twice the size of Latzel's models (she used dimensions of $30 \times 50\ m$). In all examples shown below, grid spacing is 0.5 m and the active modelling domain is enclosed by a frame of 15 m tick PML-type absorbing boundaries. 2.5-D and complex frequency parameterization is based on the results of Section 4.3. The imaginary part ω_i was fixed at 10 and n_{k_y} was set to 256.

Frequency-domain modelling results for the Green's functions were multiplied with the spectrum of a 50 Hz central frequency Ricker wavelet. To obtain a non-attenuated time series, an inverse Fourier transform and a multiplication with $exp(\omega_i t)$ were performed. For better insight into the nature of the k_y spectra near critical wavenumbers and the overall shape of the spectra, complementary 2.5-D modelling (with and without complex frequencies) for a single frequency of 150 Hz and a reference sampling density of $n_{k_y} = 2048$, was performed.

Similar to Section 4.1.2, wavenumber spectra were extracted at three receiver locations, 5, 20 and 100 m away from the source. Again, thin black lines correspond to the reference sampling density of 2048 k_y and black dots represent sampling with 256 k_y samples.

4.4.1 Numerical example: Model HAT

To ensure comparability of numerical and analytical experiments, I tried to reproduce my analytical results with the finite element method, by performing FEM 2.5-D modeling with and without complex frequencies, on the homogeneous acoustic fullspace model HAT. Analytic and FEM wavenumber spectra matched each other very well in the far field (H3), but showed some deviations close to the source (Receivers H1, H2), which can be seen in Fig. 2 in Appendix A. It appears that the pole in the finite element solution (red) is limited in magnitude. Sinclair (2009, Section 8.10) found similar discrepancies at near distances, in SEM 2.5-D modelling. She suspects, that this is because in FEM or SEM, solutions of the *weak* form of the

governing equation are approximated.

In Fig. 4.13, the sample trace 30 at a depth of 74 *m* is displayed in the time and the frequency domain. Traces obtained from finite-element complex-frequency 2.5-D modelling (magenta) and 3-D finite-difference results (blue) fit each other very well **(a)**. In the right column **(b)**, a trace-by-trace comparison of 2-D (red) and filtered 3-D (green) data is shown. Asymptotic filtering shows typical failures at low frequencies. Maximum trace amplitudes fit much better in the case of 2.5-D modelling.

4.4.2 Numerical example: Model SAT

As a second example I considered the more complicated stochastic model SAT (Section 3.2.5). In Fig. 4.12, the wavenumber spectra obtained from 2.5-D modelling, without **(a)** and with **(b)** an imaginary frequency, are juxtaposed. Spectra are output at receivers S1, S2 and S3 (see Fig. 3.12) and only real parts are shown. When frequency is made complex, the small irregularities along the spectrum are smoothed out to a large extent and singularities are almost completely removed.

In Fig. 4.13, the sample trace 30 at a depth of 74 *m* is displayed in the time and the frequency domains. Traces obtained from finite-element complex frequency 2.5-D modelling (magenta) and 3-D finite-difference results (blue) fit each other very well **(a)**. In the right column **(b)**, a trace comparison of 2-D (red) and filtered 3-D (green) data is shown. Asymptotic filtering does a very good job in stochastic media and comes very close to complex frequency 2.5-D modelling, in terms of NRMSD errors.

4.4.3 Numerical example: Model BAT

Finally, the high contrast block model BAT was tested (Section 3.2.6). Figure 4.15 shows the wavenumber spectra obtained from 2.5-D modelling, without **(a)** and with **(b)** using complex frequencies. Spectra are shown for receivers S1, S2 and S3 (see Fig. 3.12) and only real parts are displayed. Again, most of the tiny fluctuations, visible in the wavenumber spectrum without complex frequencies, are eliminated.

Both complex frequency 2.5-D modelling and asymptotic filtering exhibit the largest errors at receivers located behind the low-velocity zone (see Fig. 3.14).

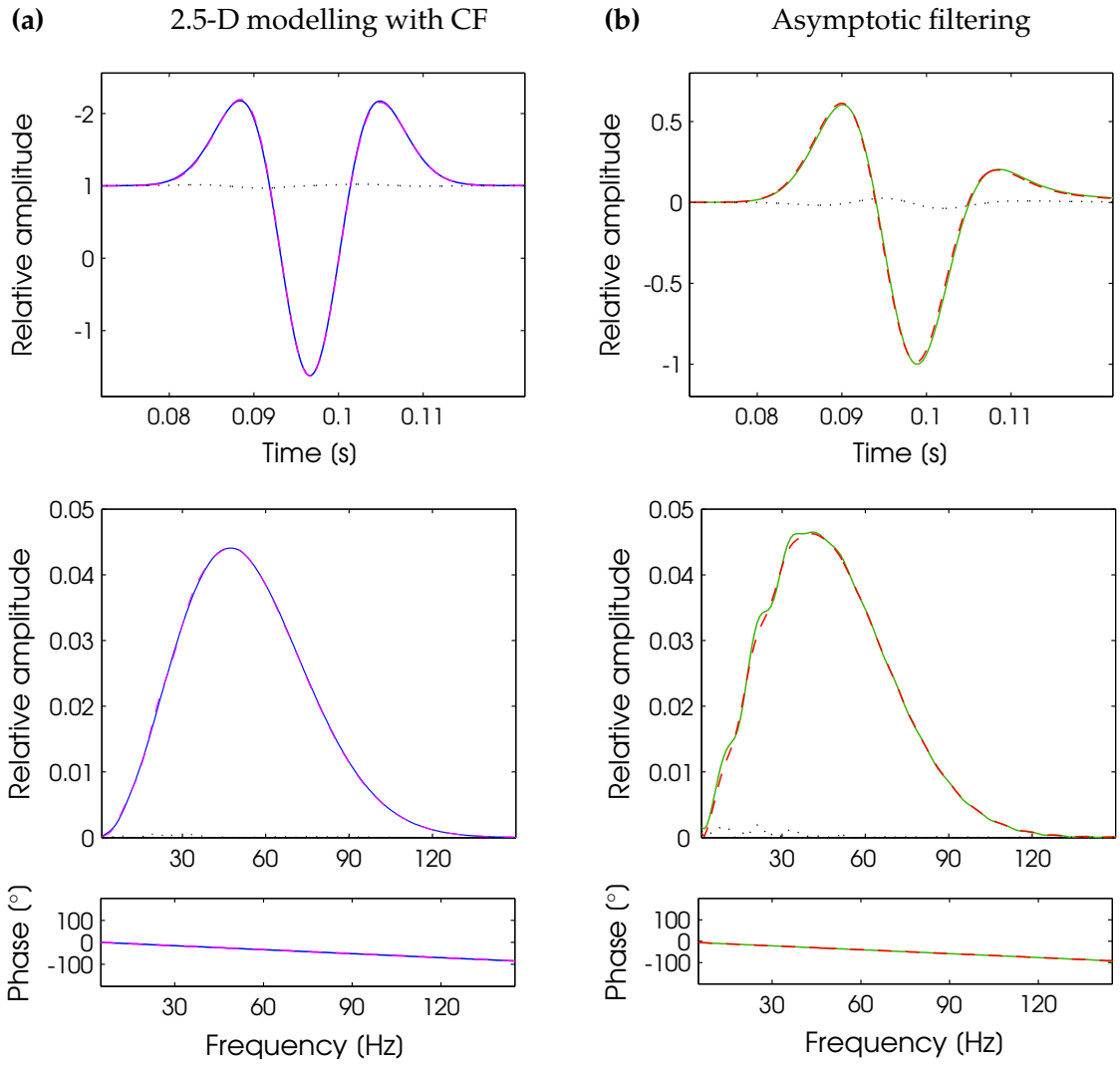

Figure 4.10: *Model HAT; Sample trace* 30 *at depth of* 74 *m displayed in time and the frequency domains. Central frequency is* 50 *Hz.* ***(a)*** *FEM complex-frequency 2.5-D modelling (magenta) and FDM 3-D modeling (blue). 2.5-D modeling results were multiplied with* $exp(\omega_i t)$. ***(b)*** *Asymptotic filtering results for comparison. FDM 2-D data (red) and filtered FDM 3-D data (green).*

2.5-D modelling yields smaller errors, better matching of maximum trace amplitudes and slightly out-performs asymptotic filtering - even though filtering worked quite well in this acoustic example.

The misfits in the time and the frequency domains (Fig. 4.16) are slightly larger for asymptotic 3D-to-2D conversion. In 2.5-D modelling, the major discrep-

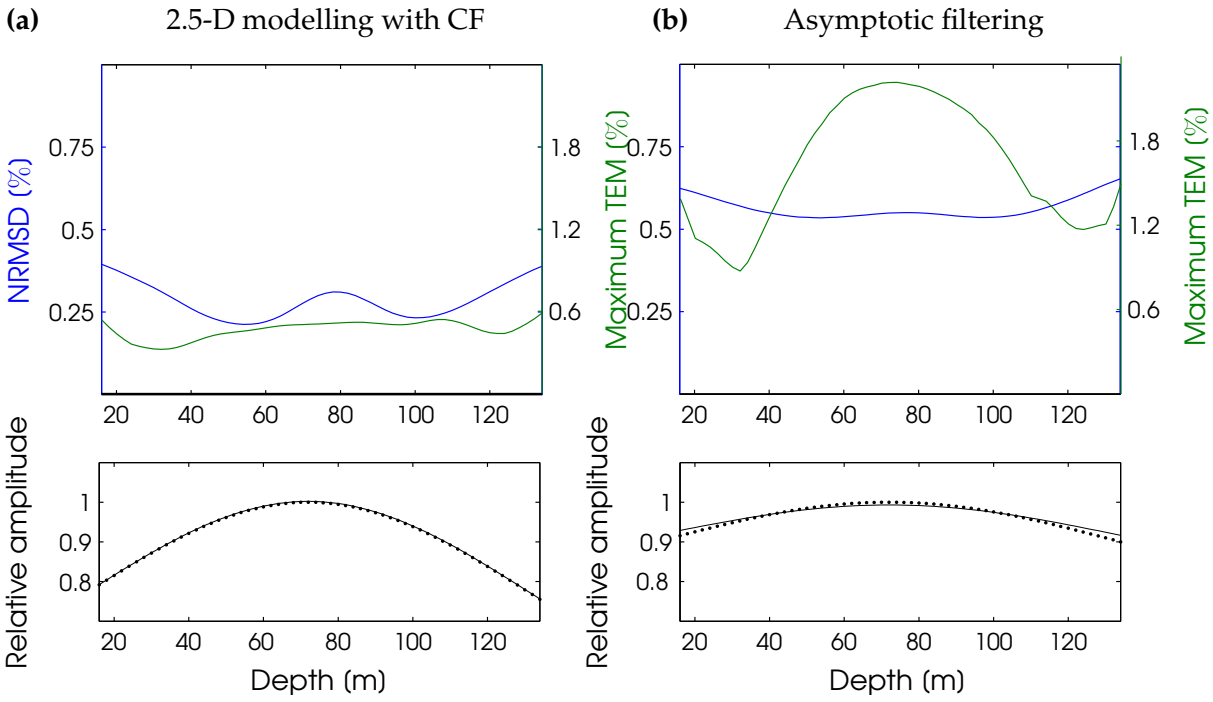

Figure 4.11: *Model HAT:* ***(a)*** *Maximum TEM (green) and NRMSD (blue) between 3-D and 2.5-D (top row). Maximum trace amplitudes of FDM 3-D (dashed) and FEM 2.5-D (dotted) data (bottom row).* ***(b)*** *Analogous results obtained by comparing FDM 2-D and asymptotically filtered FDM 3-D data.*

ancies seem to rather occur at intermediate frequencies whereas in asymptotic filtering, the errors are slightly larger at lower frequencies.

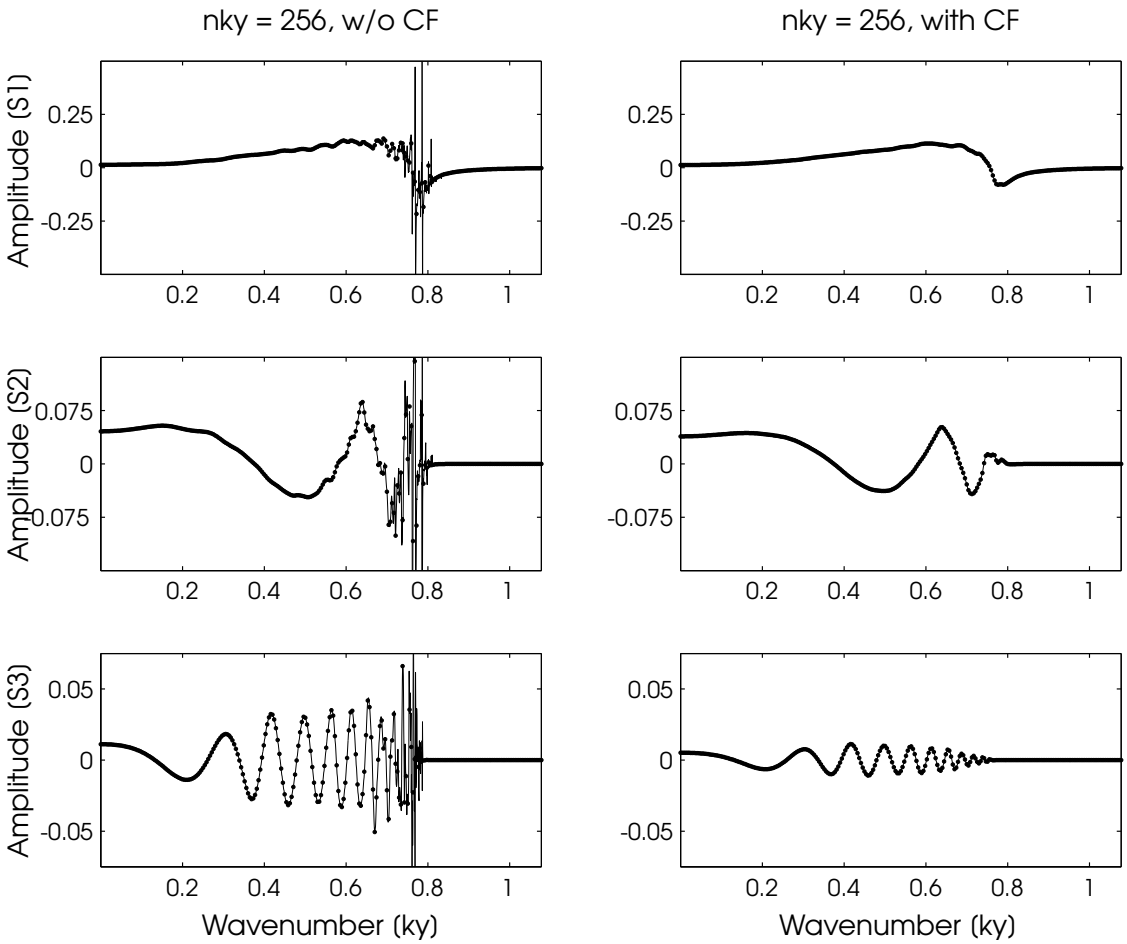

Figure 4.12: *Model SAT; Wavenumber spectra obtained from 2.5-D modelling without (left column) and with (right column) a complex valued frequency at receivers S1, S2 and S3 (see Fig. 3.12). Frequency f is* 150 *Hz and ω_i is* 0 *and* 10 *in the left and the right column, respectively. Only the real part of the spectrum is shown. Thin black lines: Reference sampling density with 2048 k_y samples. Black dots: Sampling with 256 k_y samples. Singularities near $k_y = 0.8$ are completely removed when frequency is made complex.*

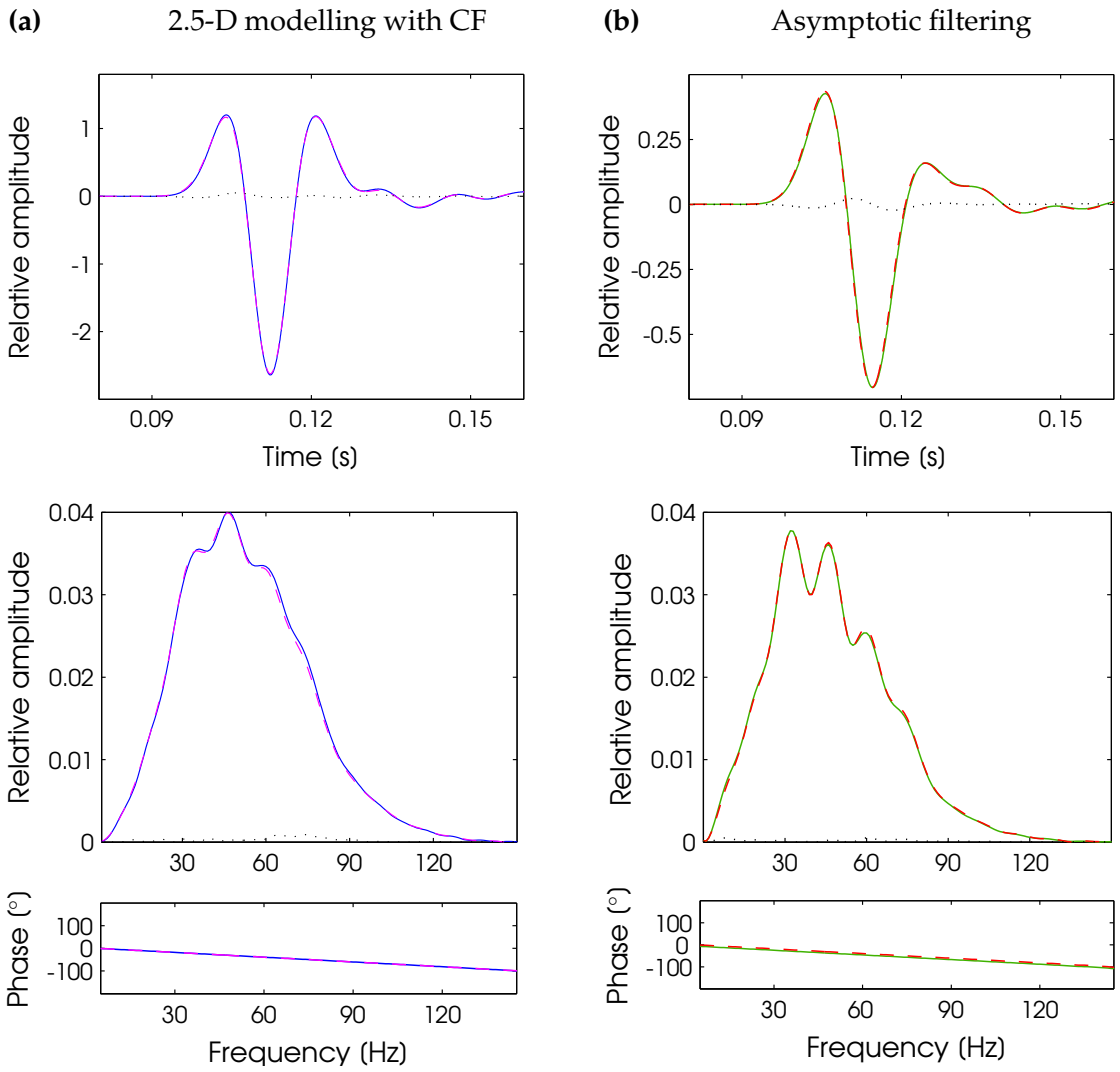

Figure 4.13: *Model SAT; Sample trace* 30 *at a depth of* 74 *m displayed in the time and the frequency domains. Central frequency is* 50 *Hz.* ***(a)*** *FEM complex frequency 2.5-D modelling (magenta) and FDM 3-D modelling (blue). 2.5-D modelling results were multiplied with* $exp(\omega_i t)$. ***(b)*** *Asymptotic filtering results for comparison. FDM 2-D data (red) and filtered FDM 3-D data (green).*

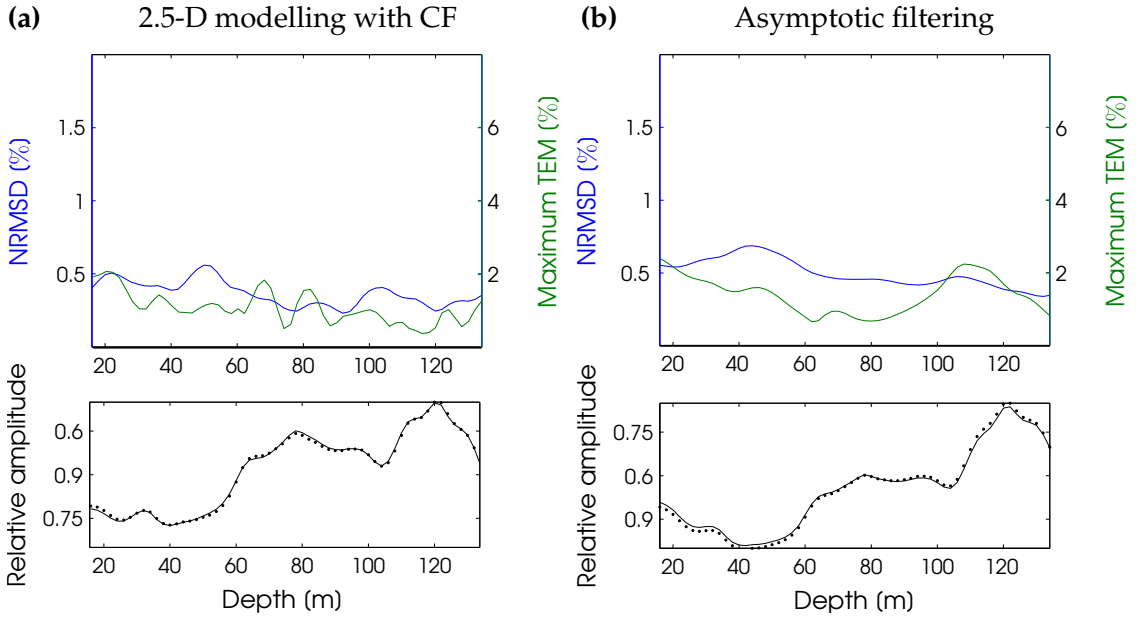

Figure 4.14: *Model SAT;* ***(a)*** *Maximum TEM (green) and NRMSD (blue) between 3-D and 2.5-D (top row). Maximum trace amplitudes of FDM 3-D (dashed) and FEM 2.5-D (dotted) data (bottom row).* ***(b)*** *Analogous results obtained by comparing FDM 2-D and asymptotically filtered FDM 3-D data.*

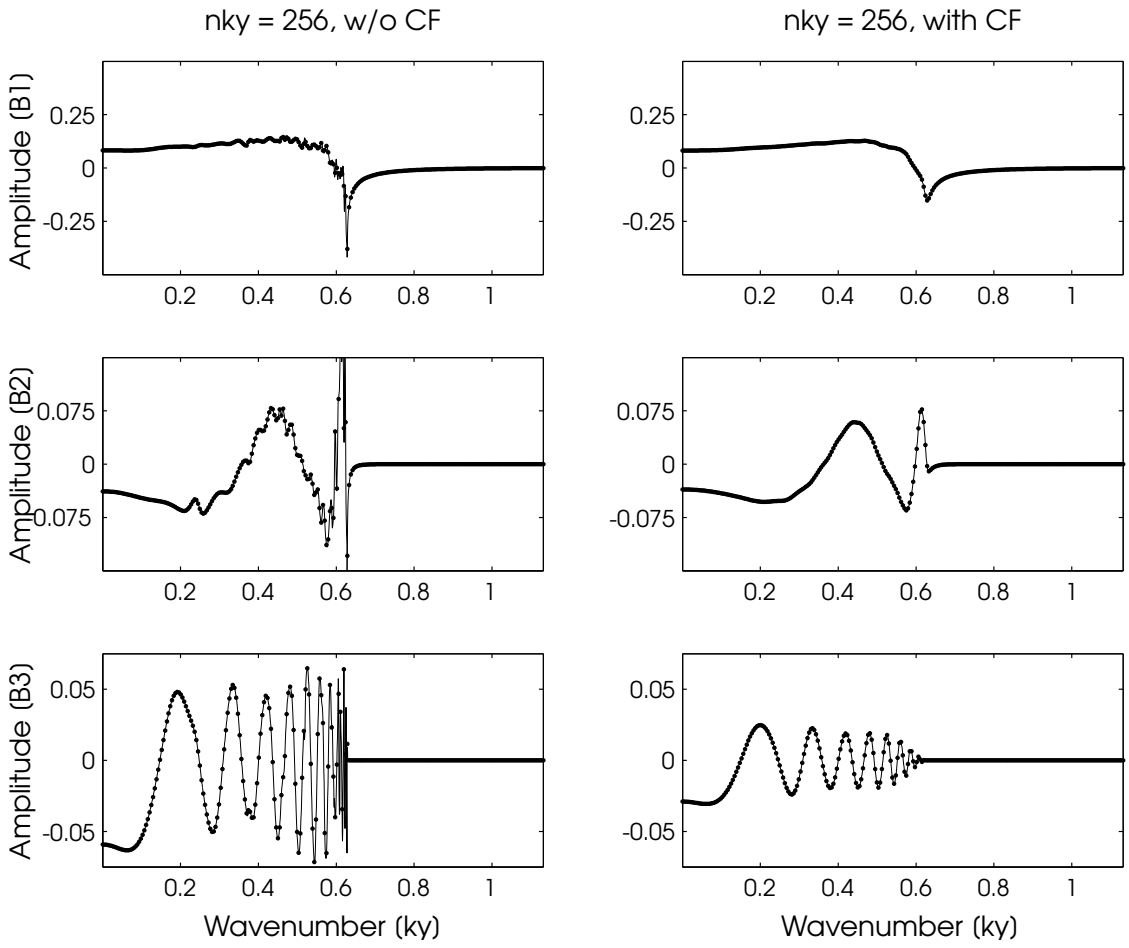

Figure 4.15: *Model BAT; Wavenumber spectra obtained from 2.5-D modelling without (left column) and with (right column) complex valued frequencies at receivers B1, B2 and B3 (see Fig. 3.14). Frequency f is* $150Hz$ *and* ω_i *is* 0 *and* 10 *in the left and the right column, respectively. Only the real part of the spectrum is shown. Thin black lines: Reference sampling density of 2048 k_y. Black dots: Sampling with 256 k_y samples. Complex frequencies significantly smooth out the singularity near $k_y = 0.6$.*

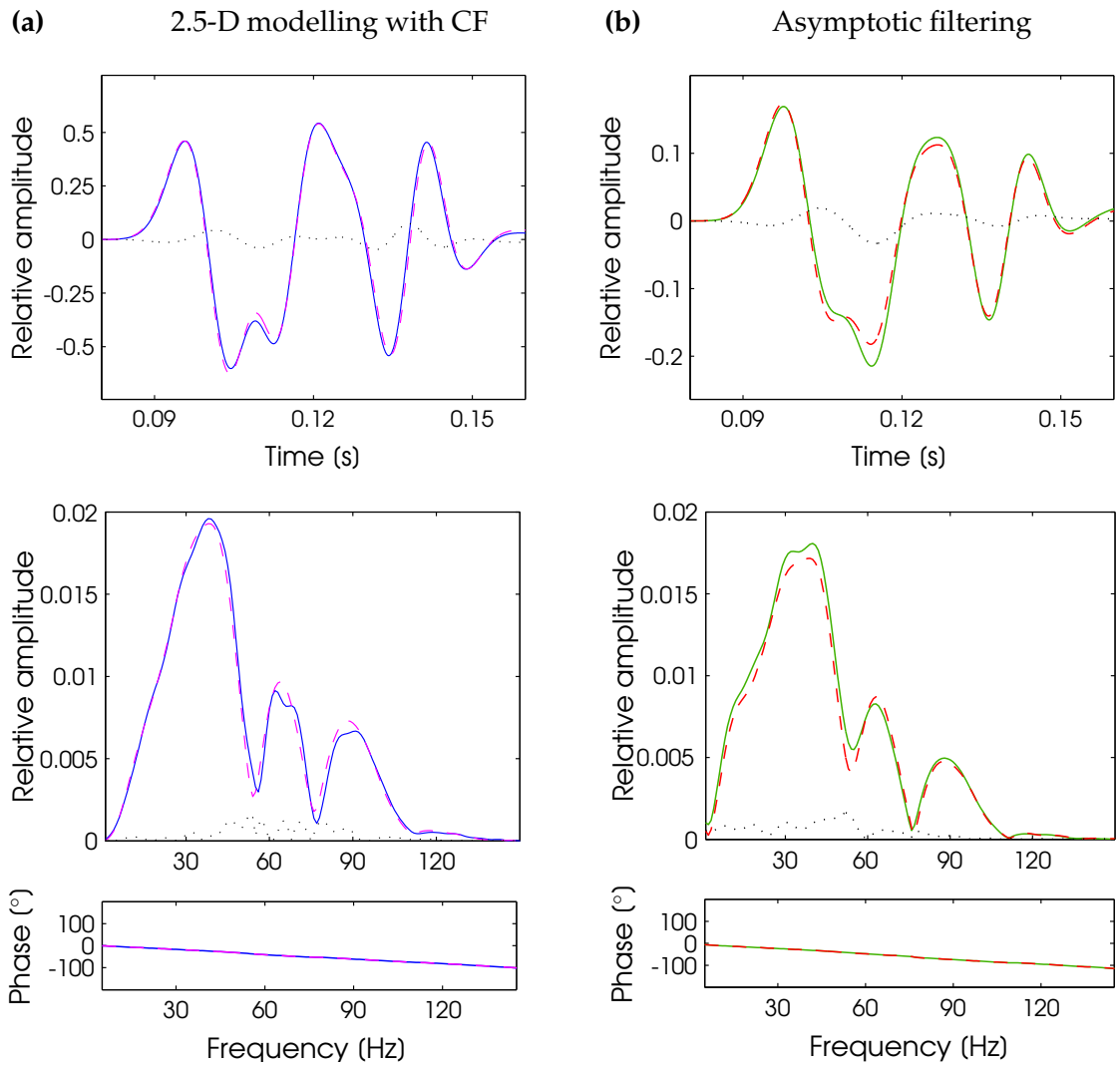

Figure 4.16: *Model BAT; Sample trace* 45 *in a depth of* 104 *m displayed in the time and the frequency domains. Central frequency is* 50 *Hz.* ***(a)*** *FEM complex frequency 2.5-D modelling (magenta) and FDM 3-D modelling (blue). 2.5-D modelling results were multiplied with* $exp(\omega_i t)$. ***(b)*** *Asymptotic filtering results for comparison. FDM 2-D data (red) and filtered FDM 3-D data (green).*

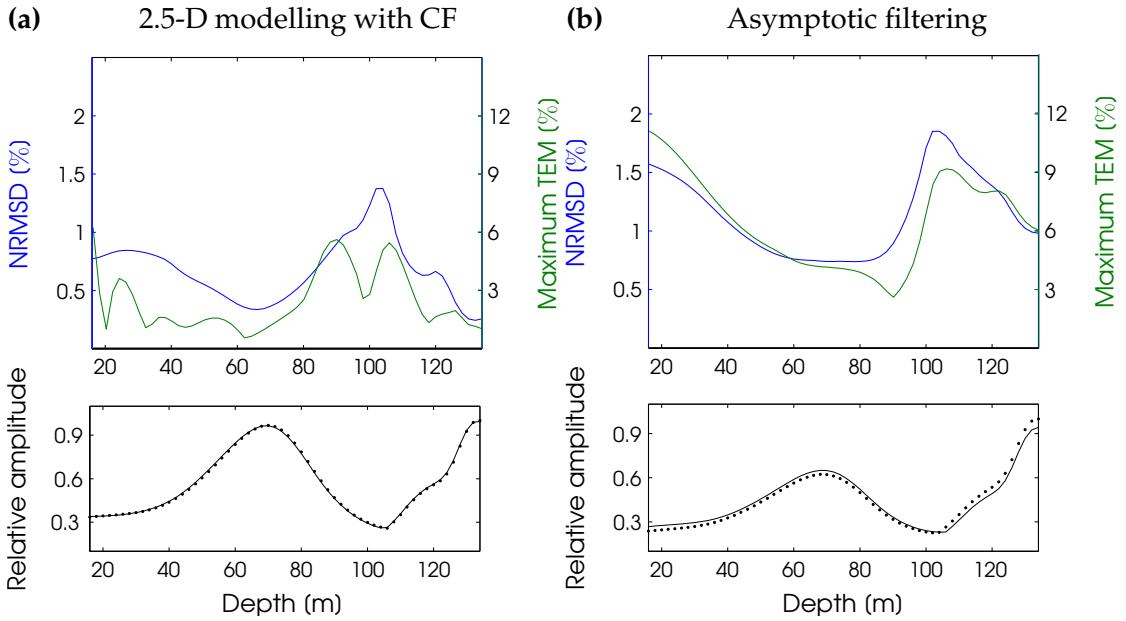

Figure 4.17: *Model BAT;* ***(a)*** *Maximum TEM (green) and NRMSD (blue) between 3-D and 2.5-D (top row). Maximum trace amplitudes of FDM 3-D (dashed) and FEM 2.5-D (dotted) data (bottom row).* ***(b)*** *Analogous results obtained by comparing FDM 2-D and asymptotically filtered FDM 3-D data.*

Chapter 5

Conclusions and Outlook

My contributions

A critical evaluation of 3D-to-2D transformation using asymptotic filters has been performed by propagating 2-D and 3-D wavefield through purely two-dimensional models, applying the correction, and comparing 2-D to filtered 3-D synthetic seismograms in the time and the frequency domains. Average NRMSD errors generally stay below an acceptable value around 1 % for purely acoustic media like a homogeneous fullspace (HAT) or a stochastic fullspace (SAT). A full waveform inversion was performed only on a single, very simple, constant-density acoustic model, including block anomalies and exhibiting only minor evidences of interfering events. The inversion results shown in Section 3.3 exhibited only marginal disparities between model reconstructions from full waveform inversion of 2-D and filtered 3-D data.

However, when full elastic treatment is considered, elastic mode conversions and energy leakage into different elastic modes occurs, which highly complicates the wavefield and causes severe interference between P and S waves. This results in considerably increased NRMSD error values of up to 5 % and maximum TEM errors up to 40 % for models like the high contrast block model (BET) and an 50 Hz central frequency x-directed source. It is most likely that adverse effects in inversion are much stronger when full elastic treatment is considered

Trace-by-trace comparison of 2-D and filtered 3-D data often indicated higher discrepancies at low frequencies, while at higher frequencies, amplitudes tended to match each other much better. In my opinion, this does not only reflect the inherent asymptotic assumption in 3-D to 2-D conversion, but also the fact that lower frequency components diffract around obstacles more easily and deviate

stronger from direct ray paths, thus violating the straight-ray assumption more severly.

The fact that I often observed relatively small errors at higher frequencies raises the hope that frequency-domain optimization schemes, which start at low frequencies and progressively include higher frequencies, might potentially be able to repair damages caused by faulty 3D-to-2D transformation, in later iterations, and ultimately yield model reconstructions of comparable quality - even in the case of elastic treatment. On the other hand, large errors at low frequencies might exacerbate difficulties related to entrapment in local minima.

I regard my results as an indication that 3D-to-2D transformation is acceptable, as long as velocity contrasts are moderate, and only slight shear energy is contained in the data. This might be the case in marine or some cross-well applications. Filtering works particularly satisfactory in acoustic stochastic media. However, in fully elastic, high contrast, heterogeneous media, the filter fails completely. Hence, I strongly advise to avoid the application of asymptotic 3D-to-2D conversion when the medium under investigation comprises large velocity contrasts, and/or a strong shear component is present.

Several analytical experiments and numerical examples on frequency-domain 2.5-D modelling with complex frequencies, were presented. Preliminary results suggested, that relatively large values of the imaginary frequency component ω_i are required to achieve a noticeable reduction of NRMSD errors. High magnitudes of ω_i - in turn - result in strong damping towards later times and a removal of subtle disruptions in the wavenumber spectrum. This raises the concern of a loss in signal quality.

I regard the excellent time- and frequency-domain fit of 3-D FDM and reconstructed 2.5-D (complex frequency) FEM time-domain signals as an indication that complex frequencies do not markedly deteriorate wavefield information in the data. Even though the damping parameter ω_i has to be chosen relatively high, it seems that neither significant distortion of the waveform nor major loss of signal information occurs. The analytical inverse relation - given by a time-domain multiplication with $exp(t\omega_i)$ - seems to be fully satisfied. Compared to elastic experiments on equidistant wavenumber sampling, performed by Latzel (2010), the number of wavenumber samples required for stable behaviour could be reduced by a factor of 10.

Suggestions for further research

Future research could be directed towards various aspects which I was not able to address during the course of this thesis. First of all, it would be important to extend the suite of 3D-to-2D test cases to more realistic, elastic reflection-type models such as the *MARMOUSI2* benchmark model (Martin et al., 2006) or even wide-azimuth scenarios). In addition, it would be worthwhile to extend the inversion part of this thesis to the elastic case.

My investigations on complex-frequency FEM 2.5-D modelling were performed in the acoustic approximation and can therefore only be considered as a proof of concept. I did not proceed to the much more challenging elastic or anisotropic cases. The results of Marelli et al. (2011) give strong evidence that elastic treatment is inevitable for waveform inversion on cross-borehole experiments in high-contrast media. Therefore, it would be important to establish a true elastic complex frequency 2.5-D modelling code, so as to achieve critical usefulness. It should be straight-forward to extend the complex frequency acoustic method to the elastic case.

To date, 2.5-D modelling with complex frequencies has only been tested with sources and receivers that are confined to the xz-plane. It would be important to incorporate a suitable numerical integration method for carrying out the inverse Fourier transform to the frequency domain, when other source-receiver geometries are desired. With the availability of a stable elastic complex-frequency 2.5-D forward solver, one could extend the work further by, for example, investigating which degree of model variation in the third direction is allowed in 2.5-D modelling.

The total number of wavenumbers has to be reduced further. Taking into account the starting model and the source-receiver layout, could help in this regard. Naturally, the final step would be to combine the 2.5-D complex frequency forward solver with a full waveform inversion scheme and to invert field data.

Appendix A: Verification of numerical algorithms

Here I present supporting results, obtained from comparing analytical to finite-element and finite-difference solutions. This was done in order to verify comparability of the different approaches to wavefield modelling which were used within this thesis.

Verification of 3-D and 2-D FDM numerical code

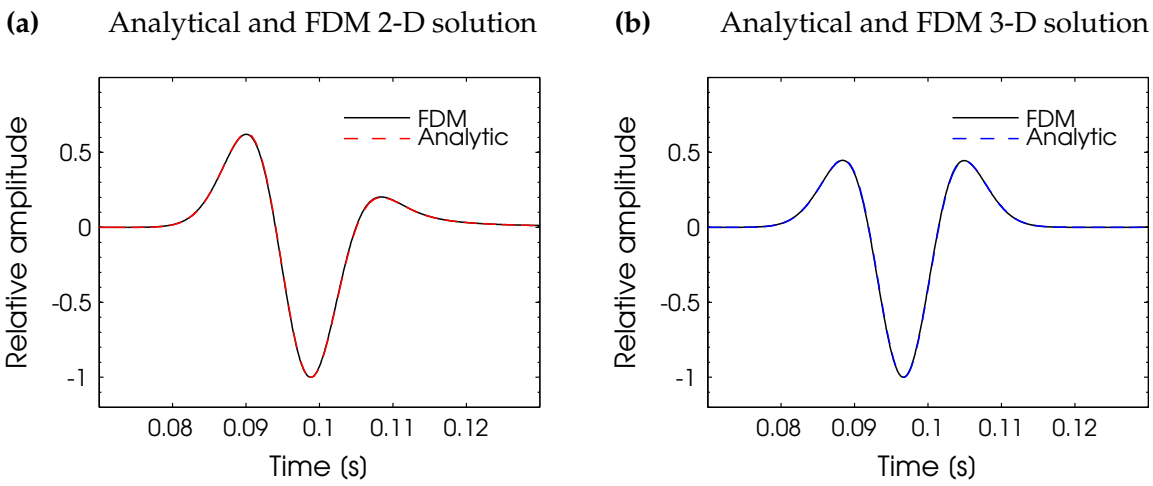

Figure 1: *Verification of the employed finite difference code. Analytical modelling is based on convolving acoustic 2D and 3D Green's function solutions for a constant velocity medium with a Ricker-type source wavelet. FDM modelling has been performed in a homogeneous medium with the same wavespeed and source-receiver distance. Analytical time-domain signals (black) compare very well to their FDM counterparts (red and blue).*

Verification of complex-frequency 2.5-D FEM numerical code

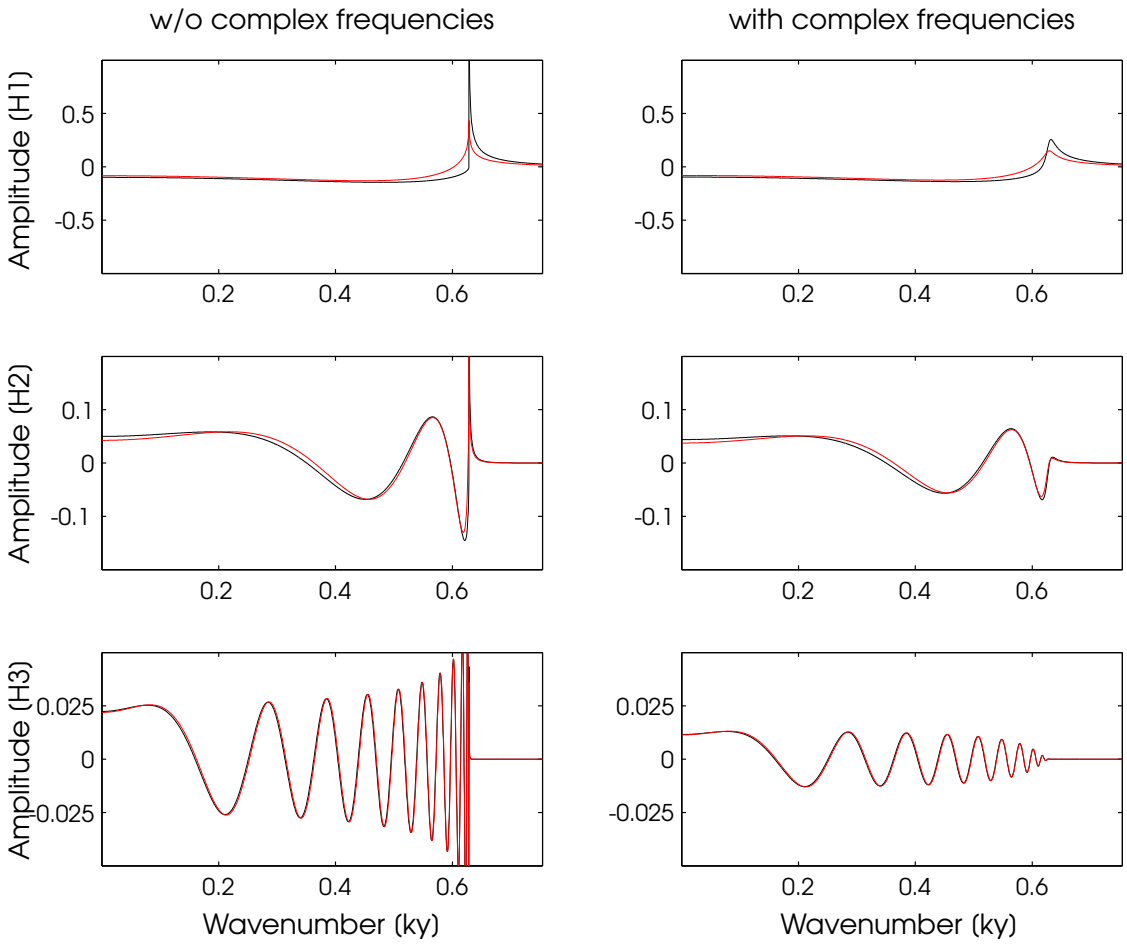

Figure 2: *Verification of employed 2.5-D finite element code, with (right column) and without (left column) complex frequencies. Analytical modelling is performed on basis of the 2.5-D Green's function solution 4.4 for a homogeneous acoustic fullspace. Wavenumber spectra, output at receivers H1, H2 and H3 (5, 10 and 20 m away from the source, show a good agreement, but the fit deteriorates near to the source.*

Appendix B: Trace-by-trace errors corresponding to Chapter 2

This addendum contains a compilation of trace-by-trace NRMSD, maximum TEM errors and maximum trace amplitudes, which were not explicitly described in the main text. See Section 3.2.1 for a description of the underlying numerical experiments and details on the error estimation.

Model LAR - NRMSD, maximum TEM errors and maximum trace amplitudes

(a) Maximum trace amplitudes

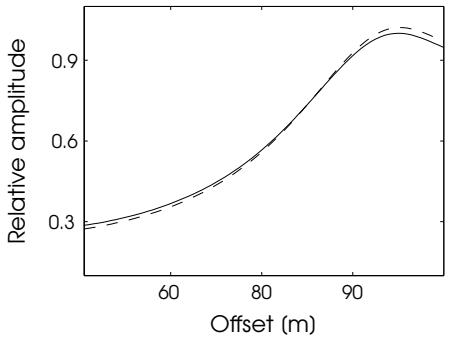

(b) RMS and maximum errors

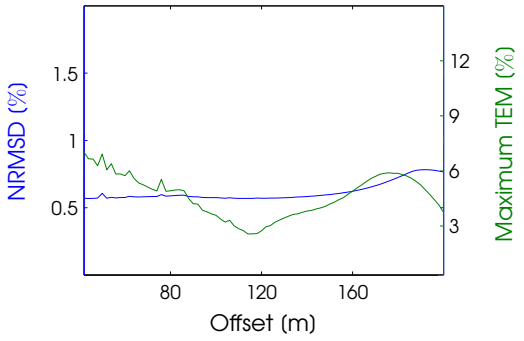

Figure 3: *Model LAR.* ***(a)*** *Maximum trace amplitudes of 2-D (dashed) and filtered 3-D (solid) data. There is over-correction at near offsets and under-correction at far offsets.* ***(b)*** *NRMSD and maximum TEM in %. Errors are low, but slightly higher than in model HAT and SAT.*

Model SAT - NRMSD, maximum TEM errors and maximum trace amplitudes

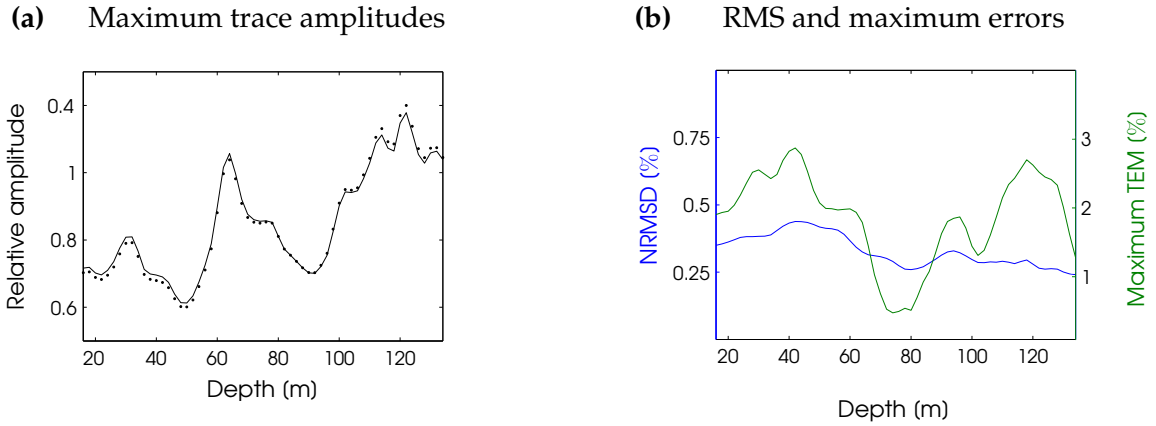

Figure 4: *Model SAT.* ***(a)*** *Maximum trace amplitudes of 2-D (dashed) and filtered 3D (solid) data.* ***(b)*** *NRMSD and maximum TEM in %.*

Model BAT - NRMSD, maximum TEM errors and maximum trace amplitudes

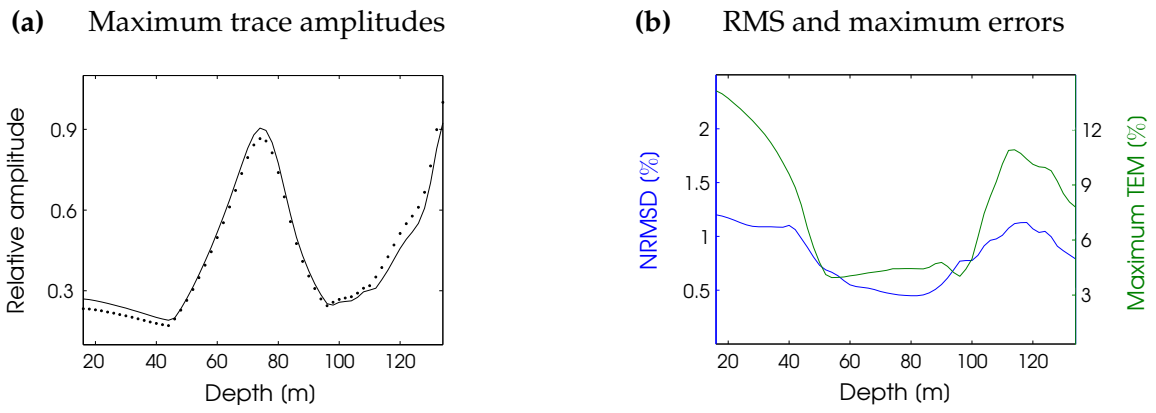

Figure 5: *Model BAT.* ***(a)*** *Maximum trace amplitudes of 2-D (dashed) and filtered 3D (solid) data.* ***(b)*** *NRMSD and maximum TEM in %.*

Model BET(e) and BET(x) - NRMSD and maximum TEM errors

(a) BET, explosive source, x comp.

(b) BET, explosive source, z comp.

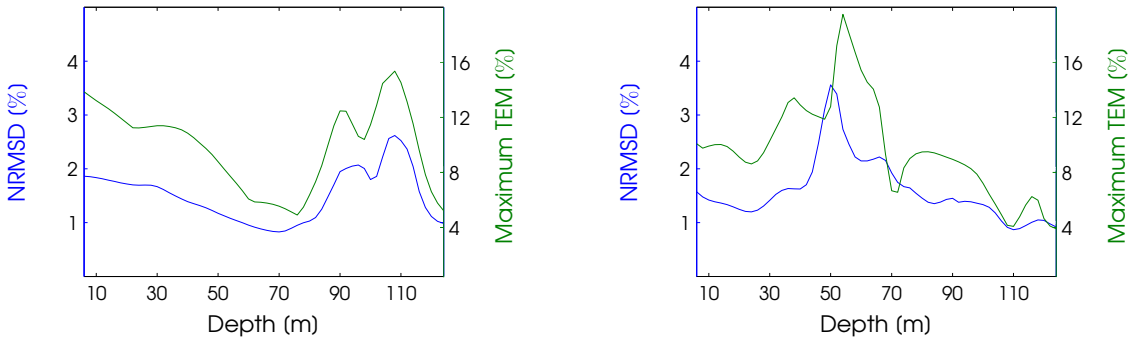

(c) BET, directed source, x comp.

(d) BET, directed source, z comp.

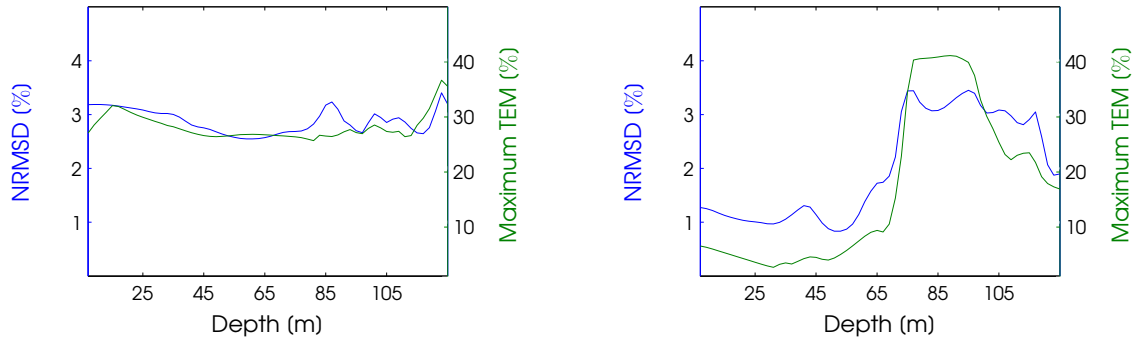

Figure 6: *Trace-by-trace NRMSD and maximum TEM errors for models BET(e) and BET(x). In* ***(a)*** *and* ***(c)****, x components are shone whereas in* ***(b)*** *and* ***(d)*** *z components are displayed. Errors are significant in all cases, but values are largest when an x-directed source is used. The low velocity zone in depths between 70 and 110 m manifests in large errors in* ***(a)*** *and* ***(d)****.*

Model SET(e) and SET(x) - NRMSD and maximum TEM errors

(a) SET, explosive source, x comp.

(b) SET, explosive source, z comp.

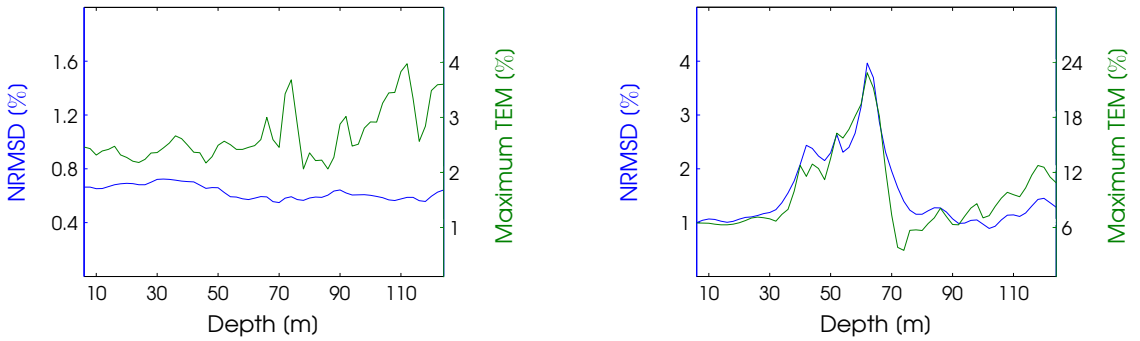

(c) SET, directed source, x comp.

(d) SET, directed source, z comp.

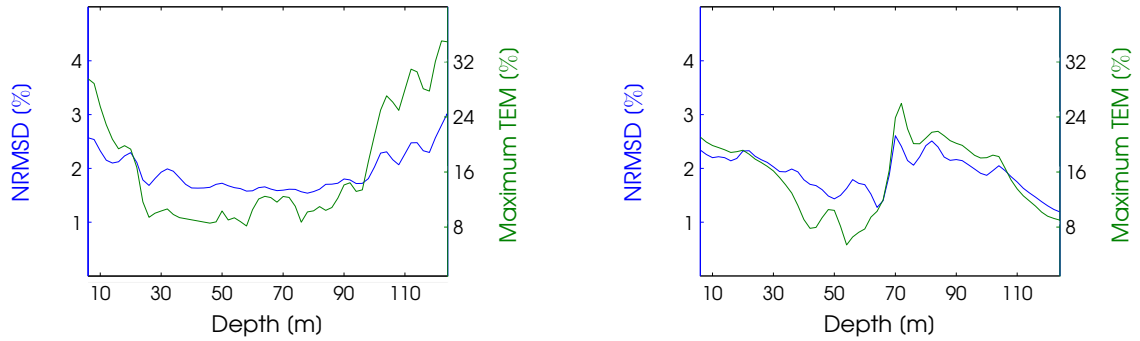

Figure 7: *Trace-by-trace NRMSD and maximum TEM errors for models SET(e) and SET(x). In* ***(a)*** *and* ***(c)****, x components are shone whereas in* ***(b)*** *and* ***(d)*** *z components are displayed. Errors are lower than for model BET, but still considerable and much larger than in the acoustic model SAT.*

Influence of dominant wavelength on RMS error; SAT and BAT

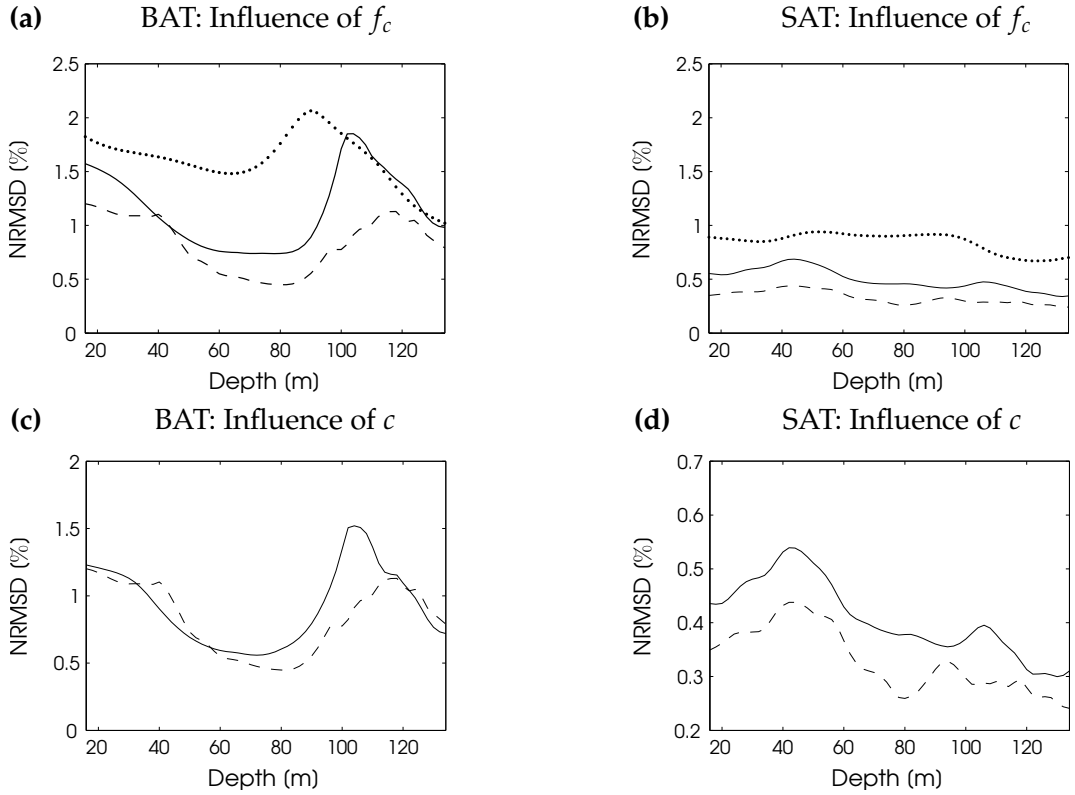

Figure 8: *Influence of dominant wavelength.* ***(a)*** *Comparison of NRMSD filter error for simulations with 100 Hz (dashed line), 50 Hz (solid line) and 25 Hz (dotted line) central frequency of the source wavelet on model BAT.* ***(b)*** *Analogue results for model SAT.* ***(c)*** *and* ***(d)*** *NRMSD values for low (dashed line) and high (solid line) velocities for model BAT and SAT, respectively.*

List of Figures

Bibliography

Abramowitz M. and Stegun I. *Handbook of Mathematical functions: with Formulas, Graphs, and Mathematical Tables*. Dover Publications, 1965.

Aki K. and Richards P. G. *Quantitative Seismology*. University Science Books, 2002.

Belina F. A., Ernst J. R., and Hollinger K. Inversion of crosshole seismic data in heterogeneous environments: Comparison of waveform an ray-based approaches. *Journal of Applied Geophysics*, 68:85–94, 2008.

Ben-Hadj-Ali H., Operto S., and Virieux J. Velocity model building by 3D frequency-domain full-waveform inversion of wide-aperture seismic data. *Geophysics*, 73:VE101–VE117, 2008.

Bleibinhaus F., Lester R. W., and Hole J. A. Applying waveform inversion to wide-angle seismic surveys. *Tectonophysics*, 472:238–248, 2009.

Bleistein N. *Mathematical methods for Wave Phenomena*. Elsevier, 1984.

Bleistein N. Two-and-One-Half Dimensional In-Plane Wave Propagation. *Geophysical Prospecting*, 34:686–703, 1986.

Bohlen T. Parallel 3-D viscoelastic finite difference seismic modelling. *Computers & Geosciences*, 28:887–899, 2002.

Bouchon M. A Review of the Discrete Wavenumber Method. *Pure and Applied Geophysics*, 160:445–465, 2003.

Brenders A. J. and Pratt R. G. Full waveform tomography for lithospheric imaging: Results from a blind test in a realistic crustal model. *Geophysical Journal International*, 168:133–151, 2006.

Brossier R., Operto S., and Virieux J. Seismic imaging of complex onshore structures by 2D elastic frequency-domain full-waveform inversion. *Geophysics*, 74: WCC105–WCC118, 2009.

Cao S. and Greenhalgh S. A. 2.5-D Acoustic Wave Modelling in the Frequency-wavenumber Domain. *Exploration Geophysics*, 28:11–15, 1997.

Cervený V. *Seismic Ray Theory*. Cambridge University Press, 2005.

Crase E., Pica A., Noble M., McDonald J., and Tarantola A. Robust elastic nonlinear waveform inversion: Application to real data. *Geophysics*, 55:527–538, 1990.

Deregowski S. M. and Brown S. M. A Theory of Acoustic Diffractors Applied to 2-D Models. *Geophysical Prospecting*, 31:293–333, 1983.

Ernst J. R. *2-D Finite Difference Time-Domain Full-Waveform Inversion of Cross-hole Georadar Data*. PhD thesis, Applied and Environmental Geophysics, ETH Zurich, 2007.

Esmersoy C. and Oristaglio M. Reverse-time wave-field extrapolation, imaging and inversion. *Geophysics*, 53:920–931, 1988.

Fichtner A. *Full Seismic Waveform Modelling and Inversion*. Springer, 2010.

Greenhalgh M., Liu X., Greenhalgh S. A., Sinclair C., and Zhou B. Removing the singularities in 2.5-D frequency-domain elastic wave modelling by introducing slight attenuation. (submitted to Geophysical Prospecting), 2009.

Hicks G. J. and Pratt R. G. Reflection waveform inversion using local descent methods: Estimating attenuation and velocity over a gas-sand deposit. *Geophysics*, 66:598–612, 2001.

Igel H., Debski W., Djikpéssé H., and Tarantola A. Gradient Inversion of Marine Seismic Reflection Data: Parameterization and Geometrical Spreading. *SEG Technical Program Expanded Abstracts*, 12:657–660, 1993.

Klotzsche A., Kruk van der J., Meles G. A., Doetsch J., Maurer H., and Linde N. Full-waveform inversion of cross-hole ground-penetrating radar data to characterize a gravel aquifer close to the Thur River, Switzerland. *Near Surface Geophysics*, 8:635–649, 2010.

Kravtsov Y. A. and Orlov Y. I. *Geometrical Optics of Inhomogeneous Media*. Springer, 1990.

Kristeková M., Kristek J., Moczo P., and Day S. M. Misfit Criteria for Quantitative Comparison of Seismograms. *Bulletin of the Seismological Society of America*, 96: 1836–1850, 2006.

Latzel S. *2.5D elastic modelling and sensitivity investigations directed towards near-*

surface seismic waveform analysis. PhD thesis, Applied and Environmental Geophysics, ETH Zurich, 2010.

Lauterborn W., Kurz T., and Wiesenfeldt M. *Coherent Optics: Fundamentals and Applications*. Springer, 1999.

Liner C. L. *Elements of 3D seismology*. Penwell Pub, 2004.

Mallick S. and Frazer L. N. Practical aspects of reflectivity modeling. *Geophysics*, 52:1355–1364, 1987.

Marelli S., Maurer H., and Manukyan E. A review of the acoustic approximation in full waveform seismic tomography. (submitted to Geophysics), 2011.

Margrave G. F. *Numerical Methods of Exploration Seismology with algorithms in MATLAB*. CREWES Consortium, 2001.

Martin G. S., Wiley R., and Marfurt K. J. Marmousi2: An elastic upgrade for marmousi. *The Leading Edge*, 25:156–166, 2006.

Maurer H., Greenhalgh S. A., and Latzel S. Frequency and spatial sampling strategies for crosshole seismic waveform spectral inversion experiments. *Geophysics*, 74:WCC79–WCC89, 2009.

Miksat J., Müller T. M., and Wenzel F. Simulating three-dimensional seismograms in 2.5-dimensional structures by combining two-dimensional finite difference modelling and ray tracing. *Geophysical Journal International*, 174:309–315, 2008.

Min D.-J., Shin C., Pratt R. G., and Yoo H. S. Weighted-averaging finite-element method for 2D elastic wave equations in the frequency-domain. *Bulletin of the Seismological Society of America*, 93(2):904–921, 2003.

Mora P. Nonlinear two-dimensional elastic inversion of multioffset seismic data. *Geophysics*, 52:1211–1228, 1987.

Morse P. M. and Feshbach H. *Methods of Theoretical Physics, Part I and II*. McGraw-Hill Science/Engineering/Math, 1953.

Mulder W. A., P. C., and Rijzen van de M. J. 2D Acoustic Full Waveform Inversion of a Land Seismic Line. *Expanded Abstract A021, 72nd EAGE Conference & Exhibition, Barcelona, Spain*, 2010.

Novais A. and Santos L. T. 2.5D finite-difference solution of the acoustic wave equation. *Geophysical Prospecting*, 53:523–531, 2005.

Phinney R. A. Theoretical Calculation of the Spectrum of First Arrivals in Layered Elastic Mediums. *Journal of Geophysical Research*, 70:5107–5123, 1965.

Pica A., Diet J. P., and Tarantola A. Nonlinear inversion of seismic reflection data in a laterally invariant medium. *Geophysics*, 55:284–292, 1990.

Pratt R. G. and Shipp R. M. Seismic waveform inversion in the frequency-domain, Part 2: Fault delineation in sediments using crosshole data. *Geophysics*, (submitted), 1998.

Reiter D. T. and Rodi W. Nonlinear waveform tomography applied to crosshole seismic data. *Geophysics*, 61:902–913, 1996.

Roberts M. A line source to point source transform for seismograms. *Lithos Science Report*, 7:49–52, 2005.

Schenk O. and Gärtner K. Solving unsymmetric sparse systems of linear equations with PARDISO. *Future Generation Computer Systems*, 20(3):475–487, 2004.

Shipp R. Two-dimensional full wavefield inversion of wide-aperture marine seismic streamer data. *Lithos Science Report*, 3:11–34, 2001.

Sinclair C. *Elastic Wave Modelling in Anisotropic Media using the Spectral-Element Methods*. PhD thesis, Deoartment of Physics, School of chemistry and Physics, University of Adelaide, 2009.

Sinclair C., Greenhalgh S. A., and Zhou B. Wavenumber Sampling Issues in 2.5D Frequency Domain Seismic Modelling. *Pure and Applied Geophysics*, 2011.

Slawinski M. A. *Seismic Waves and Rays in Elastic Media*. Elsevier, 2003.

Song Z.-M. and Williamson P. R. Frequency-domain acoustic-wave modeling and inversion of crosshole data: Part I - 2.5-D modeling method. *Geophysics*, 60: 784–795, 1995.

Takenaka H. and Tanaka H. Quasi-cylindrical 2.5D wave modeling for large-scale seismic surveys. *Geophysical Research Letters*, 30, 2003.

Tarantola A. A strategy for nonlinear elastic inversion of seismic reflection data. *Geophysics*, 51:1893–1903, 1986.

Vidale J., Helmberger D. V., and Clayton R. W. Finite-difference Seismograms for SH Waves. *Bulletin of the Seismological Society of America*, 75:1765–1782, 1985.

Vigh D. and Starr E. W. 3D prestack plane-wave, full-waveform inversion. *Geophysics*, 73:VE135–VE144, 2008.

Virieux J. and Operto S. An overview of full-waveform inversion in exploration geophysics. *Geophysics*, 74:WCC1–WC26, 2009.

Wapenaar C. P. A., Verschuur D. J., and Herrmann P. Amplitude preprocessing of single and multicomponent seismic data. *Geophysics*, 57:1178–1188, 1992.

Williamson P. R. and Pratt R. G. A critical review of acoustic wave modeling procedures in 2.5 dimensions. *Geophysics*, 60:591–595, 1995.

Yedlin M., Vorst van D., and Virieux J. Uniform Asymptotic Conversion of Helmholtz Data from 3D to 2D. *Journal of Applied Geophysics*, submitted, 2011.

Yilmaz O. *Seismic Data Analysis: Processing, Inversion and Interpretation of Seismic Data*. Society of Exploration Geophysicists, 1987.

Zhou B. and Greenhalgh S. Explicit expressions and numerical calculations for the Fréchet and second derivatives in 2.5D Helmholtz equation inversion. *Geophysical Prospecting*, 47:443–468, 1999.

Zhou B. and Greenhalgh S. A. A damping method for the computation of the 2.5-D Green's function for arbitrary acoustic media. *Geophysical Journal International*, 133:111–120, 1998a.

Zhou B. and Greenhalgh S. A. Crosshole acoustic velocity imaging with full-waveform spectral data: 2.5-D numerical simulations. *Exploration Geophysics*, 29:680–684, 1998b.

Zhou B. and Greenhalgh S. A. An Adaptive Wavenumber Sampling Strategy for 2.5D Seismic-Wave Modeling in the Frequency Domain. *Pure and Applied Geophysics*, 163:1399–1416, 2006.